Title

Applications of van der Waals Thin Films

Author

Xu, Dong

Publication Date

2023

Peer reviewed|Thesis/dissertation

UNIVERSITY OF CALIFORNIA

Los Angeles

Applications of van der Waals Thin Films

A dissertation submitted in partial satisfaction

of the requirements for the degree

Doctor of Philosophy in Material Science and Engineering

by

Dong Xu

2023

ABSTRACT OF THE DISSERTATION

Applications of van der Waals Thin Films

by

Dong Xu
Doctor of Philosophy in Material Science and Engineering
University of California, Los Angeles, 2023
Professor Yu Huang, Co-Chair
Professor Xiangfeng Duan, Co-Chair

The 2D materials have drawn great interests since they have been exploited. Although they have excellent properties, the mass production has been a great challenge. To overcome this, a solution proceeded approach was introduced in 2018. The MoS_2 ink is prepared by intercalating ammonia salt into the raw material and exfoliated the bulk materials into small thin flakes and get a suspension solution. This MoS_2 ink can be easily spin−coated on to hydrophilic surface and form a uniform large−scaled semiconducting thin film with high performance. The thin films are made of flakes overlapped with each other by van der Waals force, so we call them van der Waals thin film (VDWTF). And my projects are main about the applications of the VDWTF. The first application is using the thin film as conventional transistors. And we manage to build an integrated pressure sensor array, by combining solution-processed two-dimensional (2D) MoS_2 van der Waals (vdW) thin film transistor (TFT) active matrix and conductive micropyramidal pressure-sensitive rubber (PSR) electrodes made of polydimethylsiloxane/carbon nanotube composites, to achieve spatially revolved pressure mapping with excellent contrast and low power consumption. We

demonstrate a 10 $\times$ 10 active matrix by using the 2D MoS_2 vdW-TFTs with high on-off ratio $> 10^6$, minimal hysteresis, and excellent device-to-device uniformity. The combination of the vdW-TFT active matrix with the highly uniform micropyramidal PSR electrodes creates an integrated pressure sensing array for spatially resolved pressure mapping. This study demonstrates that the solution-processed 2D vdW-TFTs offer a solution for active-matrix control of pressure sensor arrays, and could be extended for other active matrix arrays of electronic. Because the thin film MoS_2 has a high light transmission rate, our thin film can applied for optoelectronic devices as transparent transistor. Here we merge our thin film transparent phototransistors (TPTs) with liquid crystal (LC) modulators to create an optoelectronic neuron array that allows self-amplitude modulation of spatially incoherent light, achieving a large nonlinear contrast over a broad spectrum at orders-of-magnitude lower intensity than most optical nonlinear materials. For a proof-of-concept demonstration, we fabricated 10,000 optoelectronic neurons, each serving as a nonlinear filter, and experimentally demonstrated an intelligent imaging system that uses their nonlinear response to significantly reduce input glares while retaining the weaker-intensity objects within the field of view of a cellphone camera. This nonlinear glare-reduction capability is important for various imaging applications, including autonomous driving, machine vision, and security cameras. Beyond imaging and sensing, this optoelectronic neuron array, with its nonlinear self-amplitude modulation for processing incoherent broadband light, might also find applications in optical computing, where nonlinear activation functions that can work under ambient light conditions are highly sought. In the next chapter, we demonstrate the application of the VDWTF as flexible electronics. The films feature a sliding and rotation degree of freedom among the staggered nanosheets to ensure mechanical stretchability and malleability, as well as a percolating network of nanochannels to endow permeability and breathability. With an excellent mechanical match to soft biological tissues, the freestanding films can naturally adapt to local surface topographies and seamlessly merge with living organisms with highly conformal interfaces, rendering living organisms with electronic func-

tions, including leaf-gate and skin-gate transistors. On-skin transistors allow high-fidelity monitoring and local amplification of skin potentials and electrophysiological signals.

The dissertation of Dong Xu is approved.

Jaime Marian

Ximin He

Xiangfeng Duan, Committee Co-Chair

Yu Huang, Committee Co-Chair

University of California, Los Angeles

2023

To my parents . . .

who—gave me all they have

supported me for whatever I pursue

TABLE OF CONTENTS

LIST OF FIGURES

LIST OF TABLES

ACKNOWLEDGMENTS

Almost 6 years study in Material Science and Engineering Department at University of California, Los Angeles changes my life totally from a naive young man. And I would like to express my appreciation to those who made these years memorable.

First I would like to thank my advisor, Professor Xiangfeng Duan, for his guidance in my research and in my life. The start of my PhD journey was not smooth as others might thought. Prof. Duan corrected my thoughts about the past on time and led me to move forward. In the following researches he taught me how to wisely set the targets and use the most efficient way to achieve them. This really changed my mind. Previously I was only trying to do something but did not really understand what I am working for. These years experience changed me totally.

Also I would like to thank Professor Yu Huang, for her support over these years. Professo Huang's attitude toward work and relationship enlightened me. And her support over these years really help me pass the difficult time especially during pandemic time.

I would like to thank my committees, Professor Ximin He and Professor Jaime Marian, for reading my thesis and giving me suggestion in oral qualification exam and in my defense.

I really enjoy the time in an outstanding group. And there are too many I want to show my appreciation. Dr. Chao Ma's hard working and persistence in researches enlightened me at the time I joined this group and I really appreciate the time working with him. Dr Zhuocheng Yan's attitude toward science should be remembered not just by me but also by those who want to achieve great goals. And I miss the time when we finished a great job together. Dr Dehui Zhang makes a great partner and also a good friend. I am confident

that he can accomplish more in the future. I also would thank to Dr. Jin Huang, Dr. Peiqi Wang, Dr. Zhaoyang Lin, Dr. Yuan Liu, Dr. Jian Guo Dr. Zhong Wan, Dr. Qi Qian, Dr. Laiyuan Wang, Dr. Yun-chiao Huang, Dr. Jingyuan Zhou and Dr. Huaying Ren for their help and advice during my years of studies.

And I really enjoy the time of life in our group. Thank to Dr. Haotian Liu, Dr. Guangyan Zhong, Dr. Jin Cai, Dr. Zeyan Liu, Dr. Bosi Peng, Dr. Peiqi Wang, Dr. Chengzhang Wan, Dr. Jian Guo, Dr. Chao Ma, Dr. Yun-chiao Huang, Dr. Jin Huang, Ao Zhang, Yang Liu, Boxuan Zhou, Dr. Dehui Zhang, Dr. Zhuocheng Yan, Dr Wang Xue, Dr. Frank Song, Dr. Dan Zhu, Dr. Jingyuan Zhou, Dr. Huaying Ren, Jingxuan Zhou, Yansong Ling, Zipeng Zhao, and so many friends who have walked through these years with me. It is a time I will never forget.

Last but not least, I really appreciate my parents. I can not make it through all of these without their support and understanding.

VITA

1995	Born, Qingdao, Shandong, China
2015–2017	Undergrad Researcher, Material Research Laboratory, University of Illinois, Urbana-Champaign.
2017	B.S.$\sim$ (Engineering Physics) and B.S.$\sim$ (Chemistry), University of Illinois, Urbana-Champaign.
2018–2022	Teaching Assistant, UCLA.
2017–present	Graduate Research Assistant, Material Science and Engineering Department, UCLA.

CHAPTER 1

Introduction

1.1 Introduction to two dimensional materials

The two dimensional materials have drawn great interests since they were introduced because of their unique electrical and mechanical properties [1–19]. The definition of 2D materials is not limited to the literal meaning of two dimensional. And actually there are many different classes can be considered as 2D materials because the main characteristics of those materials, electrical and mechanical, are in one plane, which means that we can consider those materials as a piece of paper when consider their properties, and the features outside the plane are negligible. Three typical diagrams of 2D materials are shown in Fig1.1. The left one is the representative of the 2D family, graphene. Graphene has all its atoms aligned in one plane with strong interaction, while the connection between layers is due to van der Waals and is very weak. Therefore the electrons are mainly transported in the atomic plane as the barrier between planes are huge. Thus the graphene is called 2D material. In the middle of Fig 1.1 is a diagram of transition metal dichalcogenides. As shown in the picture, this class of materials has three stacks of atoms in on plane connected by strong inter-atomic bonds. The interaction between planes are still by van der Waals, which also means that the main characteristics of this material are also in one plane. This class of materials takes a lot of attentions because with different arrangements of atoms in one plane, the properties of the whole material could be different. The right one represents the intercalated materials. Bulk materials can be intercalated with organic molecules to break the inter plane connections, so the out of plane properties can be negligible in this case. And this method can generate

some interesting properties that are not found in the bulky precursor.

The properties of 2D materials make them special and can be used to replace bulk materials in the future. As mentioned, the electrical and mechanical properties of 2D materials are within a single plane, which means they do not need a thick bulky structure to maintain the basic functions. Thus we can build a single high performance electric device with just one or a few layers of 2D materials which is usually several nanometer. This is hard to be achieved with conventional materials. The structure of bulk materials or 3D materials requires the connection between atoms in 3 dimensions. If we make the device in a few nanometer thick, the dangling bonds on the surface will start to affect the performance of the whole device. So the bulk materials need to maintain a certain thickness to have their basic functions. Also thinner transistor channel means they can be driven with lower gate voltage, which will decrease the power consumption.

Another advantage of 2D materials is that they can be easily doped [20–22]. Because the thickness of the total device is within nanometer, the molecule or atoms just need to penetrate one layer to dope the material. Therefore it gives us more flexibility in manipulating the properties of the material. On the contrary, doping bulk materials usually requires harsh environments and conditions as the molecules and particles need to penetrate many layers of atoms.

1.2 Preparation of two dimensional materials

There are two methods in mass production of 2D materials. The first one is chemical vapor deposition (CVD). CVD process uses gas phase to synthesize materials. The advantage of this process is that it could generate high quality single layered materials. But the cost is

comparatively high as the reaction condition is harsh. In order to avoid the defects from the alien particles, the chamber needs to be pumped into a high vacuum, also the reaction temperature is high so the precursors can fully react to form the target [23–26]. As shown in fig 1.2. there need to be nucleation cites for the target to locate on the substrate, and the status of the nucleation cites will determine the final states of the materials grown on. As it is hard to make every cites aligned perfectly, so the final products are usually poly crystalline.

The other method is intercalation. The basic idea of intercalation is to exfoliate the thick bulk materials that contains the flakes of 2D target materials into small pieces and thus get the thin layer 2D materials. Many of the 2D materials have their natural raw materials, so the cost of intercalation is mcuh lower in this case. There are 3 different types of intercalation. The first one is electrical intercalation, which use electric field to drive the intercalant in the solution to diffuse into the target host. And with the following sonicate process, the bulk materials can be exfoliated into thinner flakes that can be used. The second method is similar to thermal doping, which use the thermal gradient to diffuse intercalant into the host. The following processes are similar for all intercalation process as the host needs dynamic energy to break it into small pieces and later screen out the unwanted parts. And the last one is to do the diffusion process in liquid phase.The major weakness of the conventional intercalation method is the low product quality especially in for semiconducting materials [27–29].

To overcome the challenge of mass production with high quality semiconducting 2D materials, a solution proceeded approach was introduced by Dr. Lin in 2018 [30]. The detailed schematics are shown in fig. 1.4 [30]. The solution is made by intercalating tetrahexylammonium (THA) molecules into the MoS_2 raw materials and then diffuse polyvinylpyrrolidone (PVP) into the system to further exfoliate the material. After this the precursor is repetitively sonicated and centrifuged to screen out the redundant PVP and undesirable sized flakes in the solution. Finally the intercalated materials are dispersed in isopropyl alcohol

and can be easily spin coated on any hydrophilic substrate. As shown in fig. 1.4b, the final product is a thin film consist of small flakes of 2D MoS_2 tiled up by van der Waals, so we call this type of materials VDWTF.

There are many advantages of our VDWTF. At first the ink can be easily spin coated to generate a uniform large area thin film which can be further fabricated into any dimension circuits elements (as shown in fig. 1.5 [30]). Also, the preparation of the ink can be done within 5 hrs with a low cost smaller than 1.4 dollars per batch, and each batch can produce three to four 4 inch wafers. The cost can be further reduced with industrialized procedures. Another advantage is that this ink can be reserved for weeks before use and the final product of semiconducting thin films also have a long lifetime of years. Although the cost is low, the quality of the thin film is high, the on/off ratio is about $10^5 - 10^6$, and more details are discussed in chapter 2.

1.3 Properties of van der Waals thin films

There are some morphology differences between the CVD growth thin film (CVDTF) and the VDWTF As shown in fig.1.6, the CVD growth materials have larger size mono layers and finer grains and the intercalated materials have smaller flakes overlapped with each other to form a film connected by van der Waals. The overlapped parts in the thin film allows the electrons to transport with a small barrier, which ensure great electronic properties. And this makes it a great semiconductor for large scale circuits. Also the weak van der Waals allow the flakes to slide with each other, which creates a dynamic stability for the thin film to compensate the strain generated over bending and stretching. And this means the VDWTF is a great candidate for flexible electronics.

1.4 overview of dissertation

In this dissertation, I would discuss three different types of applications of van der waals thin film (VDWTF). First in chapter 2, I will introduce the VDWTF as a traditional transistor channel which can be used in large scale circuits. To fulfill the requirements of large scale circuits, the VDWTF should have the following properties: 1. The thin film should have a high on/off ratio within a low gate voltage regime, so it can be used as a switch with a low power consumption; 2. the transistor should have low hysteresis to ensure the consistency of performance of single device; 3. it can be fabricated over wafer scale with a high pixel to pixel consistency, so the performance of all transistors over the device are the same. And in this chapter, we developed a series of fabrication process that can build a large scale active matrix with a yield of 98% and it can be further used in pressure mapping with the pressure sensing rubber introduced in the next chapter.

In chapter 3, the VDWTF was used as a optical sensor. As mentioned in chapter 2, the VDWTF can be used in large scale circuits as transistors with a great performance. In this chapter, we further studied the application of the VDWTF as a photo transistor and can be developed into glare reduction system. The 2D MoS_2 has a high light transmission rate so the thin film transistor is transparent to light. And we can develop the thin film into a photo sensor that can capture the feature of light pass through it but do not affect the light too much. Later we combine this transparent phototransistor with liquid crystal to modify the transparency of the liquid crystal by the light goes through the device. This setup can be further developed into a glare reduction system and a diffractive neural network with high non-linearity.

In chapter 4, I will demonstrate the application of free standing VDWTFs as a candidates for flexible electronics. Traditional flexible electronics are usually made with substrates as

the electrodes and other elements needs supporting layers to hold the integrity of the whole device to ensure the function of the device. However, the total thickness of the device will increase together with the stiffness, and this will make the whole device incompatible with the fine−featured surface of the bio-target. Therefore it will generate more noise. To solve this problem, we introduced our VDWTF as a free-standing sensor. Because the thin film is made with tiled up flakes of 2D materials connected by van der Waals, each flake can slide with each other to compensate the stress generated during bending and maintain the integrity of the film. Therefore the thin film is not just highly flexible but more strechable and can fit the arbitrary featured surface of target. And this makes it a great candidate for the flexible electronics.

In chapter 5, I will briefly discuss the process from free standing thin films to the high performance flexible electronics devices. As mentioned in the previous chapter, the VDWTF is a great candidate for flexible electronics with ultra conformability. But the whole electronic device requires more than just a thin film sensor, it needs a whole package of different elements from the sensing part to the signal transmission part. And the connection parts are usually very fragile as they need to be compatible with both sides. For our thin film, it is very flexible, which makes it easy to fit the target and generate good signal. But it is also very fragile and can be easily broken by other comparatively rigid materials, even polymers like polyimide. So it is essential to find a packaging process to make the whole device functional. And we are also doing cuffless blood pressure measurement with the thin film sensor.

Chpater 6 is a supplimentary chapter for the pressure sensing rubber (PSR) used in chapter 2. In this chapter, I will discuss about the PSR and its application in electronic skin. The PSR is made with Polydimethylsiloxane (PDMS) and conductive carbon nanotube (CNT). The CNT can form a conductive mesh in the PDMS and maintain the net structure during

deformation, so its connectivity can be maintained. Also the surface of the PSR is made with micro-pyramid by casting the precursor into a Silicon made mould. The micro-pyramid deforms greatly under small pressure, and this will lead to a sharp increase in the contact area with the electrode and therefore the current go through the circuit will greatly increase. In this chapter, we also studied the spacial arrangement of the micro-pyramid to give a guideline for the design of similar pressure sensor.

1.5 Figures and Legends

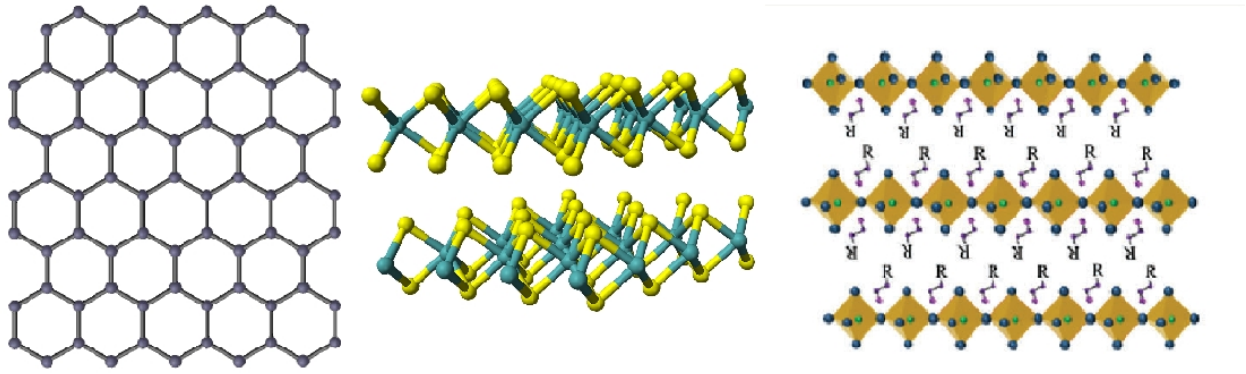

Figure 1.1: Three different types of 2D materials: (Left) graphene; (Middle) transition metal dichalcogenides; (Right) intercalated materials.

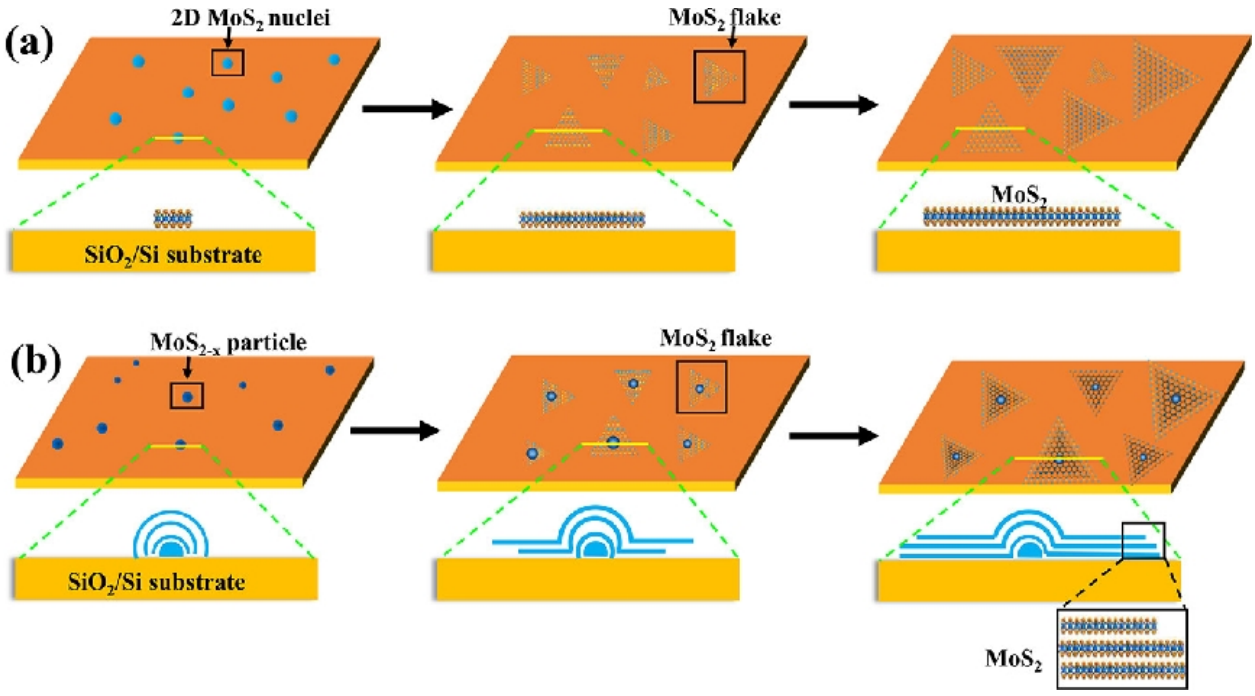

Figure 1.2: Two processes of chemical vapor deposition of MoS_2: (a) growth with 2D MoS_2 nuclei; (b) with MoS_{2-x} particle

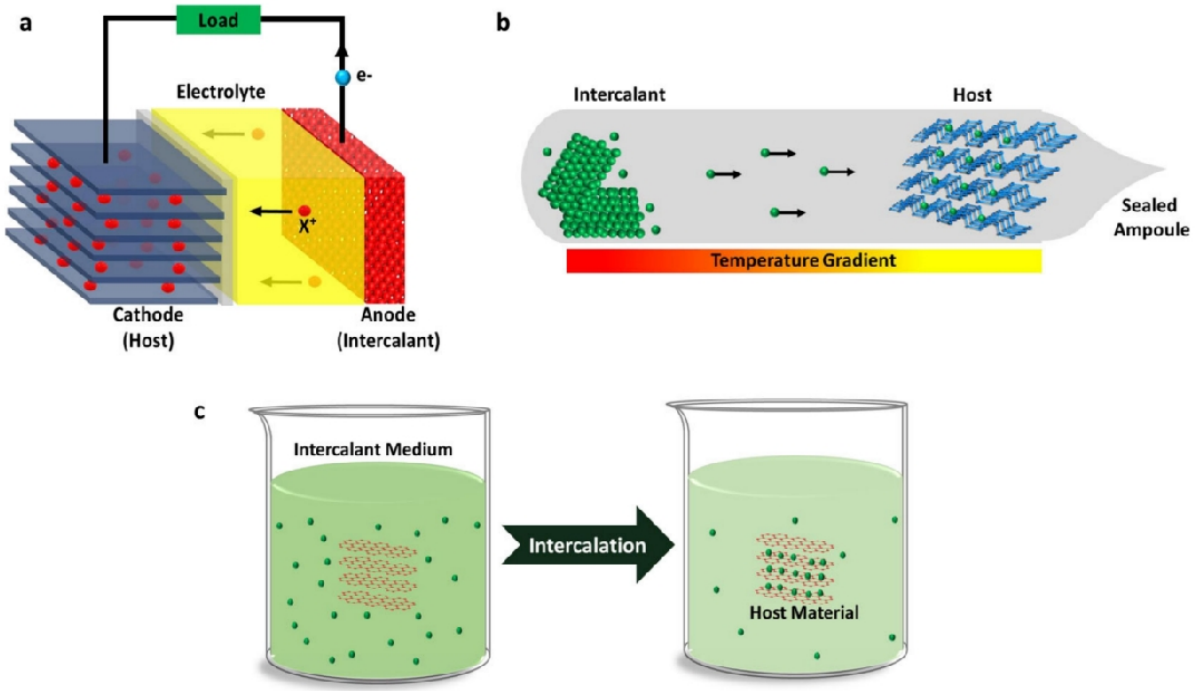

Figure 1.3: Three different methods of intercalation: (a) electrical intercalation; (b) thermal intercalation; (c) liquid phase intercalation

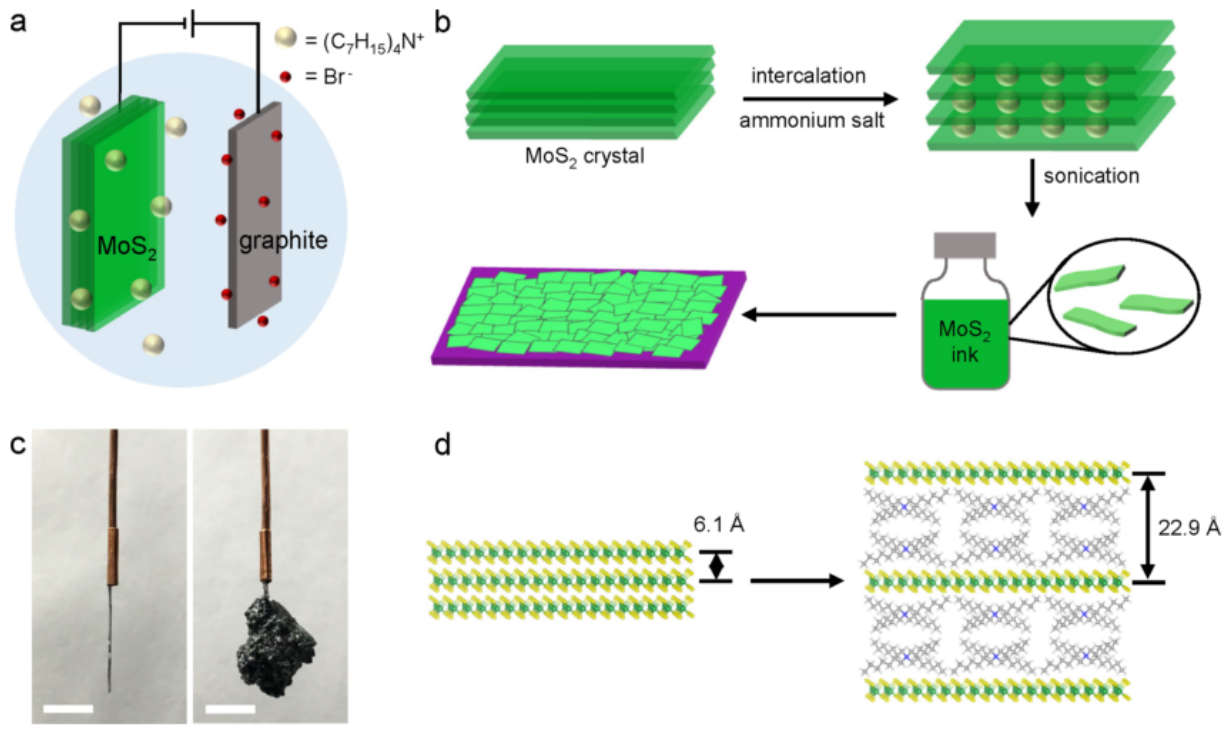

Figure 1.4: Molecular intercalation and exfoliation of MoS_2 nanosheets.

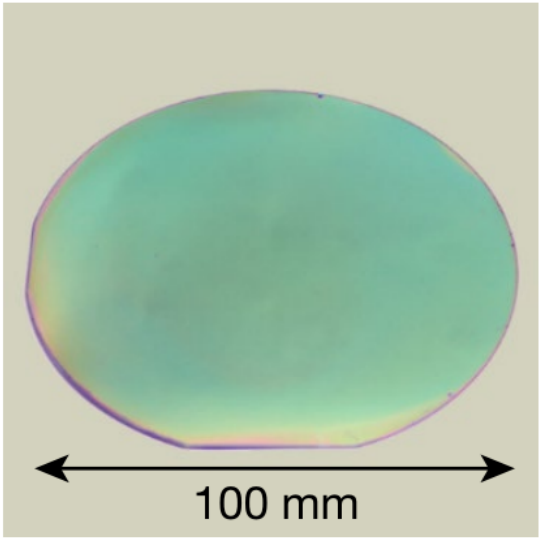

Figure 1.5: Photograph of the MoS_2 thin film deposited on a standard $100 - mm - diameter$ SiO_2/Si wafer.

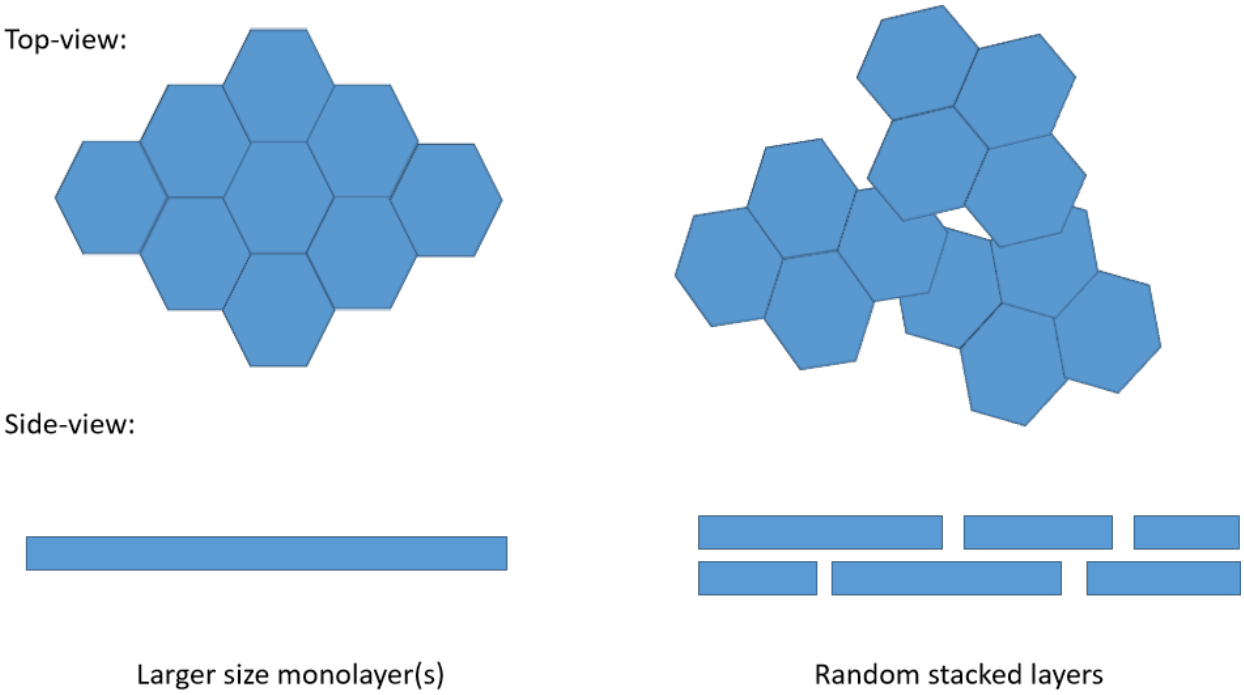

Figure 1.6: Mophorlogy of CVD thin film (left) and VDWTF (right).

References

[1] Gianluca Fiori, Francesco Bonaccorso, Giuseppe Iannaccone, Tomás Palacios, Daniel Neumaier, Alan Seabaugh, Sanjay K. Banerjee, and Luigi Colombo. Electronics based on two-dimensional materials. *Nature Nanotechnology*, 9(10):768–779, Oct 2014.

[2] Joohoon Kang, Vinod K. Sangwan, Hong-Sub Lee, Xiaolong Liu, and Mark C. Hersam. Solution-processed layered gallium telluride thin-film photodetectors. *ACS Photonics*, 5(10):3996–4002, 2018.

[3] Jung-Woo Ted Seo, Jian Zhu, Vinod K. Sangwan, Ethan B. Secor, Shay G. Wallace, and Mark C. Hersam. Fully inkjet-printed, mechanically flexible mos2 nanosheet photodetectors. *ACS Applied Materials & Interfaces*, 11(6):5675–5681, 2019. PMID: 30693759.

[4] Zhaoyang Lin, Yuan Liu, Udayabagya Halim, Mengning Ding, Yuanyue Liu, Yiliu Wang, Chuancheng Jia, Peng Chen, Xidong Duan, Chen Wang, Frank Song, Mufan Li, Chengzhang Wan, Yu Huang, and Xiangfeng Duan. Solution-processable 2d semiconductors for high-performance large-area electronics. *Nature*, 562(7726):254–258, Oct 2018.

[5] Zhaoyang Lin, Yu Huang, and Xiangfeng Duan. Van der waals thin-film electronics. *Nature Electronics*, 2(9):378–388, Sep 2019.

[6] Manish Chhowalla, Debdeep Jena, and Hua Zhang. Two-dimensional semiconductors for transistors. *Nature Reviews Materials*, 1(11):16052, Aug 2016.

[7] Deji Akinwande, Cedric Huyghebaert, Ching-Hua Wang, Martha I. Serna, Stijn Goossens, Lain-Jong Li, H.-S. Philip Wong, and Frank H. L. Koppens. Graphene and two-dimensional materials for silicon technology. *Nature*, 573(7775):507–518, Sep 2019.

[8] Qijie Liang, Qian Zhang, Jian Gou, Tingting Song, Arramel, Hao Chen, Ming Yang, Sharon Xiaodai Lim, Qixing Wang, Rui Zhu, Nikolai Yakovlev, Swee Ching Tan, Wen-

jing Zhang, Kostya S. Novoselov, and Andrew T. S. Wee. Performance improvement by ozone treatment of 2d pdse2. *ACS Nano*, 14(5):5668–5677, 2020. PMID: 32364379.

[9] Ruitao Lv, Joshua A. Robinson, Raymond E. Schaak, Du Sun, Yifan Sun, Thomas E. Mallouk, and Mauricio Terrones. Transition metal dichalcogenides and beyond: Synthesis, properties, and applications of single- and few-layer nanosheets. *Accounts of Chemical Research*, 48(1):56–64, 2015. PMID: 25490673.

[10] Qing Hua Wang, Kourosh Kalantar-Zadeh, Andras Kis, Jonathan N. Coleman, and Michael S. Strano. Electronics and optoelectronics of two-dimensional transition metal dichalcogenides. *Nature Nanotechnology*, 7(11):699–712, Nov 2012.

[11] F. Scott Stinner, Yuming Lai, Daniel B. Straus, Benjamin T. Diroll, David K. Kim, Christopher B. Murray, and Cherie R. Kagan. Flexible, high-speed cdse nanocrystal integrated circuits. *Nano Letters*, 15(10):7155–7160, 2015. PMID: 26407206.

[12] Luqi Tu, Rongrong Cao, Xudong Wang, Yan Chen, Shuaiqin Wu, Fang Wang, Zhen Wang, Hong Shen, Tie Lin, Peng Zhou, Xiangjian Meng, Weida Hu, Qi Liu, Jianlu Wang, Ming Liu, and Junhao Chu. Ultrasensitive negative capacitance phototransistors. *Nature Communications*, 11(1):101, Jan 2020.

[13] Yan Wang, Jong Chan Kim, Ryan J. Wu, Jenny Martinez, Xiuju Song, Jieun Yang, Fang Zhao, Andre Mkhoyan, Hu Young Jeong, and Manish Chhowalla. Van der waals contacts between three-dimensional metals and two-dimensional semiconductors. *Nature*, 568(7750):70–74, Apr 2019.

[14] Hu Xu, Haima Zhang, Zhongxun Guo, Yuwei Shan, Shiwei Wu, Jianlu Wang, Weida Hu, Hanqi Liu, Zhengzong Sun, Chen Luo, Xing Wu, Zihan Xu, David Wei Zhang, Wenzhong Bao, and Peng Zhou. High-performance wafer-scale mos2 transistors toward practical application. *Small*, 14(48):1803465, 2018.

[15] Heejun Yang, Sung Wng Kim, Manish Chhowalla, and Young Hee Lee. Structural and quantum-state phase transitions in van der waals layered materials. *Nature Physics*, 13(10):931–937, Oct 2017.

[16] Felix Carrascoso, Hao Li, Riccardo Frisenda, and Andres Castellanos-Gomez. Strain engineering in single-, bi- and tri-layer mos2, mose2, ws2 and wse2. *Nano Research*, 14(6):1698–1703, Jun 2021.

[17] Zhiwei Li, Yawei Lv, Liwang Ren, Jia Li, Lingan Kong, Yujia Zeng, Quanyang Tao, Ruixia Wu, Huifang Ma, Bei Zhao, Di Wang, Weiqi Dang, Keqiu Chen, Lei Liao, Xidong Duan, Xiangfeng Duan, and Yuan Liu. Efficient strain modulation of 2d materials via polymer encapsulation. *Nature Communications*, 11(1):1151, Mar 2020.

[18] Hao Liu, Lin Chen, Hao Zhu, Qing-Qing Sun, Shi-Jin Ding, Peng Zhou, and David Wei Zhang. Atomic layer deposited 2d mos2 atomic crystals: from material to circuit. *Nano Research*, 13(6):1644–1650, Jun 2020.

[19] Bei Zhao, Weiqi Dang, Xiangdong Yang, Jia Li, Haihong Bao, Kai Wang, Jun Luo, Zhengwei Zhang, Bo Li, Haipeng Xie, Yuan Liu, and Xidong Duan. van der waals epitaxial growth of ultrathin metallic nise nanosheets on wse2 as high performance contacts for wse2 transistors. *Nano Research*, 12(7):1683–1689, Jul 2019.

[20] Min Sup Choi, Deshun Qu, Daeyeong Lee, Xiaochi Liu, Kenji Watanabe, Takashi Taniguchi, and Won Jong Yoo. Lateral mos2 p–n junction formed by chemical doping for use in high-performance optoelectronics. *ACS nano*, 8(9):9332–9340, 2014.

[21] Lingming Yang, Kausik Majumdar, Han Liu, Yuchen Du, Heng Wu, Michael Hatzistergos, PY Hung, Robert Tieckelmann, Wilman Tsai, Chris Hobbs, et al. Chloride molecular doping technique on 2d materials: Ws2 and mos2. *Nano letters*, 14(11):6275–6280, 2014.

[22] Hao Wang, Liying Ouyang, Guifu Zou, Cheng Sun, Jun Hu, Xu Xiao, and Lijun Gao. Optimizing mos2 edges by alloying isovalent w for robust hydrogen evolution activity. *Acs Catalysis*, 8(10):9529–9536, 2018.

[23] HF Liu, Swee Liang Wong, and DZ Chi. Cvd growth of mos2-based two-dimensional materials. *Chemical Vapor Deposition*, 21(10-11-12):241–259, 2015.

[24] Shanshan Wang, Xiaochen Wang, and Jamie H Warner. All chemical vapor deposition growth of mos2: h-bn vertical van der waals heterostructures. *ACS nano*, 9(5):5246–5254, 2015.

[25] Xiangping Chen, Lili Zhang, and Shanshan Chen. Large area cvd growth of graphene. *Synthetic Metals*, 210:95–108, 2015.

[26] Zhaolong Chen, Yue Qi, Xudong Chen, Yanfeng Zhang, and Zhongfan Liu. Direct cvd growth of graphene on traditional glass: methods and mechanisms. *Advanced Materials*, 31(9):1803639, 2019.

[27] Zhiyuan Zeng, Zongyou Yin, Xiao Huang, Hai Li, Qiyuan He, Gang Lu, Freddy Boey, and Hua Zhang. Single-layer semiconducting nanosheets: high-yield preparation and device fabrication. *Angewandte Chemie*, 123(47):11289–11293, 2011.

[28] Rajesh Kappera, Damien Voiry, Sibel Ebru Yalcin, Brittany Branch, Gautam Gupta, Aditya D Mohite, and Manish Chhowalla. Phase-engineered low-resistance contacts for ultrathin mos2 transistors. *Nature materials*, 13(12):1128–1134, 2014.

[29] Goki Eda, Hisato Yamaguchi, Damien Voiry, Takeshi Fujita, Mingwei Chen, and Manish Chhowalla. Photoluminescence from chemically exfoliated mos2. *Nano letters*, 11(12):5111–5116, 2011.

[30] Zhaoyang Lin, Yuan Liu, Udayabagya Halim, Mengning Ding, Yuanyue Liu, Yiliu Wang, Chuancheng Jia, Peng Chen, Xidong Duan, Chen Wang, et al. Solution-processable 2d

semiconductors for high-performance large-area electronics. *Nature*, 562(7726):254–258, 2018.

CHAPTER 2

Two-Dimensional van der Waals Thin Film Transistors as Active Matrix for Spatially Resolved Pressure Sensing

2.1 Introduction

Pressure sensors that can interact with the external environment and discriminate the shape and texture of the targeting objects are of great importance for smart robots, prostheses, human-machine interfaces, and artificial intelligence (AI) [1–14]. For such applications, large-area pressure sensing arrays with high spatial resolution, sufficient contrast, and minimal power consumption are highly desirable [3–5]. In terms of the device design, the pressure sensing array can be divided into passive [6, 7, 15] and active-matrix [4, 5, 16–19]. In general, the active matrix, selectively addressed and controlled by the thin film transistors (TFTs), is superior to the typical passive matrix with minimal crosstalk (i.e., better contrast in high spatial resolution) and reduced power consumption. For flexible pressure sensors, organic TFTs are attractive building blocks for the active matrix for their low-temperature processability. However, the low performance of the organic TFTs such as low mobility (typically, $< 1\ \mathrm{cm}^2 \cdot \mathrm{V}^{-1} \cdot \mathrm{s}^{-1}$) often requires high operating voltage (from tens to hundreds of volts) [4, 16, 17, 20]. In addition, the intrinsic instability and vulnerability of the organic TFTs under ambient conditions could degrade the performance in a relatively short period of time [21–24]. To this end, one-dimensional (1D) inorganic semiconductors such as carbon nanotubes (CNTs) [5, 25–27] and nanowires [28–30] have been explored for TFTs

with respectable carrier mobility and excellent environmental stability. However, the typical network distribution of the 1D inorganic semiconductors on substrates may limit the device-to-device uniformity in the active matrix. In addition, the large off current CNT based TFTs usually leads to a relatively low on-off ratio and considerable power loss, which may hinder their practical applications [5, 25–28]. Alternatively, two-dimensional (2D) semiconductors have drawn of considerable recent attention for their excellent electronic properties and mechanical flexibility [31–49]. In particular, the solution assembly of 2D semiconductor (e.g., MoS_2) nanosheets creates a unique van der Waals thin films, in which the 2D nanosheets form a continuous tiled thin film with full surface coverage and the dangling-bond free interface to ensure minimum interfacial trapping states and high electronic performance [40, 41]. Such vdW-TFTs could thus promise an excellent candidate for high-performance active matrix arrays.

Apart from the active matrix, the tunability, sensitivity, and dynamic pressure range of the pressure sensitive rubber (PSR) electrodes in the integrated pressure sensors could also greatly affect the ultimate performance. The performance could be further tailored by creating microstructures in the pressure-sensitive layer. Such PSR electrode have been reported in individual or passive matrix of pressure sensors [6, 50–53], but seldomly applied in the active-matrix arrays [5, 25–28]. Here we report an integrated pressure sensor array, which combines a solution-processed 2D MoS_2 vdW-TFT active matrix with conductive micro-pyramidal PSR electrodes made of PDMS/CNT composites, to obtain a spatially resolved pressure sensing with excellent contrast and minimal power consumption. By exploiting 2D MoS_2 vdW-TFTs with high on-off ratio $> 10^6$, minimal hysteresis and excellent device-to-device uniformity, we construct high-performance active matrix with 10×10 pixels to enable pressure sensing array for spatially resolved pressure mapping.

2.2 Experimental

2.2.1 Device fabrication

The integrated pressure sensor array is constructed by a combination of the solution-processed 2D MoS_2 vdW-TFT active matrix and the conductive micro-pyramidal PSR electrodes made of PDMS/CNT composites (Figure 2.1(a)). The fabrication process of the 2D MoS_2 vdW-TFT active matrix is shown in Figure 2.1(b). The local back gates of Cr/Au (10 nm/20 nm) are defined by standard photolithography and electron-beam evaporation with about 50-nm-thick Al_2O_3 as a dielectric by atomic layer deposition (ALD). The 2D semiconducting MoS_2-nanosheet ink is subsequently spin-coated on the dielectric and patterned after thermal annealing treatments with defined source/drain electrodes of Ti/Au (20 nm/30 nm). The insulator of polyimide (PI) is spin-coated to protect the 2D MoS_2 vdW-TFT active matrix, and via-holes through PI are opened by oxygen plasma etching. The pads of Ti/Ag/Au (20 nm/130 nm/50 nm) are photolithographically defined to provide the electrical connection between the source electrodes and the conductive micro-pyramidal PSR; the via-connections are protected by a layer of hard-baked photoresist (PR). Finally, the conductive micro-pyramidal PSR with the thickness of $\sim$ 150 µm is laminated on the 2D MoS_2 vdW-TFT active matrix, and a 50- µm-thick PI film coated with Cr/Au (5 nm/25 nm) in contact with the backside of the conductive micro-pyramidal PSR serves as a ground electrode (Figure 2.1(c)).

It is noted that the highly uniform micropyramids of the PSR (Figure 2.1(d)) requires no special stack alignment [4] and could be readily configured to a large-area pressure sensing array. The fabricated active matrix consists of 10 $\times$ 10 2D MoS_2 vdW-TFTs in an effective area of 1 $\times$ 1 cm^2 (Figure 2.1(e)) and each vdW-TFT is patterned with two pairs of source-drain electrodes with each channel length of L = 50 µm and channel width W = 100 µm (Figure 2.1(f)). In the integrated pressure sensing array, the conductive micro-pyramidal

PSR serves as a variable resistance to modulate the drain-source voltage (V_{ds}) and thus adjust the detectable output signal of drain-source current (I_{ds}). The gate lines and drain lines (i.e., the voltage bias of gate-source and drain-source) are used to address the pixels and the final two-dimensional profile of pressure spatial distribution can be readily obtained from the addressed output signals.

2.2.2 Formulation of 2D MoS_2 ink

The 2D MoS_2 nanosheets were prepared by the electrochemical intercalation of tetraethylammonium bromide into a bulk crystal and sonication-assisted exfoliation. The exfoliated nanosheets were repeatedly washed by centrifugation and dispersed in isopropanol (IPA) to form the 2D MoS_2 ink solution. The concentration of the MoS_2 ink for the TFT fabrication was adjusted by the light absorbance at 440 nm. The thickness of the deposited MoS_2 thin film was determined by the ink concentration, spin speed, and coating cycle that follows the established procedure in literature [34].

2.2.3 2D MoS_2 vdW-TFT active matrix fabrication.

The silicon wafer with about 280-nm-thick SiO_2 as substrate was cut into a desirable piece and cleaned by acetone, IPA, and deionized (DI) water, sequentially. The local back gate electrodes of Cr/Au (10 nm/20 nm) were patterned by standard photolithography, electron beam evaporation, and lift-off process. The Al_2O_3 dielectric with a thickness of about 50 nm was deposited by the ALD process at 200 °C. After oxygen plasma treatment for 5 min, the MoS_2 ink was spin-coated on the dielectric at a speed of 2,000 rpm. for 20 s for five times. To remove the unintentional impurities, the 2D MoS_2 thin film was treated by thermal annealing process (ramping from room temperature to the set temperature in $\sim$ 30min; and holding

at the set temperature for $\sim$ 1 h before cooling to room temperature in $\sim$ 30 min). The as-prepared film was then patterned into stripes (400 µm $\times$ 100 µm) by photolithography and reactive ion etching (RIE, Technics Micro-RIE Series 800). The drain-source electrodes of Ti/Au (20 nm/30 nm) were patterned with the same process of the gate electrodes. An insulator layer of PI solution (80% NMP/20% aromatic hydrocarbon, Sigma-Aldrich) was spin-coated with a speed of 4,500$-$6000 rpm for 40 s and cured in a vacuum oven at 250 °C for 1 h 30 min. To open the via-holes and drain pads, oxygen plasma etching with the power $\sim$ 250 W was employed for about 6 min, followed by soaking in buffered hydrofluoric acid to exposure gate pads. To provide the electrical connection of the source electrodes and the conductive micro-pyramidal PSR, the pads of Ti/Ag/Au (20 nm/130 nm/50 nm) were photolithographically defined. A protection layer of photoresist (AZ 5214) for the via-connection was spin-coated at a speed of 3,000 rpm. for 40 s and hard-baked at 200 °C for 20min.

2.2.4 Conductive micropyramidal PSR fabrication.

The silicon mold was prepared by wet etching with a $\sim$ 60-nm-thick Si_3N_4 mask and a fluoropolymer layer (DAIKIN industries, LTD. Chemical R&D center) was spin-coated to facilitate the release of the film of conductive micro-pyramidal PSR. The PDMS/CNT solution was obtained by mixing the PDMS solution (1 g PDMS with the 5:1 ratio of PDMS elastomer to curing agent mixed in 8 g hexane by magneton stirring for 30 min) and the CNT solution (10 mg multi-walled carbon nanotubes are dispersed in 2 g isopropanol by magnetic stirring for 5 min and bath sonication for 30 min twice). The multi-walled carbon nanotubes (MWCNTs, 3$-$6 µm length, $\geq$ 98%) were obtained from Sigma Aldrich and the PDMS (Sylgard 184) was obtained from Dow Corning. The film of conductive micro-pyramidal PSR was prepared by a standard dip-casting method in the pre-fabricated silicon mold with the PDMS/CNT solution and curing in an oven at 120 °C for about 1 h [52] and a flatter back

surface of the PSR could be obtained by carefully laminating a flat plastic substrate before curing or using less PDMS matrix in PDMS/CNT solution.

2.2.5 Device Characterization.

FEI NOVA NANOSEM 230 was used to take SEM images of the microstructure array. The pressure responses of the micro-pyramidal PSR were measured by a computer-controlled force gauge (M7-10) with a motorized test stand (ESM303) and a source measurement unit (Agilent B2902A) at the operating voltage of 1 V. The electrical properties of the 2D MoS_2 TFTs and the integrated pressure sensor were recorded by Agilent B2902A with probe station under ambient conditions and Agilent B2902A is also applied to read the output signals for the spatially resolved pressure mapping.

2.3 Result and discussion

2.3.1 Characterization of 2D MoS_2 vdW-TFTs.

The properties of the vdW-TFTs in the active matrix are critical for spatially resolved pressure sensing. To characterize the properties of the TFTs in the active matrix, we studied the 2D MoS_2 vdW-TFTs in an ambient environment before laminating the micropyramidal PSR. Due to the atomically clean contacts between the dangling bond free 2D nanosheets with minimal interfacial traps, the vdW-TFTs show highly robust electronic properties with little hysteresis. In particular, the dual-sweep of $I_{ds} - V_{ds}$ output curves under different gate-source voltages (V_{gs}) of a typical MoS_2 vdW-TFT shows the forward and backward sweeping curves essentially overlap with each other (Figure 2.2(a)). Similarly, the dual-sweep of the $I_{ds} - V_{gs}$ transfer curve ranging from the gate-source voltage 0 V to 10 V also shows little

hysteresis (Figure 2.2(b)). Such hysteresis-free behavior of the vdW-TFT is critical for the highly robust and consistent switching the active matrix.

Figure. 2(c) shows the $I_{ds} - V_{gs}$ transfer curve of a representative MoS_2 vdW-TFT annealed at 375 °C. The carrier mobility of the MoS_2 TFT is estimated to be about 5 $cm^2 \cdot V^{-1} \cdot s^{-1}$, which is higher than organic TFTs (typically, < 1 $cm^2 \cdot V^{-1} \cdot s^{-1}$) [4, 7, 16, 17]. Meanwhile the on/off ratio (I_{on}/I_{off}) can reach up to $\sim 2\times10^6$, where the off current and on current are defined as the minimum drain-source current at $V_{gs} = -9.8$ V and maximum drain-source current at $V_{gs} = 10$ V, respectively. In the practical application of the active matrix, the inactive TFTs along gate lines are generally grounded (i.e., biased with $V_{gs} = 0$ V) [27], which requires a minimal drain-source current I_{ds} at the bias $V_{gs} = 0$ to reduce the current leakage and minimize the crosstalk and thus achieve a high on/off ratio (where the off current is defined as I_{ds} at $V_{gs} = 0$ V) of the TFTs to obtain high signal-to-noise ratio (SNR). These requirements could be readily achieved for the solution-processed 2D MoS_2 vdW-TFTs by shifting the threshold voltage through thermal annealing treatments. In particular, the unintentional doping in 2D MoS_2 semiconducting film could be further removed upon annealing at a moderate temperature, leading to a lower carrier concentration and a more positive threshold voltage. The $I_{ds} - V_{gs}$ transfer curve from a representative MoS_2 vdW-TFT annealed at 400 °C shows the threshold voltage shifts from about -1.8 V to 4.1 V (Figure 2.2(d), (e)), and thus substantially reducing the off-current (I_{ds} at $V_{gs} = 0$ V) by at least three orders of magnitude while at the same time reducing subthreshold slope. The shifted threshold voltage and relatively small subthreshold slope allow the vdW-TFTs operating at relatively low voltages $V_{gs} < 10$ V, which is lower than that of typical organic TFTs (from tens to hundreds of volts) [4, 7, 16, 17]. Additionally, a positive shift in the threshold voltage would result in a lower current leakage when the TFTs along gate lines are gated at $V_{gs} = 0$ V, thus leading to a lower power consumption and a higher contrast for the practical application of pressure sensing array.

The device uniformity and yield are critical for the practical application of large-area active matrices. Benefiting from the compact 2D MoS_2 vdW thin films with full surface coverage, the $I_{ds} - V_{gs}$ transfer curves from 90 typical MoS_2 TFTs in the active matrix (Figure 2.5(a) and S1(b) in the Electronic Supplementary Material (ESM)) shows an excellent device uniformity, where the mean and standard deviation of on current and off current are 12.3 ± 2.3 µA and 6.6 ± 4.6 pA, respectively (Figure 2.2(f)), and the yields of the fabricated MoS_2 TFTs in the active matrix (Figure 2.2(g)) can reach up to 98% (Figure 2.2(h)). We also note that our devices are processed in a typical laboratory environment and the failed devices are due to the dielectric breakdown from particulate contamination, which can be improved in a better-controlled cleanroom environment. Additionally, the device-to-device variation is partially due to the non-uniform annealing thermal treatment from the limited space uniformity in the 2-inch tube furnace, which may be improved when larger furnaces are used in future studies.

2.3.2 Properties of the pressure response.

In the integrated pressure sensor, the conductive micro-pyramidal PSR is served as a variable resistance upon pressures, in which the applied pressure deforms the micropyramids and increase the contact area between the micropyramids and electrodes, reducing the resistance of the PSR (Figure 2.3(a), Figure 2.6(a) and S2(b) in ESM) to increase the drain-source voltage (V_{ds}) and thus the detectable output signal of the I_{ds} (Figure 2.1(f)). For the micropyramidal PSR, numerical simulation indicates that the stress intensity and the deformation of the PSR are concentrated on micropyramids (Figure 2.3(b)), which indicates that pressure sensing property of the PSR can be readily tuned by the spatial arrangement of micropyramids.

We examined the pressure responses of the PSR with different pyramid lengths and spacings. For the test, the PSR is sandwiched by two layers of 50-µm-thick PI film coated with Cr/Au (5 nm/25 nm) serving as electrodes with an effective area $\sim$ 1 cm^2, and the vertical stress is applied by a z-axis motorized force gauge. Figure 3c shows the representative pressure responses of the PSR with the same pyramid length of 12 µm and the spacings of 3 µm, 6 µm, 12 µm, and 24 µm in logarithmic scale, respectively, and the corresponding linear plot is shown in Figure 3d. It can be observed that the larger spacing leads to a steeper slope (i.e., higher sensitivity) in low-pressure regime ($<$ 10 kPa), but more easily reaches saturation (i.e., lower sensitivity) (Figure 2.3(c)) with larger hysteresis (Figure 2.3(d)) in medium-pressure regime (10$-$100 kPa) due to the reduced density of the pyramids. Similar characteristics are also observed in other pyramidal base lengths with the same ratios of the pyramidal base length/spacing (Figs, S3(a)-(f) in ESM), which confirms that the design of conductive micro-pyramidal PSR offers a designable approach to obtain tunable pressure sensing performances. For instance, higher sensitivity in the low-pressure regime could be attained by choosing the PSR with a properly increased spacing, while the PSR with a reduced spacing could be used to improve the working pressure range.

To demonstrate the combination of 2D MoS_2 vdW-TFTs and the micro-pyramidal PSR can convert the applied pressure into detectable electric signals, we first probed the $I_{ds} - V_{gs}$ transfer curves under different V_{ds} of a typical 2D MoS_2 vdW-TFT in the active matrix for comparison with that of an integrated pressure sensor under different pressures. The I_{ds} can be modulated by the V_{ds} and increases beyond the threshold voltage as the increase of the V_{ds} (Figure 2.3(e)). Then we tested the $I_{ds} - V_{gs}$ transfer curves under different pressures of a typical integrated pressure sensor (Figure 2.3(f)), in which the pyramidal microstructures with the spacing of 6 µm and the pyramidal base length of 6 µm was used for the demonstration. It can be observed that the I_{ds} for the integrated pressure sensor increases beyond the threshold voltage as the applied pressure increases, and shows similar trends

with rational values of I_{ds} (in μA scale) when compared to that of the TFT under different V_{ds}, which indicates that the integrated pressure sensor can transduce the applied pressure to the electric signals.

We note that the pressure response of the integrated pressure sensor is dependent on both 1) the sensing properties of micropyramidal rubber electrodes and 2) the characteristic of the 2D vdW-TFTs (Figure 2.1(f) and Fig. S4 in ESM). The high on-off ratio ($> 10^6$) of the 2D vdW-TFTs could provide a wide window to tune the sensitivity. Such integrated pressure sensor exhibits a wide sensing range (0−100 kPa) and delivers high sensitivity both in the low-pressure regime (3−4 orders of current change, i.e., the average sensitivity > 100 kPa^{-1}) and in the medium-pressure regime (more than 1 order of current change) (Figure 2.3f). The pressure sensing range of these sensors is beyond that of the microstructured sensors with conductive surface coats (typically limited in the pressure range of 0−10 kPa) [50, 52]. The sensitivity in the low-pressure regime is comparable to that of highest reported in piezoresistive ones (56−133.1 kPa^{-1} in less than 30 Pa) [54], and greatly higher than those of most common capacitive ones (less than several kPa^{-1}) [6, 7, 55]. Moreover, the minimal hysteresis of 2D vdW-TFTs could contribute the integrated pressure sensor to maintain the excellent sensing performances of the micropyramidal rubber electrodes, such as the relatively low hysteresis and fast response. As expected, the 2D vdW-TFTs based pressure sensor exhibits a rapid response ($\sim$ 50 ms) (Fig. S5 in ESM), which is comparable to most microstructured piezoresistive [52, 56] and capacitive [55] ones (tens of milliseconds), and much faster than the traditional unstructured one (several seconds) [6].

To further explore the minimum detectable signal of our sensing device, we performed the test of $I_{ds} - V_{gs}$ transfer curves of the typical integrated pressure sensor under different pressures in the low-pressure regime (0−10 kPa). Imporantly, the minimal detectable pressure observed in our study is about 600 Pa (Fig. S6 in ESM). A lower pressure may not

be detected due to the space/gap between the micropyramid electrode and the source pad, which is introduced by the protective insulating layers of polyimide (PI) and photoresist (PR) (see Figure 2.1c). We note low pressure detection limit may be improved by reducing the thickness the protective insulating layers.

2.3.3 Spatially resolved pressure mapping.

To demonstrate the spatially resolved pressure sensing capability for the integrated pressure sensor array, the number '1' with a thickness of $\sim$ 1.5 mm made by Polydimethylsiloxane (PDMS) is used to apply pressure by fingers (Fig. 4(a)). The conducive micro-pyramidal PSR with the spacing of 6 µm and the pyramidal base length of 6 µm is employed for the demonstration. The gate lines and drain lines are biased with V_{gs} = 7 V and V_{ds} = 1 V, respectively. During the measurement, the gate lines of inactive pixels are grounded to reduce the power consumption and minimize the crosstalk. The two-dimensional pressure profile is plotted by the collected output signal of drain-source current I_{ds} from each pixel. Benefiting from the combination of the high-performance 2D MoS_2 vdW-TFT active matrix and the highly uniform micropyramidal PSR, the pressure profile of the number '1' can be clearly revealed by the integrated pressure sensor array (Fig. 4(b)) and even the relative complex shape of the number '0' can be well recognized (Figs. S7(a) and S7(b) in ESM).

The spatial resolution of the current pressure sensing array is about 1 mm ($\sim$ 25.4 pixels per inch). Since the whole fabrication process from the vdW-TFT active matrix and the conductive micro-pyramidal PSR is based on photolithography, higher resolution requirements can be readily achieved for such an integrated pressure sensing array. We note that the deformation of the micropyramidal electrodes saturates at high pressure, which can be observed in Figure 2.3(c) and Figs. S3(a), S3(c) and S3(e) in ESM. Therefore, the TFTs based pressure sensing array may exhibit a decreased contrast for spatially resolved pressure

mapping under high pressures. It is also noted that the integrated pressure sensing array is biased with relatively low voltage (V_{gs} = 7 V and V_{ds} = 1 V) and by employing the reduced thickness of dielectrics and/or high-k dielectrics, such as HfO_2, the operating voltage of V_{gs} may be further reduced down to 3 V or less for directly interfacing with most commercial chips and/or integrated circuits for practical applications.

2.4 Conclusion

To conclude, we have reported an integrated pressure sensor array by combining solution-processed 2D MoS_2 vdW-TFT active matrix and conductive micro-pyramidal PSR electrodes made of PDMS/CNT composites for spatially resolved pressure sensing. In particular, the 2D MoS_2 vdW-TFTs in the active matrix deliver high on-off ratio $> 10^6$, low operating voltage < 10 V, and minimal hysteresis, along with excellent device-to-device uniformity. We have shown that the combination of the 2D vdW-TFT active matrix and the PSR readily enables spatially resolved pressure mapping. Our study demonstrates the solution-processed 2D vdW TFTs provide an effective solution for the active matrix control of the pressure sensor arrays, and we expect the 2D vdW-TFTs could be readily applied to other active matrix arrays of electronic or optoelectronic devices. In addition, more robust active matrixes and pressure sensing arrays could be obtained by using the unique vertical design [57] for such 2D vdW-TFTs.

Methods Numerical simulations were carried out using the finite element method. The parameters used in both mechanical and electrical simulations were obtained by experiments: Young's modulus of the PSR is about 3.16 MPa and the conductivity is about 3.49 S/m. To simplify the mechanical analysis, the PSR was modelled as a linear elastomer. In the electrical simulations, the geometries of micropyramids at different deformations were conditioned

by constant volume due to the Poisson ratio of about 0.5 for the PSR.

2.5 Figures and Legends

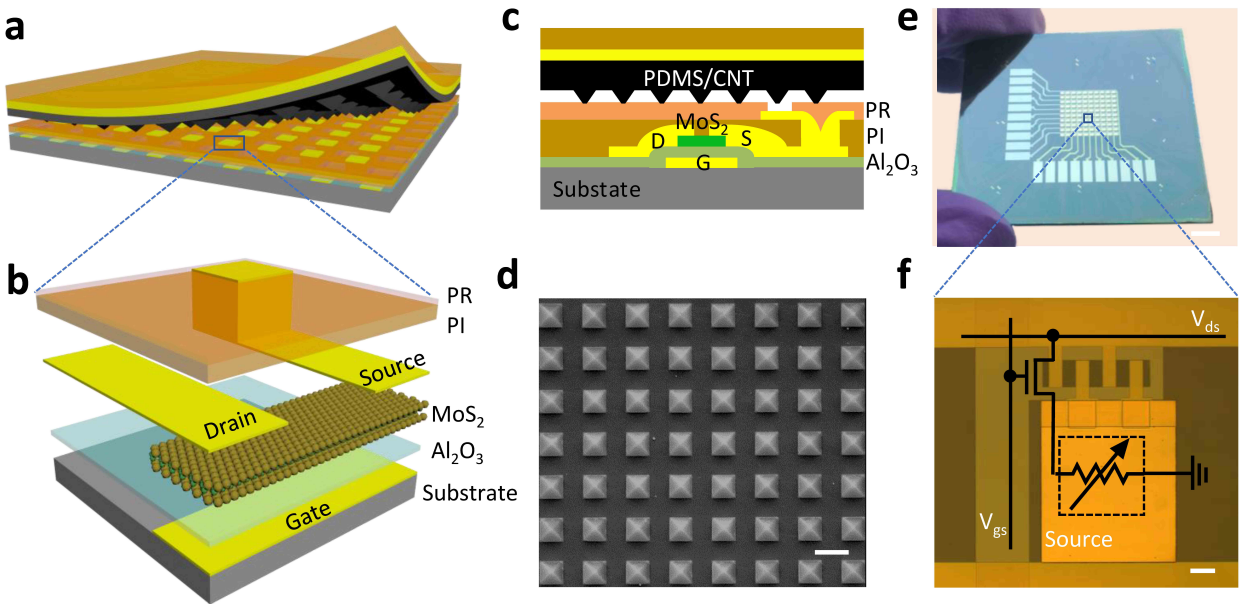

Figure 2.1: Fabrication of the integrated pressure sensing array. (a) Schematic of the integrated pressure sensing array, a combination of the 2D MoS_2 vdW-TFT active matrix (10 × 10 pixels) and the conductive micro-pyramidal PSR made of PDMS/CNT composites and (b) zoomed-in view of the 2D MoS_2 vdW-TFT active matrix. (c) Schematic of the cross-sectional view of the integrated pressure sensor. (d) Scanning electron microscope (SEM) image of the microstructured layer of the PSR. Scale bar, 10 µm. (e) Photograph of the 2D MoS_2 vdW-TFT active matrix. Scale bar, 0.5 cm. (f) Optical-microscope image of a 2D MoS_2 vdW-TFT with the circuit model, in which the gate lines and drain lines (i.e., the voltage bias of gate-source (V_{gs}) and drain-source (V_{ds})) are used to address the pixels and the source terminal is grounded through serially connecting to the PSR. Scale bar, 100 µm.

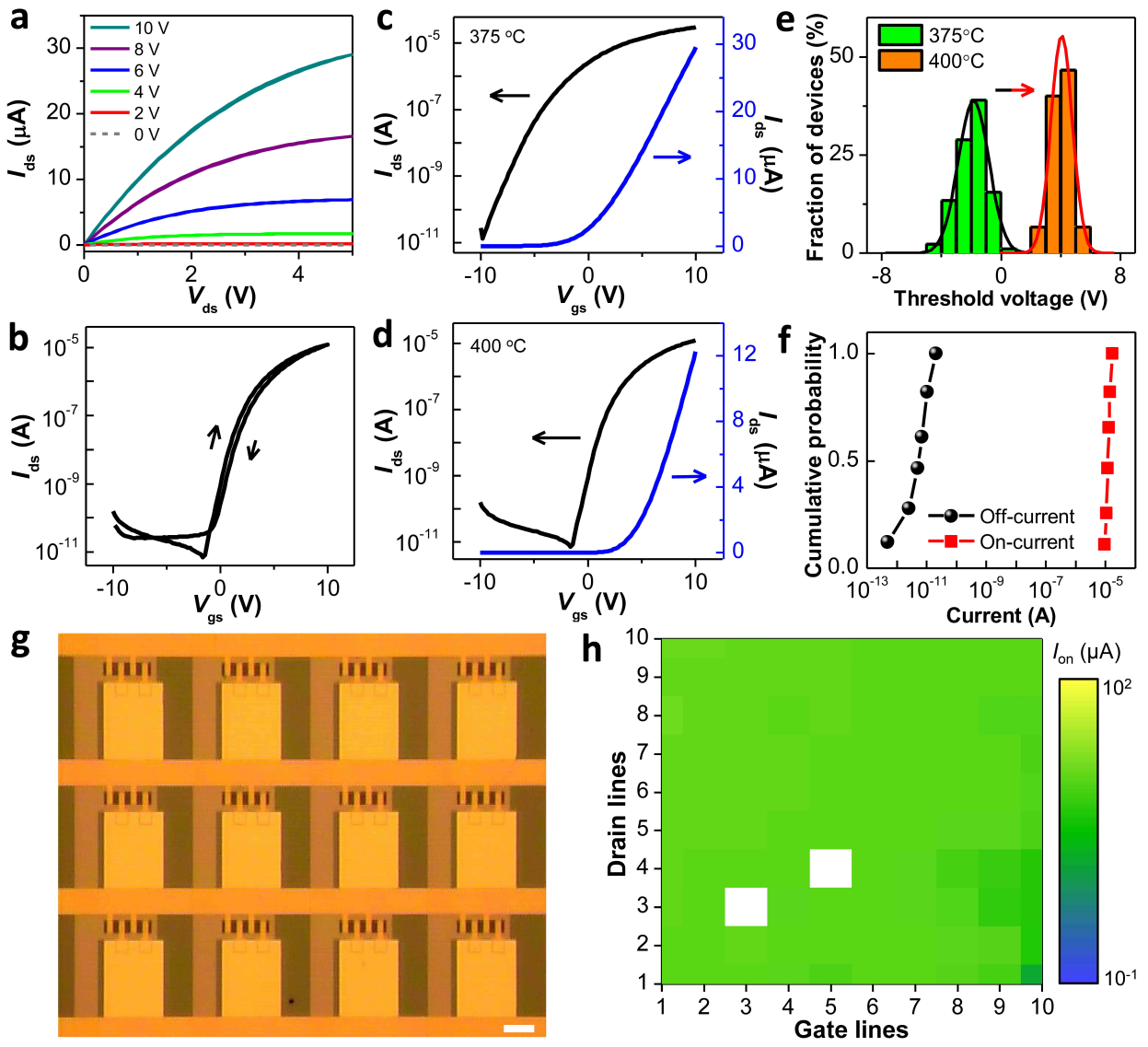

Figure 2.2: Characteristics of the 2D MoS_2 vdW-TFTs in the active matrix. (a) Dual-sweep of $I_{ds} - V_{ds}$ dual-sweep output curve at different gate-source voltage V_{gs} with a step of 2 V and (b) Dual-sweep of $I_{ds} - V_{gs}$ transfer curve at $V_{ds} = 1V$ and of the representative 2D MoS_2 vdW-TFT, which shows little hysteresis. Log plot (left axis) and linear plot (right axis) of $I_{ds} - V_{gs}$ transfer curve at $V_{ds} = 1V$ of a representative 2D MoS_2 vdW-TFT annealed at (c) 375 °C and (d) 400 °C, respectively, which indicates that the threshold voltage can be readily tuned by the annealing temperature and positively shifts as the annealing

temperature increase to minimize current leakage and reduce crosstalk. (e) The statistical distribution of threshold voltage for 90 typical 2D MoS_2 vdW-TFTs in the active matrix annealed at 375 °C (green bars) and 400 °C (orange bars) with Gaussian fits. (f) Cumulative distribution of on- and off-current for the 90 typical 2D MoS_2 vdW-TFTs annealed at 400 °C. (g) Photograph of the active matrix. Scale bar, 250 µm. (h) Color mapping of the on-current I_{on}, showing the device yields can reach up to 98% and the inactive pixels (marked with white color) are mainly due to the current leakage from the dielectric of Al_2O_3.

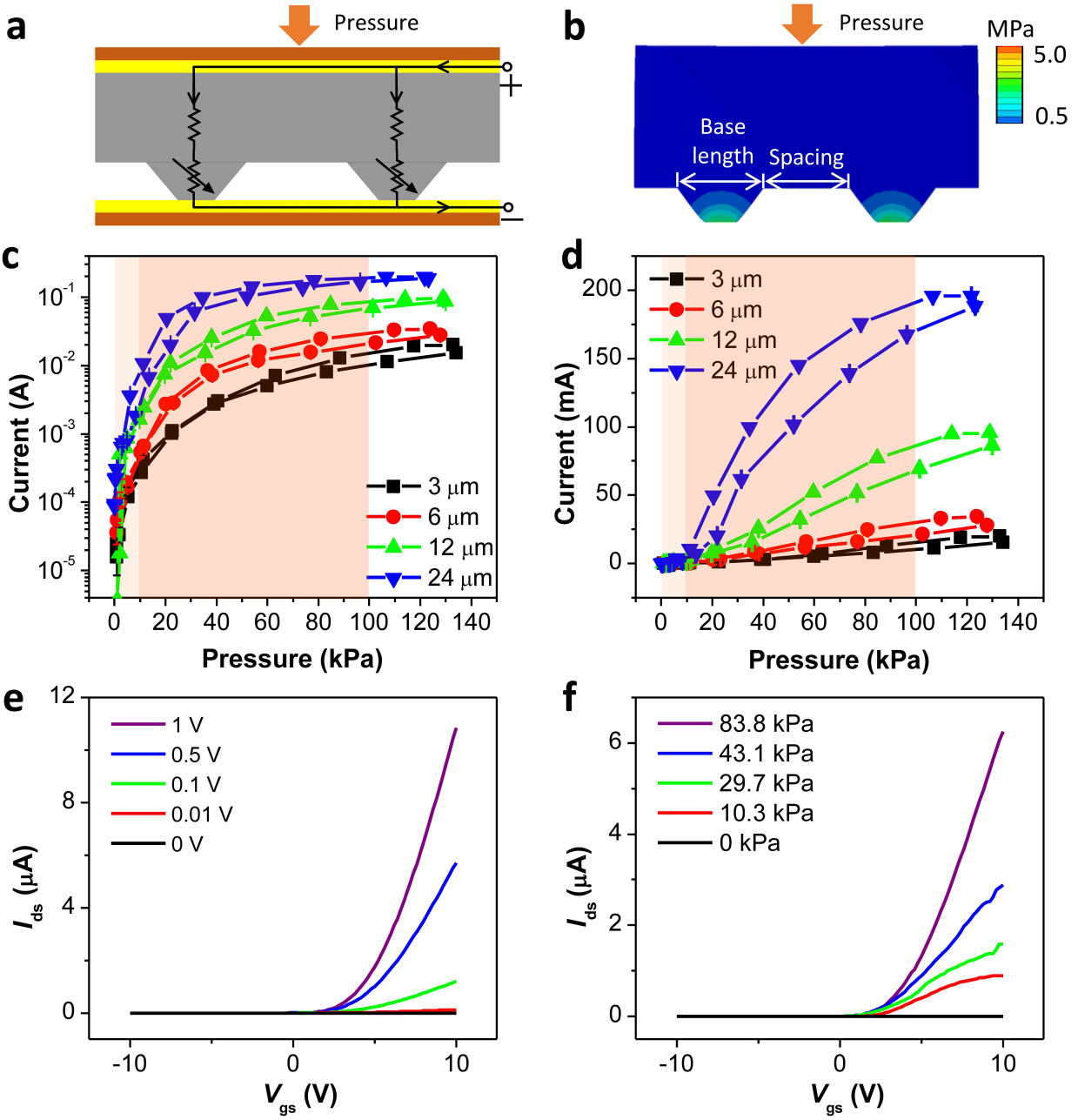

Figure 2.3: Properties of the pressure response. (a) Schematic of the working mechanism of the conductive micro-pyramidal PSR. (b) Section view of deformation and stress intensity distribution of the conductive micro-pyramidal PSR with the base length of 6 μm and spacing of 6 μm under 40 kPa by mechanical simulations. Pressure response of the conductive micro-pyramidal PSR with the same base length of 12 μm and the spacing of 3 μm, 6 μm, 12 μm,

and 24 µm in (c) logarithmic scale and (d) linear scale, respectively. (e) $I_{ds} - V_{gs}$ transfer curves of a typical 2D MoS_2 vdW-TFT under different V_{ds}. (f) $I_{ds} - V_{gs}$ transfer curves of a typical integrated pressure sensor under different pressures, where the source electrode connects to ground through the PSR in series.

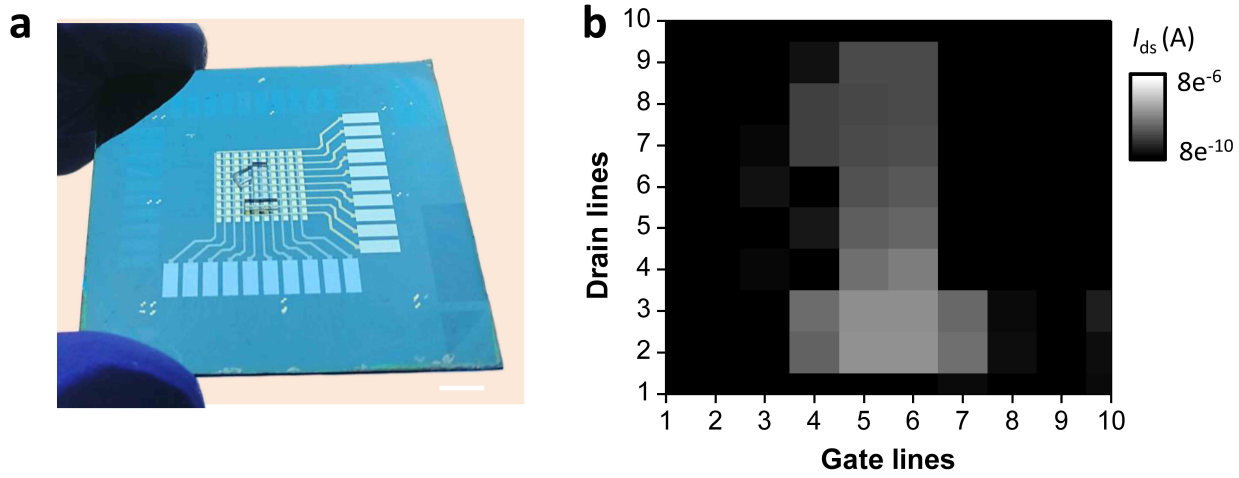

Figure 2.4: Spatially resolved pressure mapping of the integrated pressure sensing array. (a) Photograph of a fabricated 2D MoS_2 active matrix (10 × 10 pixels) with the mold '1' made by PDMS for applying pressure. Scale bar, 0.5 cm. (b) Spatially resolved current mapping corresponding to the pressure distribution. The gate lines and drain lines are biased with $V_{gs} = 7$ V and $V_{ds} = 1$ V, respectively.

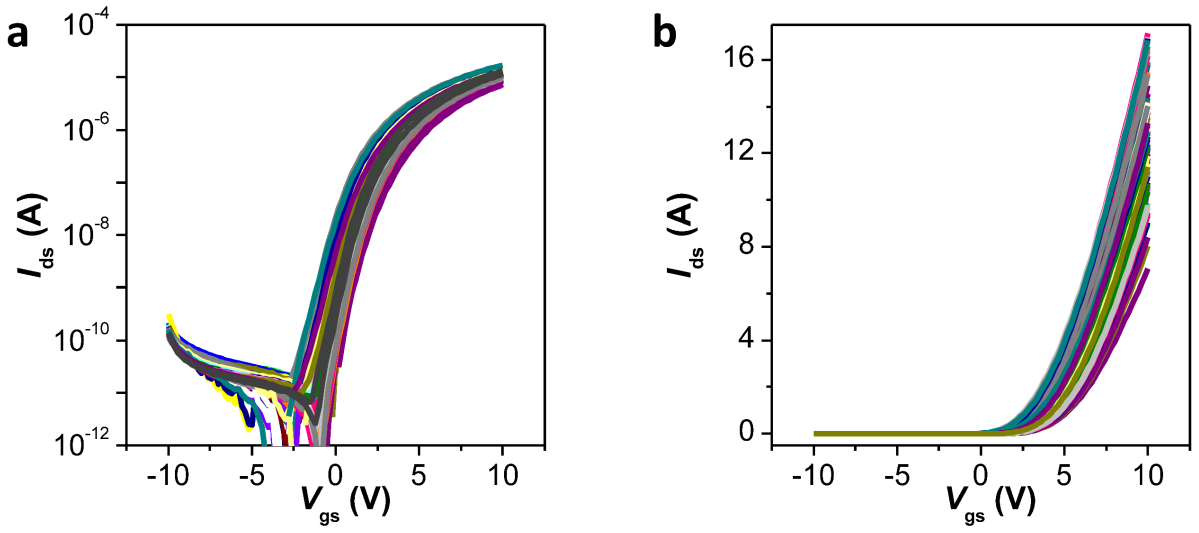

Figure 2.5: $I_{ds} - V_{gs}$ transfer curves at $V_{ds} = 1V$ of 90 typical 2D MoS_2 vdW-TFTs (a) in log scale and (b) in linear scale, showing high uniformity.

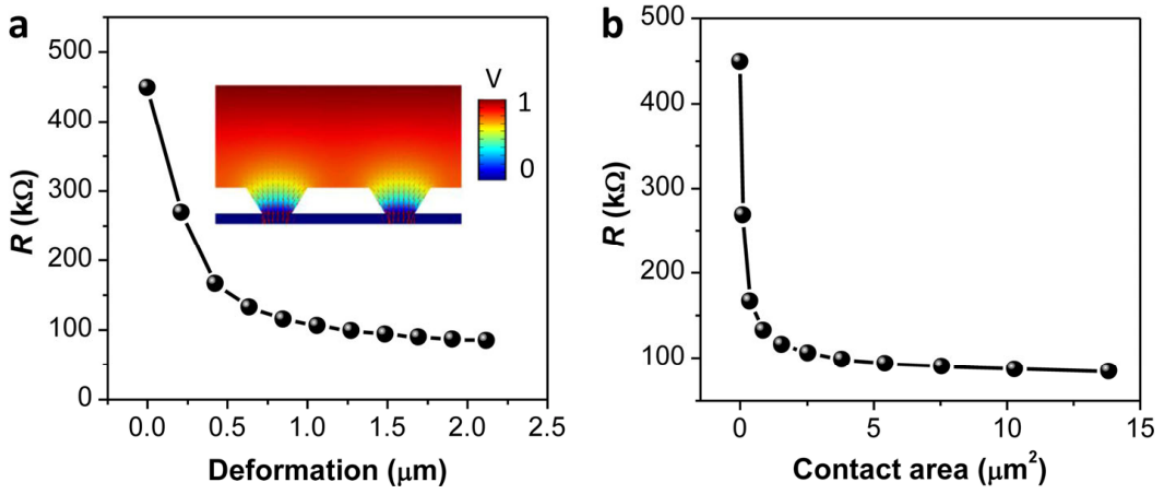

Figure 2.6: Numerical simulation of conductive micro-pyramidal PSR. (a) Resistance as a function of deformation of micropyramids and (b) resistance as a function of contact area of micropyramids with the pyramidal base length of 6 µm and the spacing of 6 µm. The deformation and the contact area of micropyramids induced by an applied pressure leads to a decrease of resistance for the conductive micropyramidal PSR.

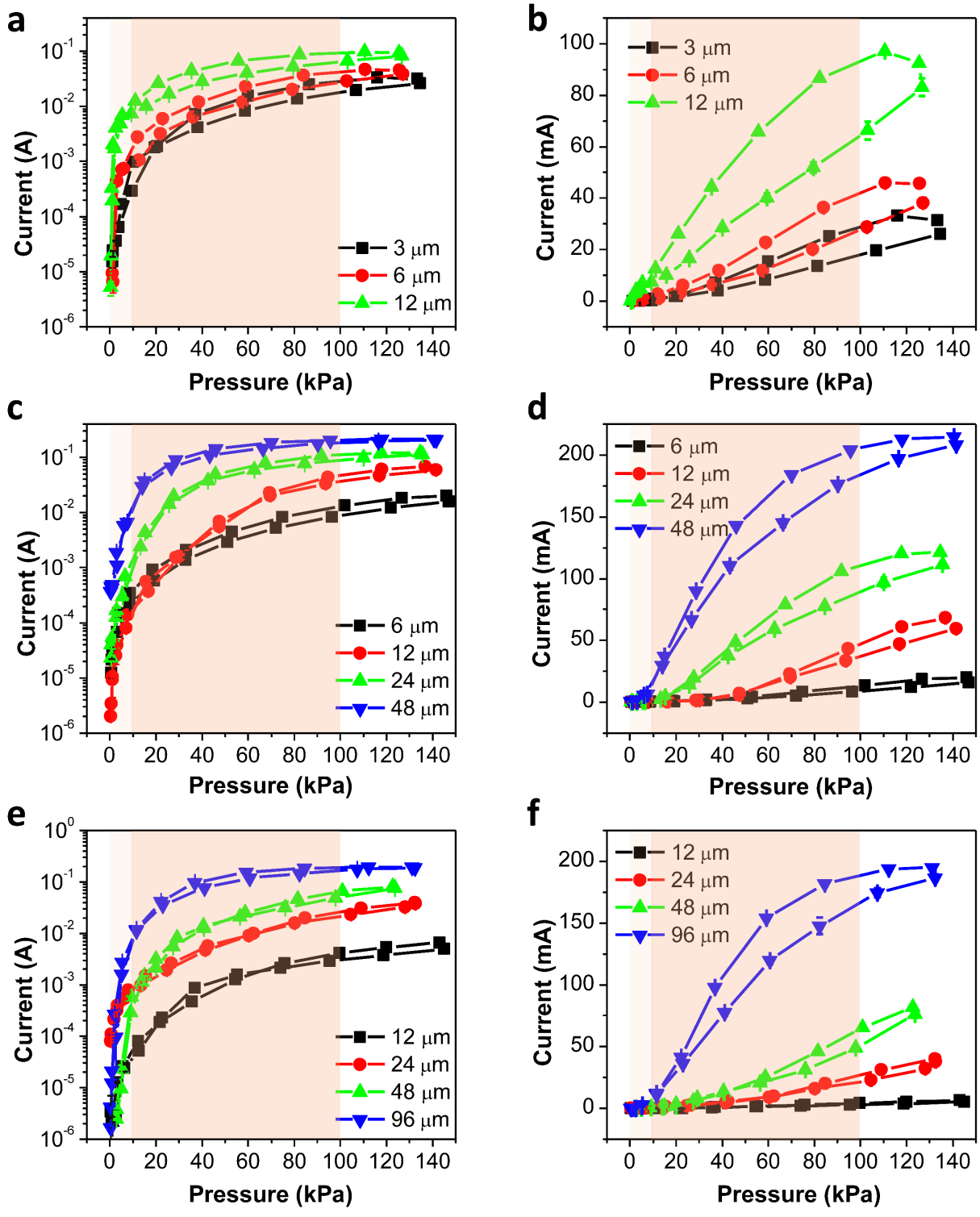

Figure 2.7: Pressure response of the conductive micro-pyramidal PSRs of different pyramidal

base lengths with the corresponding increased spacing. The same pyramidal base length of 6 µm with an increasing spacing of 3 µm, 6 µm, and 12 µm in (a) logarithmic scale and (b) linear scale, respectively; the same pyramid length of 24 µm with an increasing spacing 6 µm, 12 µm, 24 µm, and 48 µm in (c) logarithmic scale and (d) linear scale, respectively; the same pyramid length 48 µm and the spacing 12 µm, 24 µm, 48 µm, and 96 µm in (e) logarithmic scale and (f) linear scale, respectively.

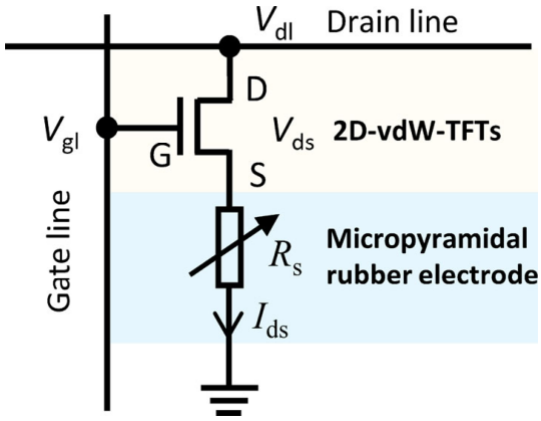

Figure 2.8: Schematic to show the working mechanism of the 2D-vdW-TFTs based pressure sensor pressure sensor.

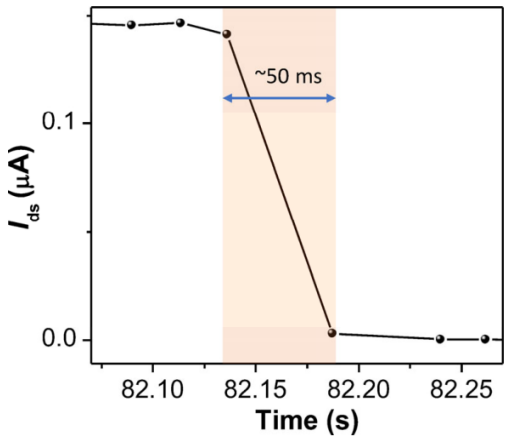

Figure 2.9: Response/relaxation time of the 2D-vdW-TFTs based pressure sensor pressure sensor.

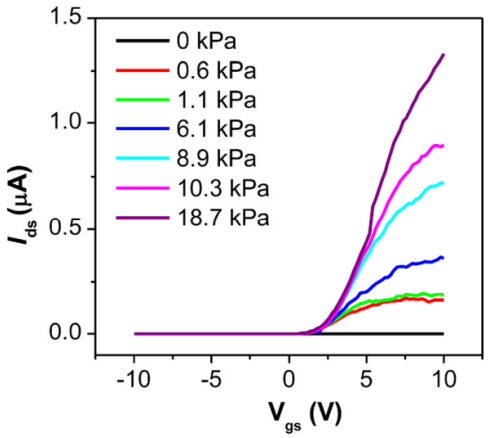

Figure 2.10: $I_{ds} - V_{gs}$ transfer curves of the typical integrated pressure sensor under different pressures in the low-pressure regime.

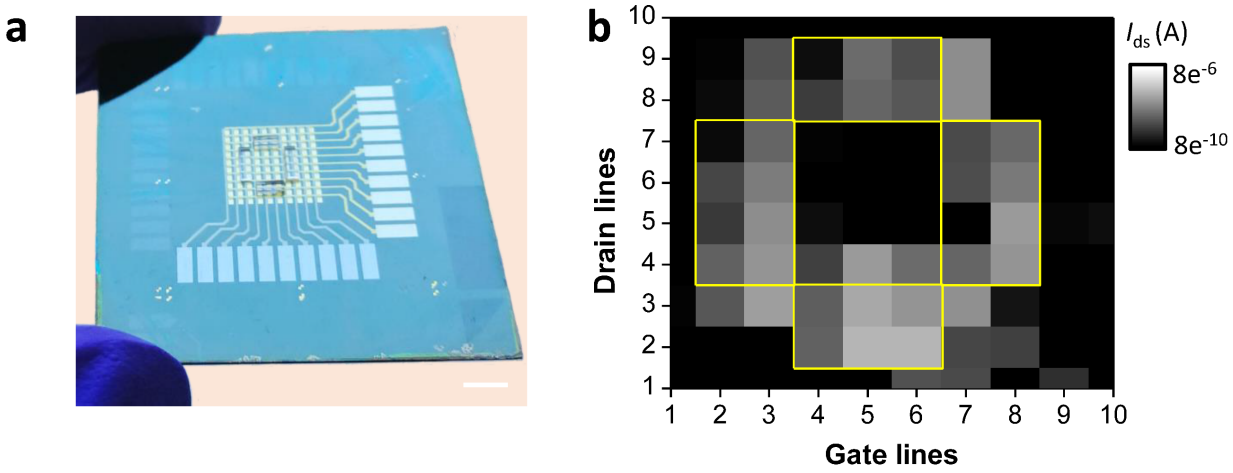

Figure 2.11: Spatially resolved pressure mapping of the integrated pressure sensing array. (a) Photograph of the 2D MoS_2 active matrix (10 × 10 pixels) with the number '0' made by PDMS for applying pressure. Scale bar, 0.5 cm. (b) Current mapping corresponding to pressure distribution. The gate lines and drain lines are biased with V_{gs} = 7 V and V_{ds} = 1 V, respectively.

References

[1] Ravinder S. Dahiya, Giorgio Metta, Maurizio Valle, and Giulio Sandini. Tactile sensing—from humans to humanoids. *IEEE Transactions on Robotics*, 26(1):1–20, 2010.

[2] Chiara Bartolozzi, Lorenzo Natale, Francesco Nori, and Giorgio Metta. Robots with a sense of touch. *Nature Materials*, 15(9):921–925, Sep 2016.

[3] Alex Chortos, Jia Liu, and Zhenan Bao. Pursuing prosthetic electronic skin. *Nature Materials*, 15(9):937–950, Sep 2016.

[4] Takao Someya, Tsuyoshi Sekitani, Shingo Iba, Yusaku Kato, Hiroshi Kawaguchi, and Takayasu Sakurai. A large-area, flexible pressure sensor matrix with organic field-effect transistors for artificial skin applications. *Proceedings of the National Academy of Sciences*, 101(27):9966–9970, 2004.

[5] Chuan Wang, David Hwang, Zhibin Yu, Kuniharu Takei, Junwoo Park, Teresa Chen, Biwu Ma, and Ali Javey. User-interactive electronic skin for instantaneous pressure visualization. *Nature Materials*, 12(10):899–904, Oct 2013.

[6] Stefan C. B. Mannsfeld, Benjamin C-K. Tee, Randall M. Stoltenberg, Christopher V. H-H. Chen, Soumendra Barman, Beinn V. O. Muir, Anatoliy N. Sokolov, Colin Reese, and Zhenan Bao. Highly sensitive flexible pressure sensors with microstructured rubber dielectric layers. *Nature Materials*, 9(10):859–864, Oct 2010.

[7] Yun-Chiao Huang, Yuan Liu, Chao Ma, Hung-Chieh Cheng, Qiyuan He, Hao Wu, Chen Wang, Cheng-Yi Lin, Yu Huang, and Xiangfeng Duan. Sensitive pressure sensors based on conductive microstructured air-gap gates and two-dimensional semiconductor transistors. *Nature Electronics*, 3(1):59–69, Jan 2020.

[8] Hongbian Li, Suye Lv, and Ying Fang. Bio-inspired micro/nanostructures for flexible and stretchable electronics. *Nano Research*, 13(5):1244–1252, May 2020.

[9] Partha Sarati Das, Ashok Chhetry, Pukar Maharjan, M. Salauddin Rasel, and Jae Yeong Park. A laser ablated graphene-based flexible self-powered pressure sensor for human gestures and finger pulse monitoring. *Nano Research*, 12(8):1789–1795, Aug 2019.

[10] Kyowon Kang, Jaejin Park, Kiho Kim, and Ki Jun Yu. Recent developments of emerging inorganic, metal and carbon-based nanomaterials for pressure sensors and their healthcare monitoring applications. *Nano Research*, 14(9):3096–3111, Sep 2021.

[11] Shuo Li, Yong Zhang, Yiliang Wang, Kailun Xia, Zhe Yin, Huimin Wang, Mingchao Zhang, Xiaoping Liang, Haojie Lu, Mengjia Zhu, Haomin Wang, Xinyi Shen, and Yingying Zhang. Physical sensors for skin-inspired electronics. *InfoMat*, 2(1):184–211, 2020.

[12] Chunya Wang, Kailun Xia, Huimin Wang, Xiaoping Liang, Zhe Yin, and Yingying Zhang. Advanced carbon for flexible and wearable electronics. *Advanced Materials*, 31(9):1801072, 2019.

[13] Li-Wei Lo, Hongyang Shi, Haochuan Wan, Zhihao Xu, Xiaobo Tan, and Chuan Wang. Inkjet-printed soft resistive pressure sensor patch for wearable electronics applications. *Advanced Materials Technologies*, 5(1):1900717, 2020.

[14] Yaping Zang, Dazhen Huang, Chong-an Di, and Daoben Zhu. Device engineered organic transistors for flexible sensing applications. *Advanced Materials*, 28(22):4549–4555, 2016.

[15] Chonghe Wang, Xiaoshi Li, Hongjie Hu, Lin Zhang, Zhenlong Huang, Muyang Lin, Zhuorui Zhang, Zhenan Yin, Brady Huang, Hua Gong, Shubha Bhaskaran, Yue Gu, Mitsutoshi Makihata, Yuxuan Guo, Yusheng Lei, Yimu Chen, Chunfeng Wang, Yang Li, Tianjiao Zhang, Zeyu Chen, Albert P. Pisano, Liangfang Zhang, Qifa Zhou, and Sheng Xu. Monitoring of the central blood pressure waveform via a conformal ultrasonic device. *Nature Biomedical Engineering*, 2(9):687–695, Sep 2018.

[16] Takao Someya, Yusaku Kato, Tsuyoshi Sekitani, Shingo Iba, Yoshiaki Noguchi, Yousuke Murase, Hiroshi Kawaguchi, and Takayasu Sakurai. Conformable, flexible, large-area

networks of pressure and thermal sensors with organic transistor active matrixes. *Proceedings of the National Academy of Sciences*, 102(35):12321–12325, 2005.

[17] Tsuyoshi Sekitani, Yoshiaki Noguchi, Kenji Hata, Takanori Fukushima, Takuzo Aida, and Takao Someya. A rubberlike stretchable active matrix using elastic conductors. *Science*, 321(5895):1468–1472, 2008.

[18] Jung Woo Lee, Renxiao Xu, Seungmin Lee, Kyung-In Jang, Yichen Yang, Anthony Banks, Ki Jun Yu, Jeonghyun Kim, Sheng Xu, Siyi Ma, Sung Woo Jang, Phillip Won, Yuhang Li, Bong Hoon Kim, Jo Young Choe, Soojeong Huh, Yong Ho Kwon, Yonggang Huang, Ungyu Paik, and John A. Rogers. Soft, thin skin-mounted power management systems and their use in wireless thermography. *Proceedings of the National Academy of Sciences*, 113(22):6131–6136, 2016.

[19] Hongjie Hu, Xuan Zhu, Chonghe Wang, Lin Zhang, Xiaoshi Li, Seunghyun Lee, Zhenlong Huang, Ruimin Chen, Zeyu Chen, Chunfeng Wang, Yue Gu, Yimu Chen, Yusheng Lei, Tianjiao Zhang, NamHeon Kim, Yuxuan Guo, Yue Teng, Wenbo Zhou, Yang Li, Akihiro Nomoto, Simone Sternini, Qifa Zhou, Matt Pharr, Francesco Lanza di Scalea, and Sheng Xu. Stretchable ultrasonic transducer arrays for three-dimensional imaging on complex surfaces. *Science Advances*, 4(3):eaar3979, 2018.

[20] Yaping Zang, Fengjiao Zhang, Dazhen Huang, Xike Gao, Chong-an Di, and Daoben Zhu. Flexible suspended gate organic thin-film transistors for ultra-sensitive pressure detection. *Nature Communications*, 6(1):6269, Mar 2015.

[21] Christopher R. Newman, C. Daniel Frisbie, Demetrio A. da Silva Filho, Jean-Luc Brédas, Paul C. Ewbank, and Kent R. Mann. Introduction to organic thin film transistors and design of n-channel organic semiconductors. *Chemistry of Materials*, 16(23):4436–4451, 2004.

[22] Ch. Pannemann, T. Diekmann, and U. Hilleringmann. Degradation of organic field-effect transistors made of pentacene. *Journal of Materials Research*, 19(7):1999–2002, Jul 2004.

[23] I Manunza and A Bonfiglio. Pressure sensing using a completely flexible organic transistor. *Biosens Bioelectron*, 22(12):2775–2779, February 2007.

[24] Henning Sirringhaus. Reliability of organic field-effect transistors. *Advanced Materials*, 21(38-39):3859–3873, 2009.

[25] Qing Cao, Hoon-sik Kim, Ninad Pimparkar, Jaydeep P. Kulkarni, Congjun Wang, Moonsub Shim, Kaushik Roy, Muhammad A. Alam, and John A. Rogers. Medium-scale carbon nanotube thin-film integrated circuits on flexible plastic substrates. *Nature*, 454(7203):495–500, Jul 2008.

[26] Chiseon Yeom, Kevin Chen, Daisuke Kiriya, Zhibin Yu, Gyoujin Cho, and Ali Javey. Large-area compliant tactile sensors using printed carbon nanotube active-matrix backplanes. *Advanced Materials*, 27(9):1561–1566, 2015.

[27] Luca Nela, Jianshi Tang, Qing Cao, George Tulevski, and Shu-Jen Han. Large-area high-performance flexible pressure sensor with carbon nanotube active matrix for electronic skin. *Nano Letters*, 18(3):2054–2059, 2018. PMID: 29442518.

[28] Kuniharu Takei, Toshitake Takahashi, Johnny C. Ho, Hyunhyub Ko, Andrew G. Gillies, Paul W. Leu, Ronald S. Fearing, and Ali Javey. Nanowire active-matrix circuitry for low-voltage macroscale artificial skin. *Nature Materials*, 9(10):821–826, Oct 2010.

[29] Xiangfeng Duan. Assembled semiconductor nanowire thin films for high-performance flexible macroelectronics. *MRS Bulletin*, 32(2):134–141, 2007.

[30] Xiangfeng Duan, Chunming Niu, Vijendra Sahi, Jian Chen, J. Wallace Parce, Stephen

Empedocles, and Jay L. Goldman. High-performance thin-film transistors using semiconductor nanowires and nanoribbons. *Nature*, 425(6955):274–278, Sep 2003.

[31] Gianluca Fiori, Francesco Bonaccorso, Giuseppe Iannaccone, Tomás Palacios, Daniel Neumaier, Alan Seabaugh, Sanjay K. Banerjee, and Luigi Colombo. Electronics based on two-dimensional materials. *Nature Nanotechnology*, 9(10):768–779, Oct 2014.

[32] Joohoon Kang, Vinod K. Sangwan, Hong-Sub Lee, Xiaolong Liu, and Mark C. Hersam. Solution-processed layered gallium telluride thin-film photodetectors. *ACS Photonics*, 5(10):3996–4002, 2018.

[33] Jung-Woo Ted Seo, Jian Zhu, Vinod K. Sangwan, Ethan B. Secor, Shay G. Wallace, and Mark C. Hersam. Fully inkjet-printed, mechanically flexible mos2 nanosheet photodetectors. *ACS Applied Materials & Interfaces*, 11(6):5675–5681, 2019. PMID: 30693759.

[34] Zhaoyang Lin, Yuan Liu, Udayabagya Halim, Mengning Ding, Yuanyue Liu, Yiliu Wang, Chuancheng Jia, Peng Chen, Xidong Duan, Chen Wang, Frank Song, Mufan Li, Chengzhang Wan, Yu Huang, and Xiangfeng Duan. Solution-processable 2d semiconductors for high-performance large-area electronics. *Nature*, 562(7726):254–258, Oct 2018.

[35] Zhaoyang Lin, Yu Huang, and Xiangfeng Duan. Van der waals thin-film electronics. *Nature Electronics*, 2(9):378–388, Sep 2019.

[36] Manish Chhowalla, Debdeep Jena, and Hua Zhang. Two-dimensional semiconductors for transistors. *Nature Reviews Materials*, 1(11):16052, Aug 2016.

[37] Deji Akinwande, Cedric Huyghebaert, Ching-Hua Wang, Martha I. Serna, Stijn Goossens, Lain-Jong Li, H.-S. Philip Wong, and Frank H. L. Koppens. Graphene and two-dimensional materials for silicon technology. *Nature*, 573(7775):507–518, Sep 2019.

[38] Qijie Liang, Qian Zhang, Jian Gou, Tingting Song, Arramel, Hao Chen, Ming Yang, Sharon Xiaodai Lim, Qixing Wang, Rui Zhu, Nikolai Yakovlev, Swee Ching Tan, Wenjing Zhang, Kostya S. Novoselov, and Andrew T. S. Wee. Performance improvement by ozone treatment of 2d pdse2. *ACS Nano*, 14(5):5668–5677, 2020. PMID: 32364379.

[39] Ruitao Lv, Joshua A. Robinson, Raymond E. Schaak, Du Sun, Yifan Sun, Thomas E. Mallouk, and Mauricio Terrones. Transition metal dichalcogenides and beyond: Synthesis, properties, and applications of single- and few-layer nanosheets. *Accounts of Chemical Research*, 48(1):56–64, 2015. PMID: 25490673.

[40] Qing Hua Wang, Kourosh Kalantar-Zadeh, Andras Kis, Jonathan N. Coleman, and Michael S. Strano. Electronics and optoelectronics of two-dimensional transition metal dichalcogenides. *Nature Nanotechnology*, 7(11):699–712, Nov 2012.

[41] F. Scott Stinner, Yuming Lai, Daniel B. Straus, Benjamin T. Diroll, David K. Kim, Christopher B. Murray, and Cherie R. Kagan. Flexible, high-speed cdse nanocrystal integrated circuits. *Nano Letters*, 15(10):7155–7160, 2015. PMID: 26407206.

[42] Luqi Tu, Rongrong Cao, Xudong Wang, Yan Chen, Shuaiqin Wu, Fang Wang, Zhen Wang, Hong Shen, Tie Lin, Peng Zhou, Xiangjian Meng, Weida Hu, Qi Liu, Jianlu Wang, Ming Liu, and Junhao Chu. Ultrasensitive negative capacitance phototransistors. *Nature Communications*, 11(1):101, Jan 2020.

[43] Yan Wang, Jong Chan Kim, Ryan J. Wu, Jenny Martinez, Xiuju Song, Jieun Yang, Fang Zhao, Andre Mkhoyan, Hu Young Jeong, and Manish Chhowalla. Van der waals contacts between three-dimensional metals and two-dimensional semiconductors. *Nature*, 568(7750):70–74, Apr 2019.

[44] Hu Xu, Haima Zhang, Zhongxun Guo, Yuwei Shan, Shiwei Wu, Jianlu Wang, Weida Hu, Hanqi Liu, Zhengzong Sun, Chen Luo, Xing Wu, Zihan Xu, David Wei Zhang,

Wenzhong Bao, and Peng Zhou. High-performance wafer-scale mos2 transistors toward practical application. *Small*, 14(48):1803465, 2018.

[45] Heejun Yang, Sung Wng Kim, Manish Chhowalla, and Young Hee Lee. Structural and quantum-state phase transitions in van der waals layered materials. *Nature Physics*, 13(10):931–937, Oct 2017.

[46] Felix Carrascoso, Hao Li, Riccardo Frisenda, and Andres Castellanos-Gomez. Strain engineering in single-, bi- and tri-layer mos2, mose2, ws2 and wse2. *Nano Research*, 14(6):1698–1703, Jun 2021.

[47] Zhiwei Li, Yawei Lv, Liwang Ren, Jia Li, Lingan Kong, Yujia Zeng, Quanyang Tao, Ruixia Wu, Huifang Ma, Bei Zhao, Di Wang, Weiqi Dang, Keqiu Chen, Lei Liao, Xidong Duan, Xiangfeng Duan, and Yuan Liu. Efficient strain modulation of 2d materials via polymer encapsulation. *Nature Communications*, 11(1):1151, Mar 2020.

[48] Hao Liu, Lin Chen, Hao Zhu, Qing-Qing Sun, Shi-Jin Ding, Peng Zhou, and David Wei Zhang. Atomic layer deposited 2d mos2 atomic crystals: from material to circuit. *Nano Research*, 13(6):1644–1650, Jun 2020.

[49] Bei Zhao, Weiqi Dang, Xiangdong Yang, Jia Li, Haihong Bao, Kai Wang, Jun Luo, Zhengwei Zhang, Bo Li, Haipeng Xie, Yuan Liu, and Xidong Duan. van der waals epitaxial growth of ultrathin metallic nise nanosheets on wse2 as high performance contacts for wse2 transistors. *Nano Research*, 12(7):1683–1689, Jul 2019.

[50] Bowen Zhu, Zhiqiang Niu, Hong Wang, Wan Ru Leow, Hua Wang, Yuangang Li, Liyan Zheng, Jun Wei, Fengwei Huo, and Xiaodong Chen. Microstructured graphene arrays for highly sensitive flexible tactile sensors. *Small*, 10(18):3625–3631, 2014.

[51] Jonghwa Park, Youngoh Lee, Jaehyung Hong, Minjeong Ha, Young-Do Jung, Hyuneui Lim, Sung Youb Kim, and Hyunhyub Ko. Giant tunneling piezoresistance of com-

posite elastomers with interlocked microdome arrays for ultrasensitive and multimodal electronic skins. *ACS Nano*, 8(5):4689–4697, 2014. PMID: 24592988.

[52] Chao Ma, Dong Xu, Yun-Chiao Huang, Peiqi Wang, Jin Huang, Jingyuan Zhou, Wenfeng Liu, Sheng-Tao Li, Yu Huang, and Xiangfeng Duan. Robust flexible pressure sensors made from conductive micropyramids for manipulation tasks. *ACS Nano*, 14(10):12866–12876, 2020. PMID: 32938185.

[53] Benjamin C.-K. Tee, Alex Chortos, Andre Berndt, Amanda Kim Nguyen, Ariane Tom, Allister McGuire, Ziliang Carter Lin, Kevin Tien, Won-Gyu Bae, Huiliang Wang, Ping Mei, Ho-Hsiu Chou, Bianxiao Cui, Karl Deisseroth, Tse Nga Ng, and Zhenan Bao. A skin-inspired organic digital mechanoreceptor. *Science*, 350(6258):313–316, 2015.

[54] Lijia Pan, Alex Chortos, Guihua Yu, Yaqun Wang, Scott Isaacson, Ranulfo Allen, Yi Shi, Reinhold Dauskardt, and Zhenan Bao. An ultra-sensitive resistive pressure sensor based on hollow-sphere microstructure induced elasticity in conducting polymer film. *Nature Communications*, 5(1):3002, Jan 2014.

[55] Rishabh B. Mishra, Nazek El-Atab, Aftab M. Hussain, and Muhammad M. Hussain. Recent progress on flexible capacitive pressure sensors: From design and materials to applications. *Advanced Materials Technologies*, 6(4):2001023, 2021.

[56] Kailun Xia, Chunya Wang, Muqiang Jian, Qi Wang, and Yingying Zhang. Cvd growth of fingerprint-like patterned 3d graphene film for an ultrasensitive pressure sensor. *Nano Research*, 11(2):1124–1134, Feb 2018.

[57] Yuan Liu, Hailong Zhou, Rui Cheng, Woojong Yu, Yu Huang, and Xiangfeng Duan. Highly flexible electronics from scalable vertical thin film transistors. *Nano Letters*, 14(3):1413–1418, 2014. PMID: 24502192.

CHAPTER 3

Broadband nonlinear modulation of incoherent light using a transparent optoelectronic neuron array

3.1 Introduction

General-purpose optical computing [1–4] and computational imaging [5, 6] would significantly benefit from optical nonlinearity [7–13]. For various practical applications involving the processing of visual information and scenes, the nonlinear optical layer must operate at low optical intensities and high frame rates, covering spatially incoherent and broadband illumination. Furthermore, energy loss through the nonlinear layers should be minimal to preserve the information carried by the optical fields. These demanding requirements on high speed, large nonlinear coefficient, low threshold intensity, low loss, and broadband response can hardly be achieved with existing nonlinear optical materials. For example, the ambient light intensity captured by digital cameras is typically below $\sim$100 mW/cm^2 [14, 15], which is many orders of magnitude weaker than the intensities employed in typical nonlinear optical processes, such as second harmonic generation ($>10^{11}$ W/cm^2) [16] and nonlinear Kerr effect ($>10^4$ W/cm^2)[17, 18]. Alternative forms of nonlinearity, such as photochromic [19, 20] and photorefractive [21–23] effects, may also be used, but these processes are typically slow, involving response time scales on the order of a few [19, 20] to tens of seconds [23]. Other forms of photorefractive effect, for example, in multiple quantum wells, are fast but present very weak nonlinearity [24–26]. Some organic photorefractive devices show millisecond responses, but rely on coherent interference to build up spatial charge patterns and create

strong nonlinear diffraction patterns, and are thus majorly adapted to holography [27, 28]. Many of these photochromic or photorefractive devices also feature strong absorption (e.g., >90%), leading to substantial losses [29]. Additionally, most of the existing nonlinear optical processes work for only a limited wavelength range.

Ultimately, the challenge lies in the tradeoff among power, speed, and transparency. Strong nonlinear responses require significant photo-induced physical/chemical changes in the material. The typical photochromatic/photorefractive devices overcome the transition energy barrier by either absorbing a sufficient number of photons in a short time interval, which either requires intense illumination far beyond the intensity of natural light or strong optical absorption that leads to low transparency and substantial energy losses [29, 30], or capturing a smaller portion of photons and slowly accumulating the photo-induced changes over a longer period, which is more transparent but with an intrinsically slow response [19, 23]. Addressing these challenges requires a fundamentally distinct working mechanism that can use a small amount of optical power to strongly modulate incoming photons.

Herein, we report a new strategy using an optoelectronic neuron array to achieve strong optical nonlinearity at low optical intensity, enabling broadband nonlinear modulation of incoherent light. This nonlinear optoelectronic neuron array is created by the heterogeneous integration of two-dimensional (2D) transparent phototransistors (TPTs) [31, 32] with liquid crystal (LC) modulators. The designed optoelectronic neuron allows spatially and temporally incoherent light in the visible wavelengths to tune its own amplitude, operating at a frame rate of >100 Hz with only ∼20% photon loss. For a proof-of-concept demonstration, we fabricated a 100×100 (10,000) optoelectronic neuron array, and demonstrated a strong nonlinear behavior under laser and white light illumination. The nonlinear filter-array was also integrated as part of a cellphone-based imaging system for intelligent glare reduction, selectively blocking intense glares with little attenuation of the weaker-intensity objects within

the field of view. Our device modeling suggests a very low optical intensity threshold of 4.2 μW/ cm^2 to generate a significant nonlinear response, and a low energy consumption of 14 fJ per photonic activation after proper device optimization. Our results demonstrate a new type of 2D optoelectronic device for nonlinear processing of low-power broadband incoherent light, which is highly desirable for image processing and visual computing systems that do not rely on intense laser inputs. It could find widespread applications in computational imaging and sensing and opens the door for new nonlinear processor designs for optical computing using ambient light.

3.2 Device design, fabrication and operation principles

Our proof-of-concept device consists of a 10,000-pixel array of parallel connected optoelectronic neurons (Figure 3.1a). Each pixel consists of an independent 2D TPT as the photogate, and an LC layer as the load resistor and the optical modulator, forming an optoelectronic neuron (Figure 3.1b). The incident light passing through the 2D-TPT layer modulates its resistance, which further regulates the voltage drop across the LC modulator to modulate the transmitted light. In this design, the light beam modulates its own amplitude depending on the incident power at each individual neuron, i.e., all the 10,000 pixels of the array work independently, all in parallel. This heterogeneously integrated architecture allows independent optimization of the TPTs and LC modules for desired performance metrics beyond the intrinsic tradeoff limits of a given material such as in conventional photochromatic or photorefractive devices. The TPTs were fabricated using solution-processed 2D van der Waals thin films (VDWTFs) [33, 34], which are constituted by staggered 2D MoS_2 nanosheets (see Method for details). With dangling-bond-free VDW interfaces among the staggered 2D nanosheets, the VDWTF features excellent semiconductor properties despite the low-temperature solution process [35, 36] (see Supplementary Fig S2a), which is essential

for the required optical response and electrical operation frequency. The transparency of the VDWTFs can be tuned with controlled film thickness. The solution process of ultrathin MoS_2 VDWTF allows depositing the semiconducting film on arbitrary substrates at wafer scale, offering an ideal material platform for making TPTs and heterogeneous integration with various optical modulators with little processing constraints.

We first prepared the MoS_2 VDWTF on a glass substrate, patterned the VDWTF into TPT channels, and then defined Cr/Au contacts. The TPT drain electrodes are connected to the supply voltage (V_{dd}), and the source electrodes are connected to a metal-ITO electrode stacked over the TPT pixel. An SU-8 layer isolates the ITO electrode from the TPT channel (except for the via) to remove the leakage current and parasitic capacitance. The top ITO electrode modulates a twisted nematic LC cell, which works both as a voltage divider and an optical modulator (Figure 3.1b)[37, 38]. Finally, a pair of orthogonal polarizers sandwiches the TPT-LC stack (see Methods for details on the material preparation and device fabrication).

Ten thousand optoelectronic neurons were connected in parallel, with the TPT terminals connected to V_{dd} and the top LC terminals connected to the common ground (GND). Each pixel works independently as an optoelectronic neuron, only controlled by the local illumination intensity at that pixel. The LC cell has a resistivity of R_{LC} $\sim$10 GΩ per pixel (see Supplementary Notes). We engineered the TPT channel to make its dark resistivity higher than R_{LC}, and its light resistivity below R_{LC}. Consequently, most of V_{dd} falls on the TPT when it is dark, leaving the LC modulator transparent under rotating polarization (Figure 3.1c). When the light is intense enough, most of V_{dd} drops on the LC cell. The strong electric field rotates the LC molecules to suppress the optical transmission, resulting in a nonlinear transmission function (Figure 3.1c,d).

3.3 2D transparent phototransistor array

We first prepared the VDWTF on a 10 cm×10 cm glass substrate to demonstrate its uniformity and transparency over a large area (Figure 3.2a). Figure 3.2b shows the TPT array under an optical microscope, which was fabricated using standard photolithography processes. The TPT layer exhibits a transmission of 88.5% at 550 nm and generally contributes to less than 20% decrease in transmission within the visible band (Figure 3.2c). Figure 3.2d shows the photoresponse of a VDWTF TPT wired out for single-device tests, where we used a 633-nm laser as the light source. The beam was defocused with a spot diameter overlapping with the 100 µm× 100µm pixel area (see Methods). Our device design needs a large ON/OFF current ratio under illumination/darkness for the corresponding optoelectronic neuron to achieve large nonlinearity. The channel current increases from 0.12 nA in the dark state to 1.96 nA at an input illumination intensity of 65.8 mW/cm^2, corresponding to an ON/OFF ratio of 16. This large resistance change is important for creating sufficient voltage modulation across the LC to produce a strong nonlinear transmission contrast (Supplementary Figure 3.6c).

Next, we used a chopper to modulate the light and study the photoresponse speed of our device at 488 nm and 633 nm wavelengths. These experiments show that the 3dB cutoff frequencies are above 3 kHz for both wavelengths (Figure 3.2e). Moreover, the responsivity at the red light is only slightly lower than that at the blue light because the bandgap of the few-layer MoS_2 is below 1.9 eV (>653 nm) [39]. We further characterized the photoresponse of 116 single pixels of individually wired TPTs (from four chips with identical process flow) under the illumination of a thermal lamp (with an intensity of ∼21 mW/cm^2, see Methods), revealing a dark/light resistance ratio of 8.95±1.30 (mean and standard deviation) (Figure 3.2f), suggesting a relatively uniform photoresponse under broadband spatially incoherent light.

3.4 Nonlinear self-amplitude modulation

We next evaluated the nonlinear amplitude modulation of the optoelectronic neuron by quantitatively analyzing the transmission of a 473-nm laser under varying incident intensity. The transmission ratios are plotted with respect to the transmission at the reference high-transmission states (i.e., at V_{dd} = 0 V for all the measurements shown in Figure 3.3a, see Methods). Our results showed that the transmission drops substantially with increasing illumination power, showing a modulation onset intensity of 0.1-10 mW/cm^2 (Figure 3.3a). The exact onset power and modulation ratio can be readily tuned by varying the supply voltage (V_{dd}). An opposite nonlinear mode can also be achieved with the same device by rotating the two polarizers to be parallel to each other: in this case, the transmission ratio is low for dim light, but increases to near unity at high illumination power (see Figure 3.3b). We further tested the nonlinearity under thermal lamp illumination and observed similar nonlinear responses with an onset illumination of ∼10,000 lux, equivalent to ∼14.7 mW/cm^2, about one order of magnitude smaller than typical sunlight intensity in ambient conditions (Figure 3.3c), demonstrating that the device is fully functional under low-intensity broadband spatially incoherent light. No transmission modulation was observed on the LC devices without the TPTs under the same test conditions, excluding a possible thermal contribution to the observed nonlinearity.

To evaluate the overall yield and uniformity of the optoelectronic neuron array, we also examined the transmission at V_{dd} = 10 V to 22 V under weak uniform white-LED illumination (Supplementary Figure 3.8 e-g). We observed two lines of malfunctioned pixels that cannot attenuate the transmitted light even at 22 V. Counts of such malfunctioning pixels suggest a yield of 98.94% for 10,000 devices fully covered in the field of view. Micro-

scopic pictures revealed the broken metal wires responsible for this failure (Supplementary Figure 3.8 h, i), likely due to particle contamination in our less strict academic cleanroom environment, suggesting no fundamental limitations in building an even larger array with high yield in a more stringent industrial fab. We further characterized the uniformity of the nonlinear response of 360 devices under different illumination levels with a cumulative plot (Figure 3.3d, see Methods for details), demonstrating distinct transmission under different illumination fluxes for all devices. Note that $V_{dd} = 0$ V does not always give the maximum transmittance for LC modulators, as observed in previous literature [40, 41]. Consequently, the transmission ratio for some optoelectronic neurons exceeds 1.0. We also note that our current optoelectronic neuron array does show a certain transmission spread among different pixels (Figure 3.3d). Similar behavior was observed in pure LC devices, suggesting that this transmission spread is primarily due to the non-uniformity of the LC modulators (see Supplementary Figure 3.7c and d). This is mainly caused by the non-uniform polyvinyl alcohol (PVA) LC alignment layer, which could be significantly improved by fabricating the LC modulators with mature industrial processes.

3.5 Integration of the optoelectronic neuron array with a cellphone camera for glare reduction

Next, we integrated our optoelectronic neuron array with a cellphone camera for intelligent glare reduction. Bright glares, such as sun glare and high beams during driving, stray laser beams in labs, or welding glares in factories, can trigger corneal reflexes or damage the human eye, as well as saturate image detectors in cameras, obscuring valuable information. Thus, bright glares are undesirable in various human/robot working conditions. Uniform attenuators or polarizers are used in sunglasses to solve this issue partially. However, such attenuators are linear optical elements and uniformly attenuate the glare and the working

environment by the same level, and thus cannot selectively maintain useful information. Ideally, a glare-reduction imaging solution should selectively dim the bright rays while efficiently capturing the useful information from the surrounding, less-bright objects, which is highly desirable for many applications.

Our nonlinear optoelectronic neuron array offers an ideal solution for this challenge as it can filter out glares at a desired intensity threshold (that can be fine-tuned electronically using V_{dd}), operating at a broad visible spectrum faster than the typical video frame rate. Therefore, it can intelligently suppress fast-moving glares over a large field-of-view with an electrically tunable intensity threshold. To showcase this capability, we constructed an imaging system using a cellphone camera (see Figure 3.4a and Supplementary Figure 3.8) to demonstrate intelligent glare reduction. A white LED array (center wavelength at 582 nm, Supplementary Figure 3.9) illuminates an aluminum diffuser to generate a uniform white background. The broadband beam passes through a patterned mask, which serves as the object. A lens projects the object image to the plane of the optoelectronic neuron array. The filtered image (forming the input scene of interest) is then captured by a cellphone camera (LGLS991, LG G4). A 473-nm laser is used to generate the (undesired) reflected intense glare at the object to evaluate glare reduction properties.

With this setup, we imaged grating-like object patterns using the cellphone camera under different conditions (Figure 3.4b-f). The patterns were clearly resolved when there were no glares (Figure 3.4b). After turning on the glare while keeping the exposure and focus condition of the cellphone camera the same (Figure 3.4c), the image was saturated by the intense scattered glare in the center, leaving little detectable features in the surrounding areas. Next, we applied $V_{dd} = 14$ V to switch ON the optoelectronic neurons. This voltage was chosen to place the LC pixels right below the nonlinear transmission threshold for ambient light, and well above the threshold when intense glares turn on the TPTs. The intense

glare beam pushed the illuminated optoelectronic neurons to the low-transmission state. As a result, the captured cellphone image shows a much dimmer glare, faithfully resolving the grating patterns and recovering the spatial information (Figure 3.4d) that was lost at V_{dd} = 0 V (Figure 3.4c). Direct transmission power measurement with a power meter shows the glare power drops by 74% when compared to its value at 0 V, while the non-glare region only showed an insignificant transmission reduction by ∼9%.

Since most current camera systems adopt auto-exposure software, we further compared the impact of our nonlinear filtering under auto-exposure settings. Turning on the auto-exposure of the cellphone camera without nonlinear filtering (V_{dd} = 0 V) leads to a complete loss of the surrounding object patterns (Figure 3.4e), which is due to the software-adjusted, reduced exposure resulting from the intense glare beams. Turning on the nonlinear filtering (V_{dd} = 14 V) under the auto-exposure mode restores the patterns of the input scene (Figure 3.4f). These results clearly highlight that our optoelectronic neuron array can rapidly reduce the negative impact of intense glares, in a way that is not possible with the standard auto-exposure features.

We also quantified the SNR of the acquired cellphone images (see the red boxes in Figure 3.4b). The image in each box is transformed into a 300×100 matrix. We computed the averages and standard deviations along the grating lines (y-axis for Box 1 in Figure 3.4b) to get the cross-sectional profiles perpendicular to the grating lines (Figure 3.4b-f right three panels, see Methods for calculation details). The noise increases by over ten times in the dark regions (Figure 3.4b and 4c, error bars for Box 1) after turning on the glare. As expected, the contrast between the black and white stripes of the input object under the glare is substantially suppressed, leaving few resolvable features. Evaluated at Box 1 in Figure 3.4b, the SNR (see Methods) is 13.8 for the no-glare case, which drops to 0.70 with the bright glare when the nonlinear filtering is off, and is restored to ∼1.34 when the nonlinear

filtering is turned on. Under the auto-exposure setting, the image SNR collected by the cellphone camera decreases to 0.26 due to the glare (without the nonlinear filtering), which increases to ∼2.31 when the nonlinear filtering is on, thanks to the suppression of the glare using the optoelectronic neuron array. We also evaluated the reduction of dynamic glares by chopping the laser glare at 3 Hz (see Supplementary Video 1). We observed a similar glare reduction performance under dynamic glare conditions. If the optoelectronic neurons were to have a response time slower than the video frame rate (60 Hz), we would expect a delayed transmission, i.e., a dark spot at the glare center right after the glare is shut off. However, no such dark spot was observed (Supplementary Figure 3.10), suggesting a nonlinear response speed much faster than the video frame rate of 60 Hz.

3.6 Discussion

We reported a unique strategy to create an optoelectronic neuron array for nonlinear modulation of broadband spatially incoherent input light at low optical intensities. Thanks to the heterogeneous integration of 2D TPT and LC modulators, the TPT and LC layers can be optimized separately without tradeoffs.

We believe the performance of our proof-of-concept demonstrations is largely limited by suboptimal material processing and device fabrication protocols (particularly related to LCs), and could be further improved by developing and adopting mature industrial processes. For example, the LC modulators in our studies show a gradual modulation slope, requiring a $\Delta V > 3$ V to switch from the high-transmission state to the low-transmission state (Supplementary Figure 3.7a). In contrast, the state-of-the-art LC modulators can achieve much more steep slopes, with a much smaller switching voltage of $\Delta V < 0.3$ V [42, 43]. This means a smaller resistance change in TPTs can trigger the LC modulators. Another

possible optimization is the lowest transmission value of LC, which relies on high-quality LC alignment layers and polarizers. Commercial LCD-based monitors can have a contrast ratio beyond 5000, compared to ∼10 in our proof-of-concept LC modulators. This would correspond to a 500-fold stronger glare reduction when the industry-quality LC modulators are integrated with our optoelectronic neuron arrays.

Our device has two important figures of merit: the threshold optical intensity to enable the nonlinear response, and the total power consumption (optical absorption plus the electrical power consumption). Our experimental device has a nonlinear intensity threshold of ∼10 mW/cm^2. It absorbs ∼20% of the incident photons in the TPT layer, corresponding to a photon power loss of 200 nW/neuron. The electrical power consumption is 1.7 nW/neuron with the typical nonlinear operation voltage at 12 V (for the chip with less resistive TPTs in Figure 3.3d-f) and a current density of 1.4 µA/cm^2. Thus, the total power consumed by our experimental device is 202 nW/neuron. Dynamic changes in the input light field could also lead to frequent charging/discharging of the LCs. However, given the large number of devices connected in parallel, the dynamic charging/discharging can be balanced with the common electrodes, and shall not create a significantly larger power consumption than the static electrical power.

We further modeled the device performance with optimized LC parameters and a better match between the TPT ON/OFF resistances and the LC resistance (see the discussion in Supplementary Note 1). This modeling indicates that the ultimate optical intensity threshold for ON/OFF switching can go below 4.2µW/cm^2 for 633-nm laser polarized along the input polarizer direction. The total power consumption per neuron scales linearly with the pixel area, and thus can be reduced substantially to 1.4 pW/neuron (5.6 µW/cm^2) by scaling the pixel size down to 5 µm, as proved feasible in LCD technologies. The LC we used (4-cyano-4'-pentylbiphenyl, common name: 5CB) supports a modulation speed above 100 Hz

[44]. Taking this modest estimation of 100 Hz as the device speed, the total power consumption can be calculated as 14 fJ per nonlinear activation. An even lower power consumption is possible with further material and device-level optimizations of LCs to increase the speed [45, 46] and scale down the device footprint [47].

We should also note that calibration may be conducted for more precise uses of these nonlinear neurons for optical computing and computational imaging in general. For this, the nonlinear optical threshold variations between the neurons of a given optoelectronic array would need to be calibrated/measured so that computer simulations or in-situ training [48, 49] can be optimized to best exploit the optical nonlinearity of each device regardless of the neuron-to-neuron variations. Alternatively, since these nonlinear responses are electrically tunable through V_{dd}, a different individual voltage can be applied to each pixel (in the form of a calibrated look-up table) to achieve more uniform thresholds by, for example, integrating a compensation resistor with each device pixel and adjusting the resistor values during the calibration [50]. In summary, we heterogeneously integrated 2D TPTs with LC modulators to form an array of 10,000 nonlinear optoelectronic neurons. Our design enables nonlinear self-amplitude modulation of spatially-incoherent broadband light, featuring a low optical intensity threshold, strong nonlinear contrast, broad spectral response, faster speed than video frame rate, and low photon loss. We further integrated this optoelectronic neuron array into a cellphone-based imaging system and demonstrated intelligent glare reduction by selectively attenuating bright glares while preserving the surrounding object information that is otherwise unrecognizable by the camera. Our device modeling suggests a very low power consumption of $\sim$14 fJ per activation after proper device optimization. This device might find various applications in, e.g., autonomous driving, photography and security cameras. Our nonlinear optoelectronic neuron array could find broad uses in computational imaging and sensing fields and opens the door for new nonlinear processor designs for optical computing using ambient light that is spatially and temporally incoherent.

3.7 Methods

3.7.1 MoS_2 ink preparation.

The raw molybdenite flake is electro-chemically intercalated by tetra-n-hexyl ammonium benzoate (THAB). 200 mg THAB is dissolved into 40 ml acetonitrile. The molybdenite is fixed on a copper electrode, which connects to the cathode of the power source. The anode is connected to a carbon electrode. The current is around 5 mA at a voltage of around 8.5 V. After 1 hr intercalation, the flake is thickened, and the intercalated layers look dark green. We cut the intercalated molybdenite and grind the pieces into small flakes with a glass rod. We dissolve 900mg polyvinylpyrrolidone (PVP) into 50 ml dimethylformamide (DMF) and mix the intercalated molybdenite into it. Next, we ultrasonicate the mixture for 1 hr. The whole solution looks dark green with small shining flakes.

The mixture is centrifuged under 12100 rpm for 15 min to remove DMF. After that, we pour the clear upper solution out and add 40 ml of isopropyl alcohol (IPA). The mixture is ultrasonicated for a second time until no sediment is visible. We repeat this process two more times to fully remove DMF. To concentrate the solution, we centrifuge under 12100 rpm for 20 min, then add 5 to 10 ml IPA (depending on the amount of intercalated flakes). We ultrasonicate the ink until there is no sediment.

We calibrate the ink concentration by dissolving 20 µl ink into 1 ml IPA and measure the UV-vis absorption (Beckman Coulter DU800 spectrophotometer). The peak should be around 380 nm with an absorption of around 1.7 for repeatable ink concentration. Finally, the calibrated ink is centrifuged at 3000 rpm for 3 min to remove the remaining large flakes. We repeat this process five times, after which the ink is ready for use.

3.7.2 Device fabrication.

We use microscope slides as the transparent glass substrate. The substrate is first treated with oxygen plasma and becomes hydrophilic. We spin-coat the MoS_2 ink on the substrate at 2000 rpm for 30 s on a spinner. The spin-coating is repeated six times to achieve a film thickness of around 10 nm. The MoS_2 VDWTF is then annealed in a furnace at 400 °C for an hour in an Ar atmosphere.

Next, we pattern the MoS_2 channel and define the TPT pixels as discussed in the paper. We evaporate HMDS on the sample for improved surface adhesion, then spin-coat SU-8 2005 photoresist on the device at 2000 rpm for 30 sec. The photoresist is pre-baked at 65 °C for 3 min, 95 °C for 3 min, and then 65 °C for 2 min, with the slow temperature change to reduce internal strain and peeling-off. Next, we expose the SU-8 with lithography (Karl Suss MA6) for 20 s to crosslink the polymer. A post-bake process identical to the pre-bake is conducted before developing with SU-8 developer for 30 seconds. The developed sample is rinsed with IPA. The lithography process opens windows on the external contact pads and the via region for connecting the TPT to the ITO pad on top. After the development, we further anneal the sample at 150 °C in Ar for 30 min, with slow increase and decrease of temperature to avoid SU-8 peeling. This further annealing improves the SU-8 crosslinking and makes it more robust to subsequent thermal and liquid processes. The SU-8 thickness is 8 µm measured by a surface profiler. It serves as a passivation for the TPT layer, as well as a thick insulating layer that reduces the parasitic capacitance between TPT and the top ITO pad.

Next, we sputter a 50-nm ITO layer on the top of the sample. Sputtered ITO has good step coverage, sufficient to connect the bottom metal pad to the upper electrode area over the

SU-8 step. The ITO is then patterned with lithography and wet etched with 1% hydrochloric acid to make the ITO pads electrically insulated from each other. The PVA alignment layer is prepared by first dissolving 5% weight of PVA (Sigma Aldrich, molecular weight 89,000-98,000) powder in 95 °C deionized water. The solution is stirred until transparent. Then the solution is spin-coated (3000 rpm, 60 s) on the sample, and another ITO glass as the top LC contact. The coated sample is annealed at 55 °C for two hours to remove water from the polymer.

After drying, the PVA is gently rubbed with cleanroom wipes along the targeted polarization direction, creating nanoscale structures used to align the liquid crystal. Glass microbeads at the diameter of 4.3 µm are dispersed in IPA (10 mg/L, ultrasonicated for an hour) and spin-coated (4000 rpm, 40 s) on the PVA layer as LC spacers. A drop of liquid crystal, 4-cyano-4'-pentylbiphenyl (5 CB) from Sigma Aldrich, is added to the chip. Then we overlap the sample with the top ITO glass slide with a PVA alignment layer on it. The edges of the two glass slides are sealed with epoxy. Large metal pads stretching out of the sealing region are fabricated and used to apply the supply voltage V_{dd}.

3.7.3 Transmission characterizations.

The LC modulator without the TPT layer was characterized for selecting the operation conditions. We illuminated a 1 cm × 1cm large uniform device with a thermal lamp and measured the transmitted illuminance with a lux meter. We observed an unstable threshold shift for DC voltage, which is related to ion and water contamination of the LC [51], so mobile ions can flow inside the LC and partially screen the modulation electrical field. To enable stable, repeatable LC modulation performance, we used a rapidly changing square wave at 500 Hz to modulate the LC (and also for the V_{dd} in TPT-LC stack measurements, with V_{dd} representing the peak-to-peak voltage). The AC field is too fast to cause slow

contamination ion drift in LC, but is still sufficient to align the liquid crystal [52]. The same AC measurement scheme was applied to the measurements in Figure 3.3 and Figure 3.4. The measurement result of the pure LC modulator is shown in Supplementary Figure 3.7. The transmission ratios were calculated as the ratio between the transmissions at the specific test condition (I_{test}) over the reference high transmission at V_{dd} = 0 V under weak light (I_{ON}), as reported in Figure 3.3 captions:

$T_R = \frac{I_{test}}{I_{ON}}$

such that I_{ON} was measured at $V_{dd} = 0$. The only exceptions for this are Figure 3.3b and the blue line in Figure 3.3c, when the two polarizers are parallel and the transmission is low at 0 V; for that case, we defined the reference high transmission I_{ON} as the transmission at a very high voltage under weak light, i.e., V_{dd} = 40 V was used. Our tested device's transmittance already converges to a maximized constant below this voltage for parallel polarizers, indicating it as a feasible definition of the reference high transmission for the parallel polarizer configuration.

The change in phase was also studied with a polarization and phase-sensitive spectroscopy method [53], with an extra 90° rotation in the transmission matrix due to the twisted LC. The extracted parameters are used to calculate the slight phase modulation accompanying the amplitude modulation, as shown in Supplementary Figure 3.7b. The phase modulation is relatively weak, at around 0.06 rad/V.

The cumulative plot in Figure 3.3d is defined by the cumulative distribution function in statistics. The cumulative counts (i.e., the vertical-axis value, normalized to 0∼100%) at a given transmission ratio T_R refers to the percentage of pixels that has a transmission ratio less than or equal to T_R, which reflects the nonlinear response's distribution over different optoelectronic neurons.

3.7.4 Light source quantification.

The thermal lamp and the white LED were measured with a spectroscopy system (Horiba Scientific). The light was fed into the system through the objective lens and filtered by the grating system to resolve the spectra. The thermal lamp was kept at a fixed power during these measurements and the nonlinear transmission tests. An attenuator was applied to control the intensity projected on the sample during the transmission test. This avoids possible spectral shifts when the thermal lamp filament is at different temperatures. The results of these measurements are shown in Supplementary Figure 3.9. The luminous efficiency of the lamp is calculated by integrating spectrally resolved luminous efficiency with the lamp spectrum. The photonic luminous efficiency is 68 lm/W. The result is comparable with the previously reported values: black body spectrum at 4000 K peaks at 700 nm and has a luminous efficiency of 55 lm/W [54]. Our lamp spectrum also peaks around 700 nm but has a much smaller infrared tail, probably due to infrared absorption on the chamber walls of the torch, leading to a higher luminous efficiency than the 4000 K black body radiation.

3.7.5 Photoresponse measurements.

The photoresponse at 633 nm and 488 nm was measured with a Horiba Raman spectroscopy system. We used the CCD camera in the Horiba system to adjust the laser spot size and overlap it with the device pixel. The incident powers on the device were calibrated with a power meter placed under the objective lens.

3.7.6 Glare reduction analysis.

We evaluated the image quality with and without glare reduction in the three boxes shown in Figure 3.4b. The image in each box is transformed into a 300 $\times$ 100 matrix (M_{jk}) by

summing up the RGB values. We calculated the mean intensity of the N = 100 image pixels along the direction of the grating lines to evaluate the averaged pattern ($\overline{\mathrm{I_j}}$):

$$\bar{\mathrm{I}}_{\mathrm{j}} = \frac{1}{N}\sum_{k=1}^{N} \mathrm{M_{jk}} \tag{3.1}$$

This vector, $\bar{\mathrm{I}}_{\mathrm{j}}$, is plotted with solid lines in Figure 3.4b-f. The corrected sample standard deviations ($\mathrm{s_j}$) along the 100 image pixels are also evaluated for each column and plotted as the error bars in Figure 3.4b-f:

$$\mathrm{S_j} = \sqrt{\frac{1}{N-1}\sum_{k=1}^{N}\left(\mathrm{M_{jk}} - \bar{\mathrm{I}}_j\right)^2} \tag{3.2}$$

We defined the image signal as the difference between the average intensity in the bright region ($\mathrm{R_{bright}}$, with $\mathrm{R_{bright}}$ pixels) and the dark region ($\mathrm{R_{dark}}$, with $\mathrm{N_{dark}}$ pixels) of the grating lines. The bright/dark regions were selected as the pixels with the top/bottom 25% intensities in the dynamic range, which is defined by the maximum intensity minus the minimum intensity in the box. The bright/dark regions were only segmented once using the no-glare image in Figure 3.4b, Box 1, and applied to all subsequent SNR evaluations at different glare, voltage, and exposure settings. The SNR was calculated as the ratio of the signal over the standard deviation in the dark regions:

$$\bar{\mathrm{I}}_{bright} = \frac{1}{\mathrm{N}_{bright}}\sum_{jk\in \mathrm{R}_{bright}} \mathrm{M}_{jk} \tag{3.3}$$

$$\bar{\mathrm{I}}_{dark} = \frac{1}{\mathrm{N}_{dark}}\sum_{jk\in \mathrm{R}_{dark}} \mathrm{M}_{jk} \tag{3.4}$$

$$\mathrm{SNR} = \frac{\bar{\mathrm{I}}_{bright} - \bar{\mathrm{I}}_{dark}}{\delta} \tag{3.5}$$

δ is the standard deviation of all the data points within dark grating lines in the box:

$$\delta = \sqrt{\frac{1}{\mathrm{N}_{dark}-1}\sum_{jk\in \mathrm{R}_{dark}}\left(\mathrm{M_{jk}} - \bar{\mathrm{I}}_{dark}\right)^2} \tag{3.6}$$

where $\mathrm{N_{dark}}$ is the total number of image data points in the dark regions of the grating lines.

3.8 Supplementary Note 1.

We first set a few basic parameters of the TPT-LC system with the experimental data. Material level optimizations may significantly improve the device performance beyond the calculated results based on our experimental parameters, which will not be discussed. We tested TPT-free, large-area LC modulators with the identical process flow to our optoelectronic neurons. At the threshold voltage Vth = 1.5 V, the current density is J = 1.4 μA/cm^2. Next, we tested the TPT-LC stack (the chip with less resistive TPTs corresponding to Figure 3.3d-f) and observed an averaged V_{dd} = 12 V for the LC layer to enter the threshold. As a result, we can derive the average TPT resistivity at a weak intensity from:

$$V_{LC} = \frac{R_{LC}}{R_{PD}^{(D)} + R_{LC}} V_{dd} \tag{3.7}$$

The LC resistivity per pixel (100 μm by 100 μm for our experimental devices) is = 1.5 V / 1.4 μA × 10^4 ≈ 10G Ω. The dark resistance of the square MoS_2 channel is then $R_{PD}^{(D)}$=70G Ω. The capacitance of the liquid crystal is calculated with the permittivity of 5CB (ε_r≈18) and PVA (ε_r≈2, slightly varies depending on sample preparation conditions[Reddy P L, Deshmukh K, Chidambaram K, et al. Dielectric properties of polyvinyl alcohol (PVA) nanocomposites filled with green synthesized zinc sulphide (ZnS) nanoparticles[J]. Journal of Materials Science: Materials in Electronics, 2019, 30(5): 4676-4687.]), with the thickness of PVA around 1 m for both the upper and lower LC alignment layers. The ultimate capacitance is majorly limited by the lower-permittivity PVA layers and is around 0.71 nF/cm^2. The equivalent RC circuit for a TPT-LC pixel is shown in Figure 3.11a. The LC driving voltage is related to the frequency following the equation:

$$V_{LC} = V_{dd} \frac{\frac{R_{LC}}{1+j\omega C R_{LC}}}{R_{PD}^{(D)} + \frac{R_{LC}}{1+j\omega C R_{LC}}} \tag{3.8}$$

The 3dB cutoff frequency is then:

$$f_{3dB} = \frac{1}{2\pi} \left[C \frac{R_{LC} R_{PD}^{(D)}}{R_{LC} + R_{PD}^{(D)}} \right]^{-1} \tag{3.9}$$

Take the experimental values of our devices, f_{3dB} 256 Hz. This RC delay, together with the intrinsic response time of LC molecules, limits the device response to a few hundred hertz. At the same time, the TPT layer can operate beyond kHz frequencies, and can be heterogeneously integrated with other types of modulators for higher operation speed.

Next, we discuss the scaling laws of the device. Since the two sources of power consumption, the photon absorption and the static electrical power consumption, are both fixed with the total array area, increasing the number of pixels per area (N) will result in a reduction in the power consumption per activation proportional to N^{-1}. On the other hand, the product of $C \ldots R_{LC}$remains constant during the scaling down, so the speed of the device remains constant as long as the TPT resistivity increases accordingly. The TPT resistivity can be well controlled by orders of magnitudes with changed channel geometry, annealing, and electrostatic gating for the VDWTF phototransistors. Considering the thickness of the LC modulation layer, edge effects of electric fields between parallel capacitors will become nontrivial when the pixel size is below 5 µm for the current design. However, it is possible to reduce the LC thickness to sub-micrometers, so that the pixel size can go below 1 µm [47]. Here we estimate the ultimate power consumption per pixel based on a 5-µm device size. This avoids imprecise estimations when the LC cell resistivity changes with a thinner LC layer thickness. The electrical power consumption of the optoelectronic neurons is:

$$P_{elec} = \frac{R_{PD}^{(D)} + R_{LC}}{R_{LC}} V_{th} I_{total} \tag{3.10}$$

As discussed in the paper, the modulation from a high-transmission state to a low-transmission state can be achieved in Δ V_{LC}=0.3V with optimized LC modulator structures. This can help us reduce the incidental intensity to trigger optoelectronic nonlinearity. The voltage change in LC is related to the TPT resistivity change by:

$$\Delta V_{LC} = \left(\frac{R_{PD}^{(D)} + R_{LC}}{R_{PD}^{(L)} + R_{LC}} - 1 \right) V_{th} \tag{3.11}$$

The TPT resistivity at different intensity levels can be fitted with photocurrent measurements at the wavelength of 633 nm, as shown in Figure 3.11b. There is a good linear fit of points suggesting an approximate relationship between the total channel current I_{ds} and the incident power P_{inc}:

$$I_{ds}^{(L)} = \left(1 + \alpha P_{ins}^{\beta}\right) I_{ds}^{(D)} \tag{3.12}$$

The fitting parameters are extracted to be α =3.411 and β =0.3675 , with P_{inc} in the unit of mW/cm^2. The actual responsivity at lower optical powers may exceed the fitted value, as defect saturation effects are much weaker under lower power illuminations. As a result, the presented estimation provides an upper bound of the necessary optical power for producing sufficient nonlinearity. Take together Eq. S5 and Eq. S6, we have:

$$\left(1 + \alpha P_{ins}^{\beta}\right)^{-1} = (1+\gamma)^{-1} - \frac{\gamma\varphi}{1+\gamma} \tag{3.13}$$

γ and φ are dimensionless parameters for brevity. Consequently, the minimum necessary intensity is given by:

$$P_{inc} = \left[\frac{\gamma\,(1+\varphi)}{\alpha\,(1-\gamma\varphi)}\right]^{\frac{1}{\beta}} \tag{3.14}$$

Taken the estimated parameter from our experimental devices, γ =3.3 and φ=0.14, we have P_{inc}=7.1mW/cm^2. For the potentially optimized devices with γ=0.15 (typical nematic LC parameters taken from ref [43]) and φ=1.4 (from the optimized device with minimized total power consumption, see later discussions), we would have P_{inc}=4.2μW/cm^2, much smaller than the unoptimized devices.

The total power consumption of the ideal device is:

$$P_{total} = \frac{1+\varphi}{\varphi} V_{th} I_{total} + A\left[\frac{\gamma\,(1+\varphi)}{\alpha\,(1-\gamma\varphi)}\right]^{\frac{1}{\beta}} \tag{3.15}$$

A = 0.2 is the photon loss through the TPT layer. Picking a larger value favors a smaller electrical power consumption, as a smaller V_{dd} is necessary to drive the device. However, it results in a larger optical intensity to create a larger TPT resistivity change that shuts off

the LC modulator. Supplementary Figure 3.7c plots the power consumptions from photon loss and current flow. The minimum power consumption is 5.6 μW/cm^2 at φ=1.4. Considering a scaled-down pixel size of 5 μm, the power consumption is 1.4 pW/pixel. With an operation frequency of 100 Hz, the device can perform a nonlinear optical calculation at 14 fJ per activation.

3.9 Figures and Legends

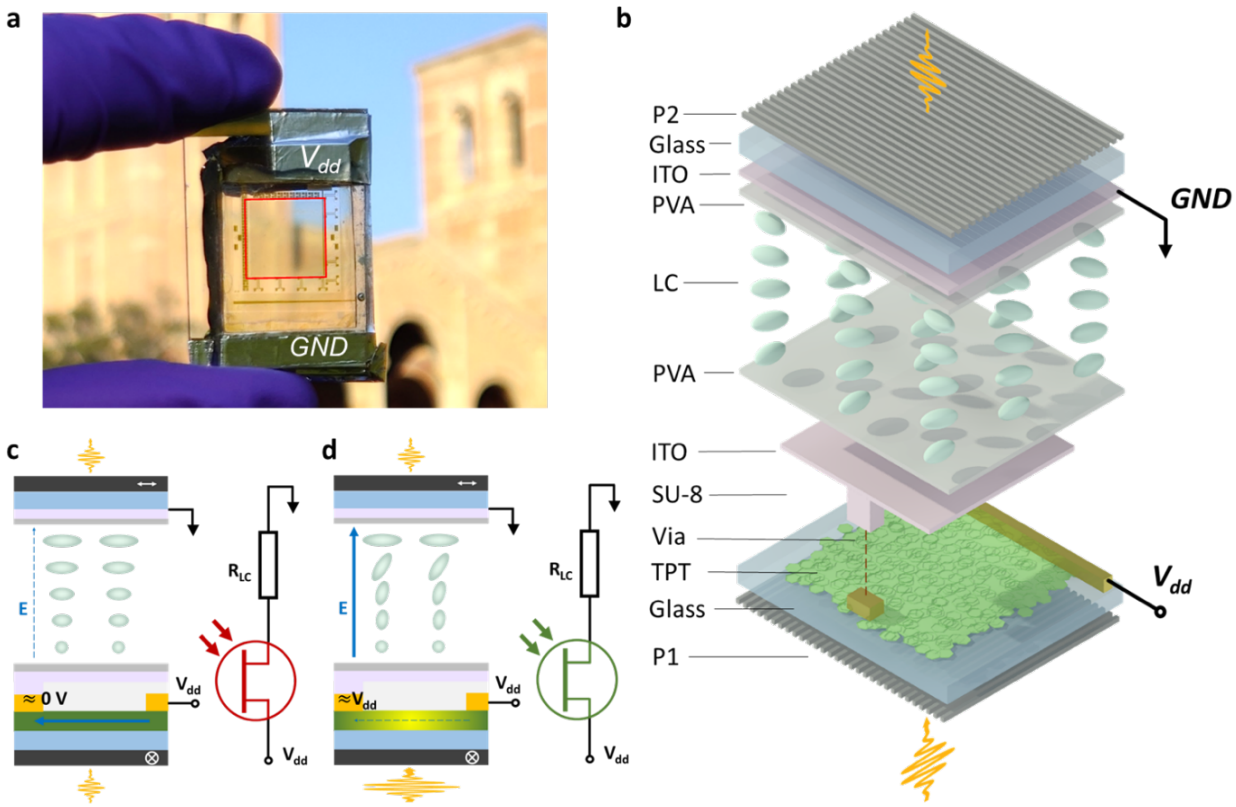

Figure 3.1: Device configuration and working mechanism. a. A photo of the packaged opto-electronic neuron array (marked by the red box, polarizers not included). There are 10,000 pixels within an array of 100100 covering 1 cm×1 cm area, showing decent transparency. b. Schematic illustration of the device structure disassembled by layers. The light is incident from the bottom, passing through the first polarizer (P1) and then through a glass substrate and a TPT made with MoS_2 VDWTF. An SU-8 insulating layer isolates an ITO electrode from the TPT channel. The ITO electrode is only locally connected to a single TPT and insulated from nearby pixels. A polyvinyl alcohol (PVA) alignment layer controls the LC molecules' orientation at the PVA-LC interface. Another orthogonal alignment layer is on top of the PVA layer, so the LC molecules gradually twist in the cell. Electrical current flows through the TPT to the ITO layer in the middle, then to the top ITO layer, which

is grounded. The LC cell also works as an optically inactive resistor. c. Self-amplitude modulation of light based on the optoelectrical operation of the TPT-LC stack. The TPT is highly resistive at low input optical power, so most electrical fields (blue arrow, thick solid line representing strong field, thin dashed line representing weak field) fall on the TPT. The LC is unperturbed and remains transmissive. The equivalent circuit is shown on the right. The TPT is highly resistive and highlighted in red. d. At high input optical power, the TPT becomes conductive (marked in green in the equivalent circuit), so most electrical field falls on the LC layer, shutting off the optical transmission.

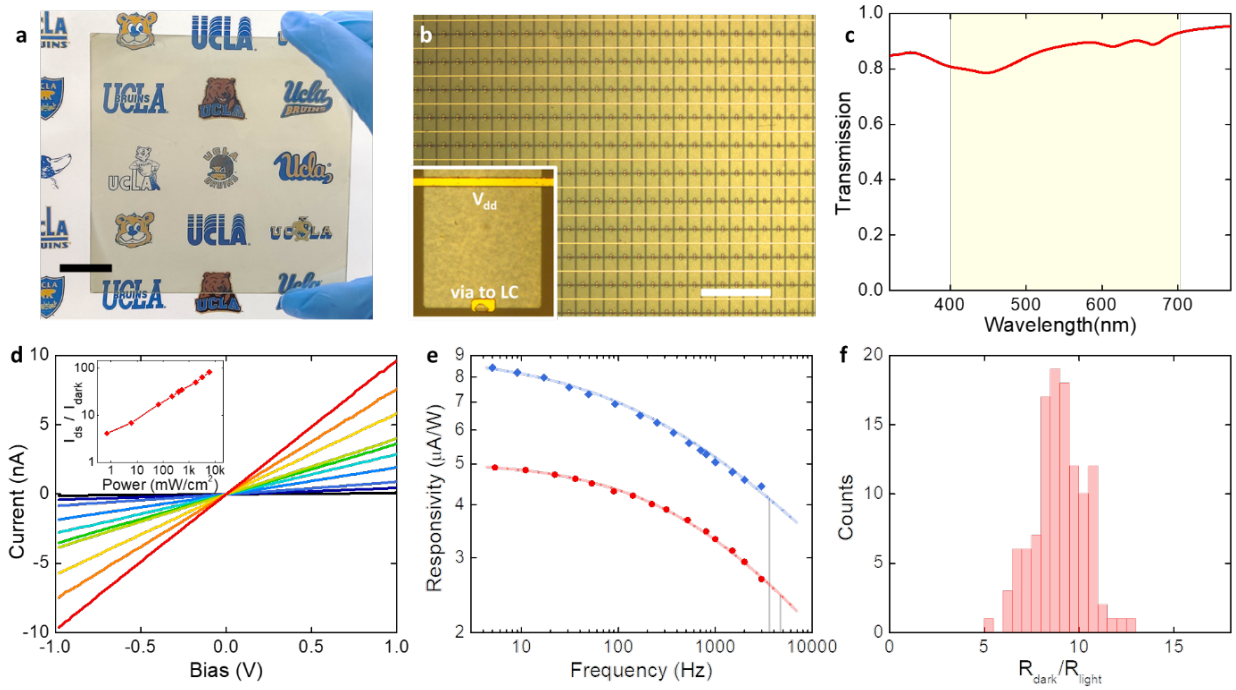

Figure 3.2: Performance quantification of the TPTs. a. A photo of a 10 cm 10 cm glass substrate coated with the MoS_2 VDWTF, demonstrating good scalability and transparency. Scale bar: 2 cm. b. A microscopic image of the TPT array. The gold wires are connected directly to V_{dd}. The vias (the small gold spots) connect to the ITO electrode covering the entire pixel area. Scale bar: 500 μm. The contrast is large despite the high transparency of the device since the microscope works in reflection mode. c. The transmission spectrum of the VDWTF in the visible range (highlighted in yellow shade). d. The photocurrent of a separately wired-out TPT at sweeping source-drain bias under 633-nm laser. Black to red (lower to higher): under the illumination intensity of 0, 0.7, 6.0, 65.8, 220, 393, 531, 1740, 3140, and 5920 mW/cm^2, respectively. Inset: the ratio of the channel current over dark current at different optical intensities. e. The responsivity measured by a lock-in amplifier at different laser chopping frequencies. Blue: data from a 488-nm laser at 0.46 mW (4.6 μW/cm^2) on a single pixel; red: data from a 633-nm laser at 0.59 mW (5.9 W/cm^2). Gray lines indicate the extrapolated 3 dB cutoff frequencies at 3.5 kHz and 4.7 kHz, respectively, which are above the chopping frequency available in our lab. f. The ratio of the dark resistances

over the light resistances of 116 TPTs on four chips with identical process flow. On each chip, 29 devices were tested, spanning an area of 14 mm×10 mm surrounding the arrayed TPTs. The light resistances were measured under a thermal lamp at an illuminance of 1.4×10^4 lux. The thermal lamp spectrum is shown in Supplementary Figure 3.9, with a center wavelength of 713 nm and a full-width-at-half-maximum (FWHM) bandwidth of 175 nm. The channel bias was 1 V for e and f.

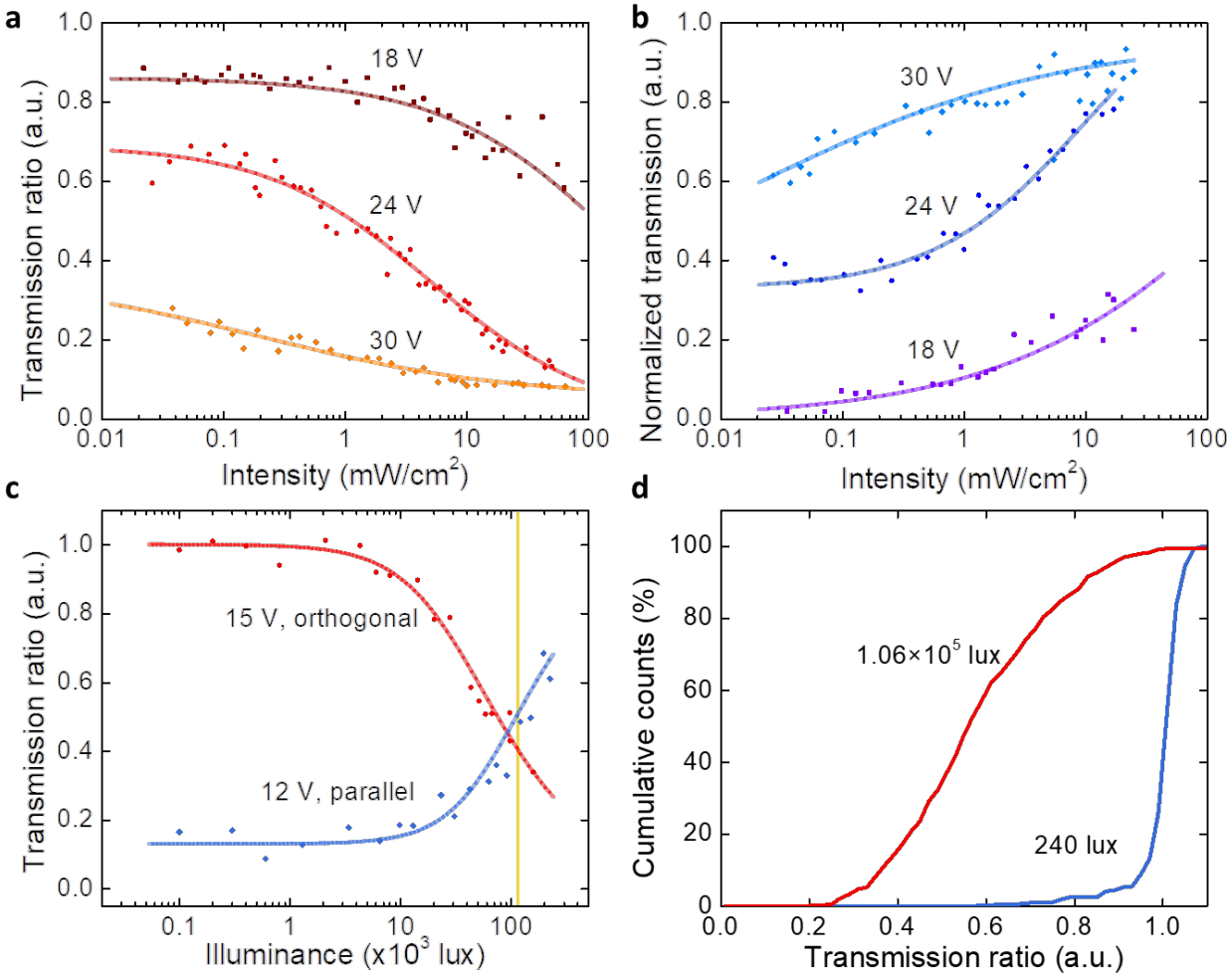

Figure 3.3: Nonlinear transmission characterization. a. The dependence of the transmission ratio on the incident intensity at a wavelength of 473 nm. The two polarizers are orthogonal, as illustrated in Figure 3.1a. b. Opposite nonlinear behavior at 473 nm when the two polarizers are parallel. c. Nonlinear behavior with thermal lamp illumination under two different voltages and polarizer orientations. The typical direct outdoor sunlight illuminance range is also highlighted (yellow line) [55]. d. Cumulative plot for the transmission ratio value distribution of 360 individual TPT-LC pixels at weak (blue) and intense (red) thermal lamp illumination at V_{dd} = 12 V. The transmission ratios are normalized by the reference high transmission of the device at the corresponding test condition, V_{dd} = 0 V for orthogonal

polarizers and $V_{dd} = 40$ V for vertical polarizers (see Methods). The incident laser in a and b was polarized along the polarizer (P1) direction. Data in a, b, and the glare reduction reported in Figure 3.4 were measured on the same chip. Data in c and d were collected from another chip with slightly lower TPT resistivities.

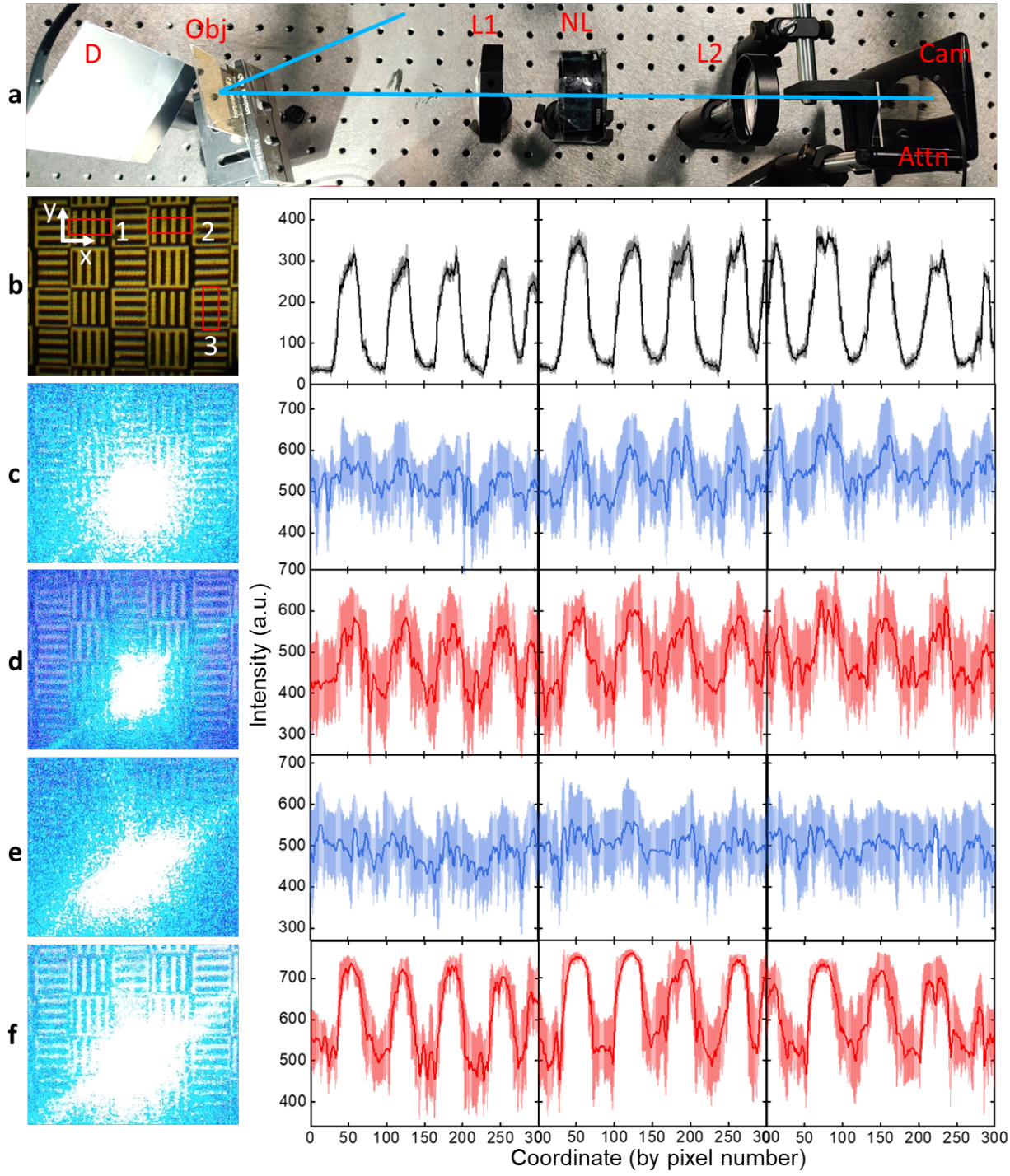

Figure 3.4: Nonlinear transmission characterization. a. The dependence of the transmission ratio on the incident intensity at a wavelength of 473 nm. The two polarizers are orthogonal,

as illustrated in Figure 3.1a. b. Opposite nonlinear behavior at 473 nm when the two polarizers are parallel. c. Nonlinear behavior with thermal lamp illumination under two different voltages and polarizer orientations. The typical direct outdoor sunlight illuminance range is also highlighted (yellow line) [55]. d. Cumulative plot for the transmission ratio value distribution of 360 individual TPT-LC pixels at weak (blue) and intense (red) thermal lamp illumination at V_{dd} = 12 V. The transmission ratios are normalized by the reference high transmission of the device at the corresponding test condition, V_{dd} = 0 V for orthogonal polarizers and V_{dd} = 40 V for vertical polarizers (see Methods). The incident laser in a and b was polarized along the polarizer (P1) direction. Data in a, b, and the glare reduction reported in Figure 3.4 were measured on the same chip. Data in c and d were collected from another chip with slightly lower TPT resistivities.

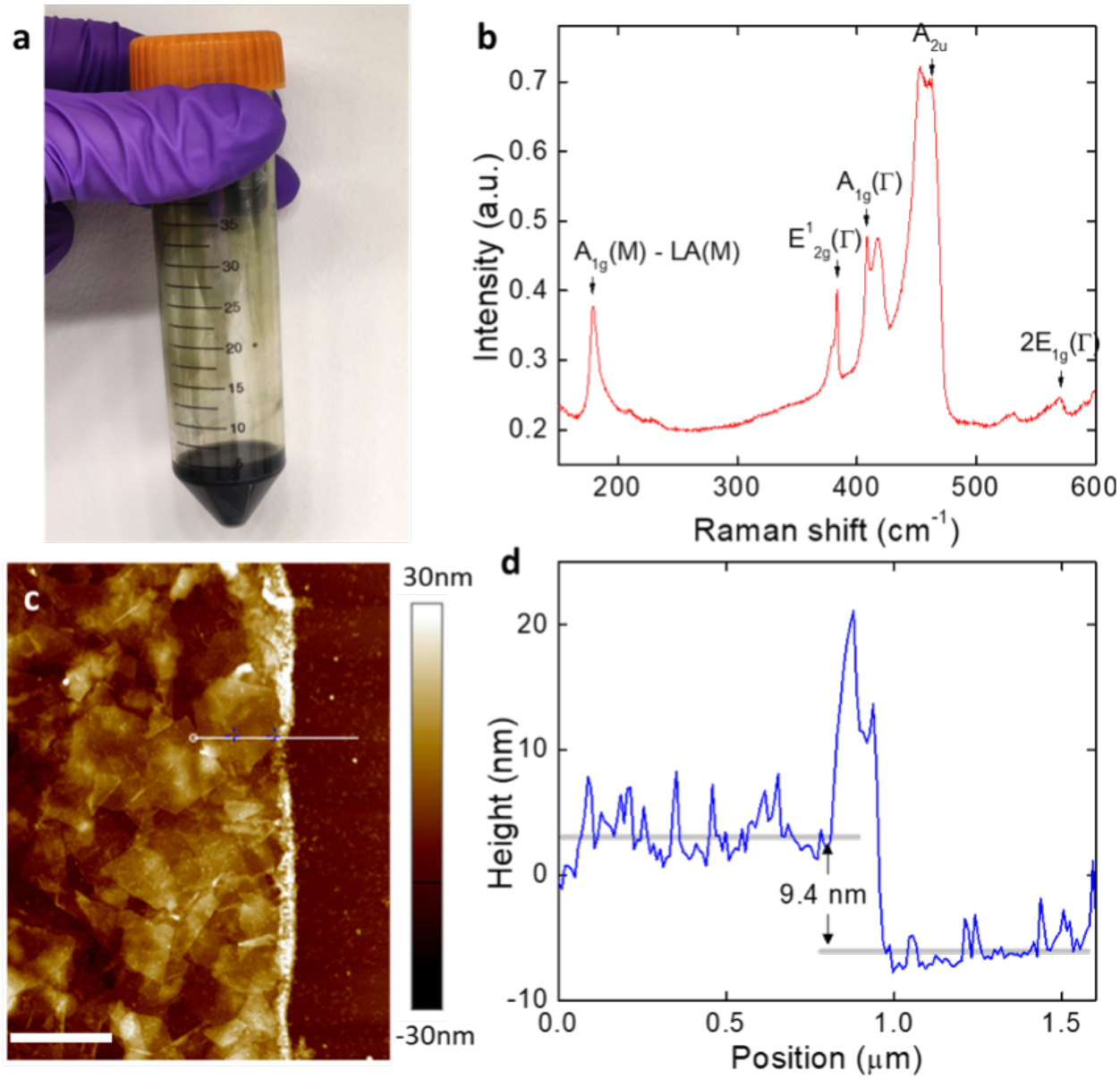

Figure 3.5: Additional data for solution processed MoS_2. a. The as-fabricated MoS_2 ink with nanosheets dispersed in IPA. b. The Raman spectra of the VDWTF, showing fingerprint peaks of MoS_2. c. The AFM measurement on the VDWTF. Scale bar: 1 um. d. The height profile along the thin white cutline in c, with a thickness around 9.4 nm.

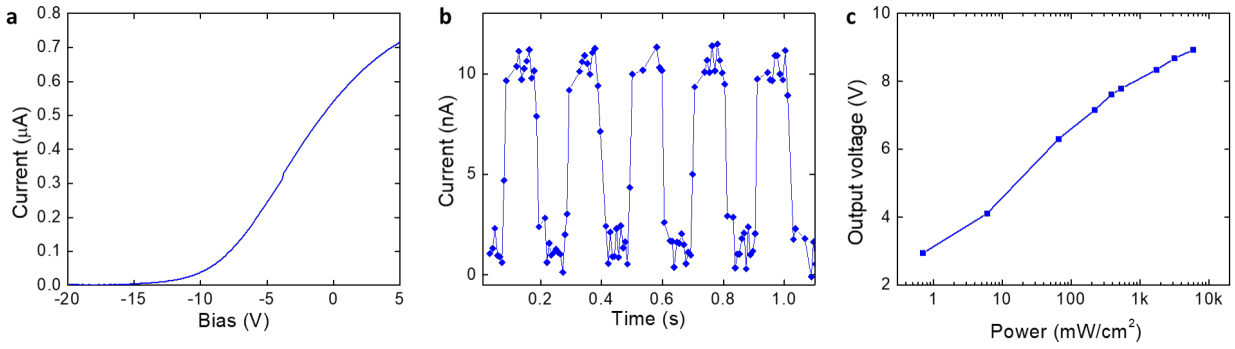

Figure 3.6: Additional TPT characteriaztion. a. The transfer curve of a VDWTF field effect transistor fabricated on silicon substrate. The device is fabricated with identical process to the TPT, except for a lower annealing temperature at 350 . A silicon body gate modulates the channel current through a 300-nm-thick SiO2 layer. The source-drain bias is 1 V. The slope leads to a derived transistor mobility of 6.1 $cm^2/(Vs)$. The value is consistent in order of magnitude with previous reported values of around 10 $cm^2/(Vs)$ [32]. b. Photoresponse from a time sweep at 5-Hz chopping frequency. The observed rise and fall times are slower than the actual response time due to the lower sampling rate and the slow speed of the chopper edges as they cut through the laser beam diameter. The measurement conditions are identical to Figure 3.2e. c. Output voltage change under different illumination powers derived from the single pixel TPT photoresponse in Figure 3.2d. We assumed a perfectly matched LC resistivity of 1 G. Both the actual LC cells and the actual TPTs integrated with the LC cells are more resistive than this wired-out single device.

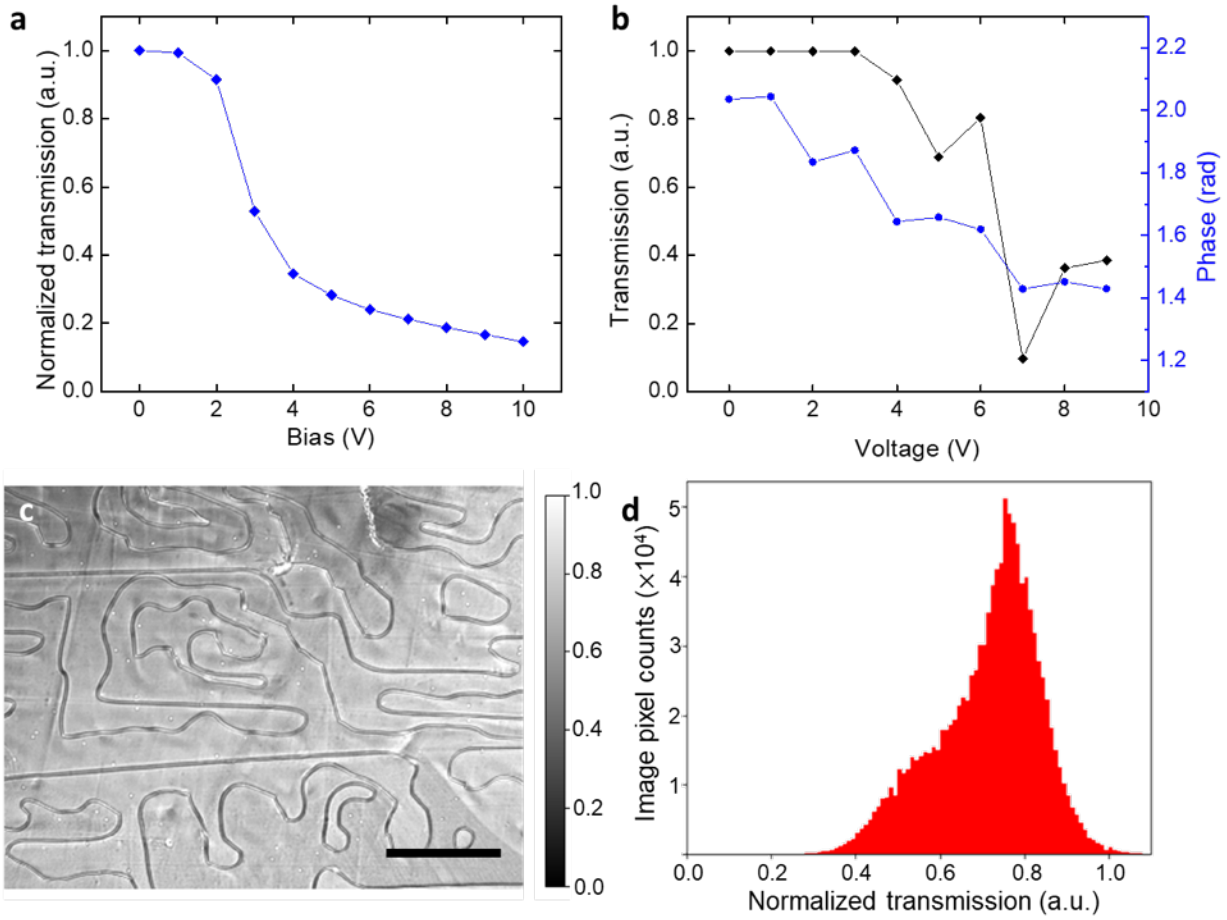

Figure 3.7: LC modulation properties. a. Measured transmission power modulation of weak thermal lamp light with pure LC. The transmission is normalized by its value at 0 V. b. Extracted transmission power and phase modulation under weak light illumination. Data from a TPT-LC device different from the main device reported in the main paper. The device also shows a lower threshold voltage due to variations in TPT resistivity as a result of process variation. c. Normalized transmission of a pure LC sample under weak thermal lamp illumination at $V_{dd} = 2.5$ V. Scale bar: 0.5 mm. d. The transmission histogram of all the image pixels in c.

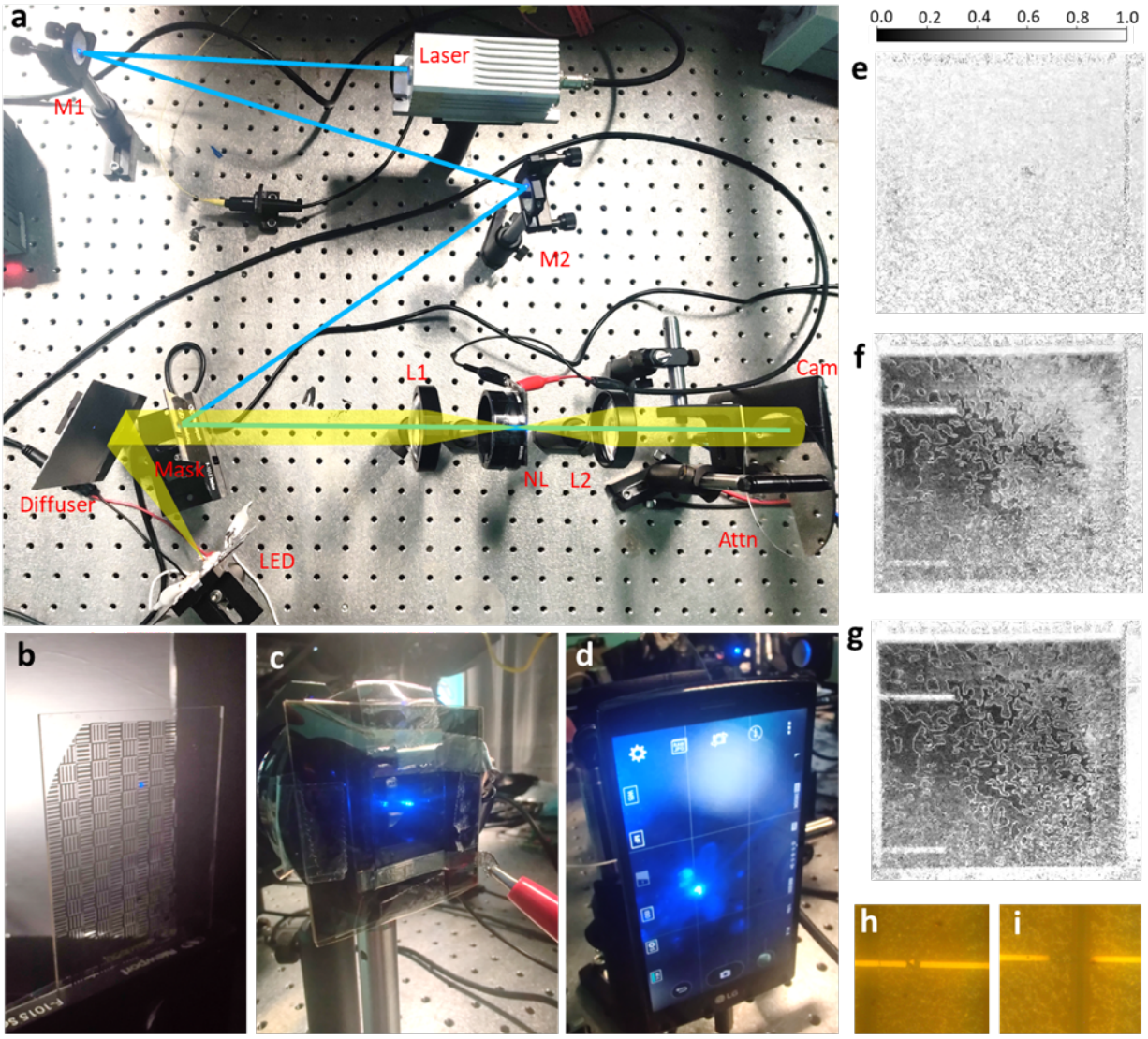

Figure 3.8: Device integration to optical systems for uniformity and glare reduction test. a. The optical setup for the test. The optical path of white light is highlighted in yellow, and the 473-nm laser path is highlighted in blue. The LED produces up to 1-W illumination that is diffusely reflected by the unpolished aluminum foil as the diffuser. The reflected light transmits through a patterned gold mask at the thickness of 100 nm as the object. Then the pattern is imaged by the lens L1 to the image plane that overlaps with the nonlinear layer NL. Lastly, the light passes through L2, which works as a magnifying glass to facilitate better

capture of the image at the smartphone camera. The laser beam is reflected by mirrors M1 and M2 to the metal mask surface. We tune the M1, M2, and mask angles to collimate the laser beam with the white light path. Since the collimated laser beam is a reflection of an intense parallel beam on the metal surface, it is a good simulation of sun glares regularly seen on glasses and cars on the road. b. A zoomed-in look at the metal mask. We remove the mask during uniformity measurements, so a relatively uniform white background is directly projected on the NL layer for transmission measurements. c. The packaged optoelectronic neuron array sandwiched by two orthogonal polarizers. It is connected to the voltage supply with the wires and mounted on an iris, which helps align the center of the device region to the optical path. d. The LG G4 smartphone used to capture the image. The image capture is set on the manual mode unless otherwise specified, with the following parameters: camera model: LGLS991, resolution = 72 dpi, bit depth = 24, color representation = sRGB, f/1.8, exposure time = 125 ms, manually set focal length = 4 mm, ISO-800, and digital zoom = 4.6. e-g. Normalized transmission at V_{dd} = 10 V (e), 16 V (f), and 22 V (g). h and i: microscope image of the broken metal wires corresponding to the upper (h) and lower (i) malfunctioning lines in g.

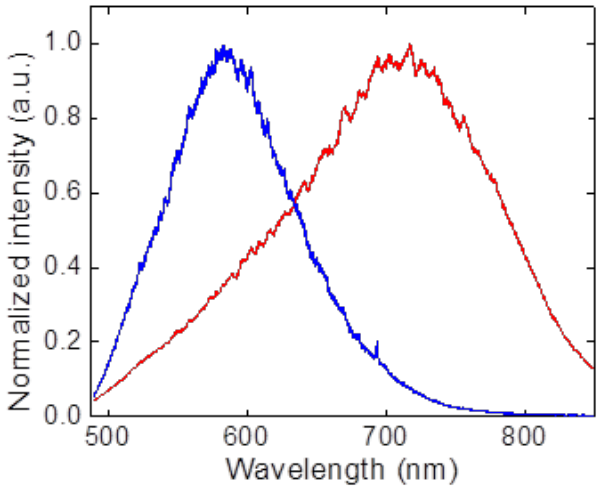

Figure 3.9: Spectra of broadband incoherent light sources. Blue: the LED spectrum, with a center wavelength of 582nm. Red: the thermal lamp spectrum at the power level applied during the measurement, with the center wavelength at 713 nm.

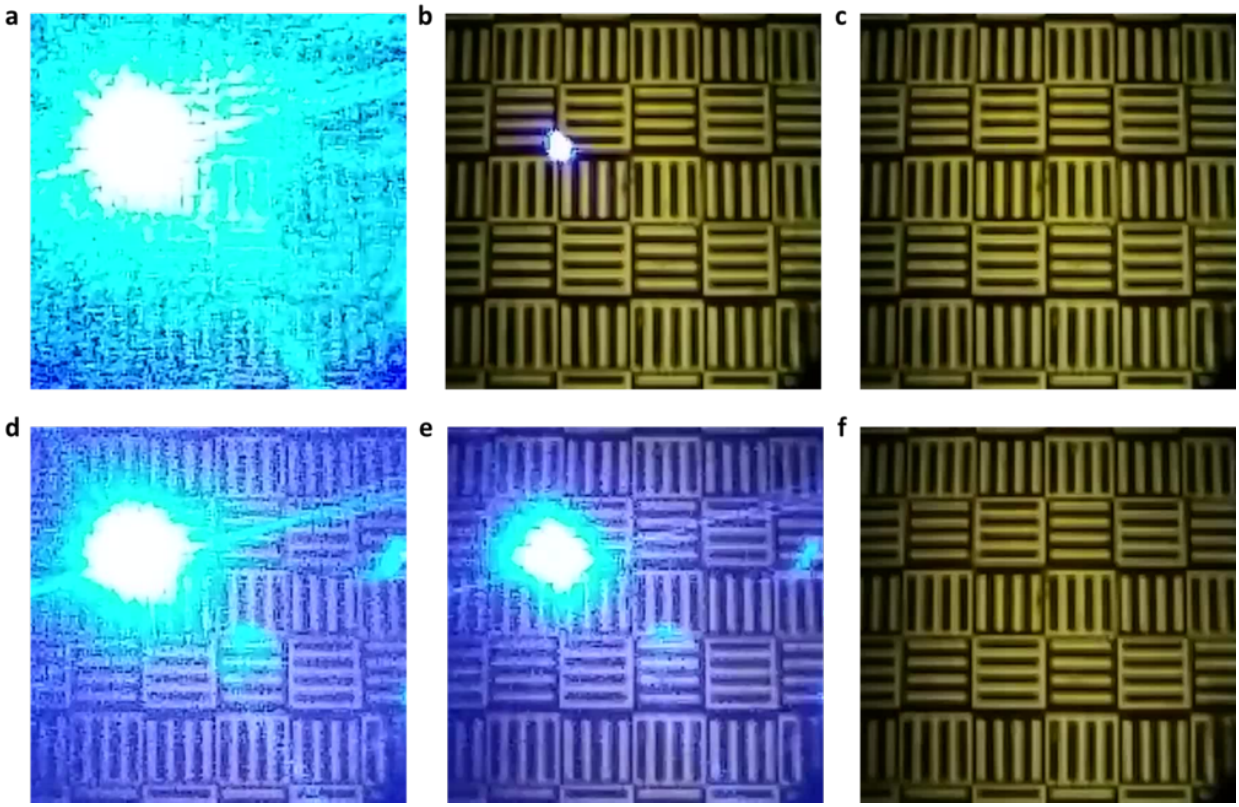

Figure 3.10: Time-resolved glare reduction observations. a-c, three continuous frames of Supplementary Video 1 at $V_{dd} = 0$ V, captured with fixed exposure. d-f, three continuous frames captured at $V_{dd} = 16$ V. No dark spot was observed at the glare spot in f, suggesting that the nonlinear neurons operate faster than the frame rate (60 Hz).

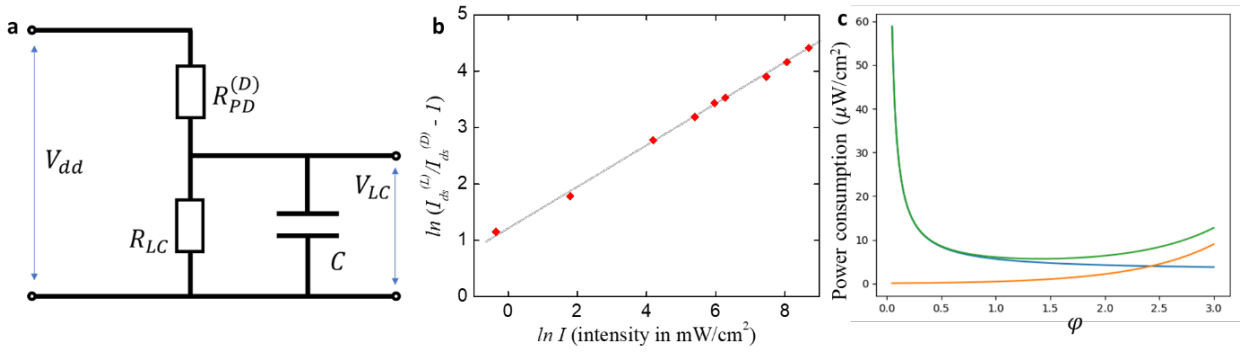

Figure 3.11: Modeling and optimization of the optoelectronic neuron. a. The equivalent circuit for frequency response modeling. b. Fitting of the channel at different incidental intensities for modeling the resistivity change. c. Estimation of power consumption per unit area at different values. Blue: electrical power consumption; orange: photon loss; green: total power consumption.

References

[1] Laj Cutrona, E Leith, C Palermo, and L Porcello. Optical data processing and filtering systems. *IRE Transactions on Information Theory*, 6(3):386–400, 1960.

[2] Pierre Ambs. Optical computing: A 60-year adventure. *Advances in Optical Technologies*, 2010:372652, May 2010.

[3] Yichen Shen, Nicholas C. Harris, Scott Skirlo, Mihika Prabhu, Tom Baehr-Jones, Michael Hochberg, Xin Sun, Shijie Zhao, Hugo Larochelle, Dirk Englund, and Marin Soljačić. Deep learning with coherent nanophotonic circuits. *Nature Photonics*, 11(7):441–446, jun 2017.

[4] Xing Lin, Yair Rivenson, Nezih T Yardimci, Muhammed Veli, Yi Luo, Mona Jarrahi, and Aydogan Ozcan. All-optical machine learning using diffractive deep neural networks. *Science*, 361(6406):1004–1008, July 2018.

[5] David J. Brady. *Optical imaging and spectroscopy.* John Wiley and Sons, Hoboken, 2009.

[6] Ravindra A Athale Joseph N Mait, Gary W Euliss. Deep learning with coherent nanophotonic circuits. *Advances in Optics and Photonics*, 10(2):409–483, jun 2018.

[7] Tao Yan, Jiamin Wu, Tiankuang Zhou, Hao Xie, Feng Xu, Jingtao Fan, Lu Fang, Xing Lin, and Qionghai Dai. Fourier-space diffractive deep neural network. *Phys Rev Lett*, 123(2):023901, July 2019.

[8] Ying Zuo, Bohan Li, Yujun Zhao, Yue Jiang, You-Chiuan Chen, Peng Chen, Gyu-Boong Jo, Junwei Liu, and Shengwang Du. All-optical neural network with nonlinear activation functions. *Optica*, 6(9):1132–1137, Sep 2019.

[9] Mario Miscuglio, Armin Mehrabian, Zibo Hu, Shaimaa I Azzam, Jonathan George, Alexander V Kildishev, Matthew Pelton, and Volker J Sorger. All-optical nonlinear

activation function for photonic neural networks. *Optical Materials Express*, 8(12):3851–3863, 2018.

[10] Aashu Jha, Chaoran Huang, and Paul R. Prucnal. Reconfigurable all-optical nonlinear activation functions for neuromorphic photonics. *Opt. Lett.*, 45(17):4819–4822, Sep 2020.

[11] Thorsten S Rasmussen, Yi Yu, and Jesper Mork. All-optical non-linear activation function for neuromorphic photonic computing using semiconductor fano lasers. *Opt Lett*, 45(14):3844–3847, July 2020.

[12] Guangyuan Zhao, Cheng Zheng, Cuifang Kuang, Renjie Zhou, Mohammad M. Kabir, Kimani C. Toussaint, Wensheng Wang, Liang Xu, Haifeng Li, Peng Xiu, and Xu Liu. Nonlinear focal modulation microscopy. *Phys. Rev. Lett.*, 120:193901, May 2018.

[13] Guangyuan Zhao, Mohammad M. Kabir, Kimani C. Toussaint, Cuifang Kuang, Cheng Zheng, Zhongzhi Yu, and Xu Liu. Saturated absorption competition microscopy. *Optica*, 4(6):633, June 2017.

[14] D. Stoppa, A. Simoni, L. Gonzo, M. Gottardi, and G.-F. Dalla Betta. Novel cmos image sensor with a 132-db dynamic range. *IEEE Journal of Solid-State Circuits*, 37(12):1846–1852, 2002.

[15] Monica Vatteroni, Daniele Covi, and Alvise Sartori. A linear-logarithmic cmos pixel for high dynamic range behavior with fixed-pattern-noise correction and tunable responsivity. *2008 IEEE Sensors*, pages 930–933, 2008.

[16] C Aparajit, Kamalesh Jana, Amit D Lad, Yash M Ved, Arnaud Couairon, and G Ravindra Kumar. Efficient second-harmonic generation of a high-energy, femtosecond laser pulse in a lithium triborate crystal. *Opt Lett*, 46(15):3540–3543, August 2021.

[17] Elissa Klopfer, Mark Lawrence, David R Barton, 3rd, Jefferson Dixon, and Jennifer A Dionne. Dynamic focusing with High-Quality-Factor metalenses. *Nano Lett*, 20(7):5127–5132, June 2020.

[18] Xingqiao Chen. Optical nonlinearity and non-reciprocal transmission of graphene integrated metasurface. *Carbon*, v. 173:pp. 126–134–2021 v.173, 0000.

[19] Shuzo Hirata, Kenro Totani, Takashi Yamashita, Chihaya Adachi, and Martin Vacha. Large reverse saturable absorption under weak continuous incoherent light. *Nat Mater*, 13(10):938–946, September 2014.

[20] Yoichi Kobayashi and Jiro Abe. Recent advances in low-power-threshold nonlinear photochromic materials. *Chem. Soc. Rev.*, 51:2397–2415, 2022.

[21] Stephen Ducharme and Jack Feinberg. Altering the photorefractive properties of batio 3 by reduction and oxidation at 650 c. *JOSA B*, 3(2):283–292, 1986.

[22] Liyun Xue, Hongde Liu, Dahuai Zheng, Shahzad Saeed, Xuying Wang, Tian Tian, Ling Zhu, Yongfa Kong, Shiguo Liu, Shaolin Chen, et al. The photorefractive response of zn and mo codoped linbo3 in the visible region. *Crystals*, 9(5):228, 2019.

[23] Koji Usui, Kohsuke Matsumoto, Erika Katayama, Norihisa Akamatsu, and Atsushi Shishido. A deformable low-threshold optical limiter with oligothiophene-doped liquid crystals. *ACS Applied Materials & Interfaces*, 13(19):23049–23056, 2021.

[24] A Partovi, AM Glass, DH Olson, GJ Zydzik, HM O'bryan, TH Chiu, and WH Knox. Cr-doped gaas/algaas semi-insulating multiple quantum well photorefractive devices. *Applied physics letters*, 62(5):464–466, 1993.

[25] Ergun Canoglu, Ching-Mei Yang, Elsa Garmire, Daniel Mahgerefteh, A Partovi, TH Chiu, and GJ Zydzik. Carrier transport in a photorefractive multiple quantum well device. *Applied physics letters*, 69(3):316–318, 1996.

[26] A Dongol, J Thompson, H Schmitzer, D Tierney, and HP Wagner. Real-time contrast-enhanced holographic imaging using phase coherent photorefractive quantum wells. *Optics Express*, 23(10):12795–12807, 2015.

[27] Jong-Sik Moon, Kyujung Kim, Dong-Wook Han, Jeffrey G Winiarz, and Jin-Woo Oh. Recent progress in organic photorefractive materials. *Applied Spectroscopy Reviews*, 53(2-4):203–223, 2018.

[28] Jong-Sik Moon, Tyler E Stevens, Todd C Monson, Dale L Huber, Sung-Ho Jin, Jin-Woo Oh, and Jeffrey G Winiarz. Sub-millisecond response time in a photorefractive composite operating under cw conditions. *Scientific Reports*, 6(1):1–12, 2016.

[29] IC Khoo, MV Wood, Min-Yi Shih, and Pao H Chen. Extremely nonlinear photosensitive liquid crystals for image sensing and sensor protection. *Optics Express*, 4(11):432–442, 1999.

[30] Ihor V Kedyk, Pierre Mathey, Gregory Gadret, Olivier Bidault, Alexander A Grabar, Ivan M Stoika, and Yulian M Vysochanskii. Enhanced photorefractive properties of bi-doped sn 2 p 2 s 6. *JOSA B*, 25(2):180–186, 2008.

[31] Miao-Bin Lien, Che-Hung Liu, Il Yong Chun, Saiprasad Ravishankar, Hung Nien, Minmin Zhou, Jeffrey A Fessler, Zhaohui Zhong, and Theodore B Norris. Ranging and light field imaging with transparent photodetectors. *Nature Photonics*, 14(3):143–148, 2020.

[32] Dehui Zhang, Zhen Xu, Zhengyu Huang, Audrey Rose Gutierrez, Cameron J Blocker, Che-Hung Liu, Miao-Bin Lien, Gong Cheng, Zhe Liu, Il Yong Chun, et al. Neural network based 3d tracking with a graphene transparent focal stack imaging system. *Nature Communications*, 12(1):2413, 2021.

[33] Zhaoyang Lin, Yuan Liu, Udayabagya Halim, Mengning Ding, Yuanyue Liu, Yiliu Wang, Chuancheng Jia, Peng Chen, Xidong Duan, Chen Wang, et al. Solution-processable 2d

semiconductors for high-performance large-area electronics. *Nature*, 562(7726):254–258, 2018.

[34] Zhaoyang Lin, Yu Huang, and Xiangfeng Duan. Van der waals thin-film electronics. *Nature Electronics*, 2(9):378–388, 2019.

[35] Chao Ma, Dong Xu, Peiqi Wang, Zhaoyang Lin, Jingyuan Zhou, Chuancheng Jia, Jin Huang, Shengtao Li, Yu Huang, and Xiangfeng Duan. Two-dimensional van der waals thin film transistors as active matrix for spatially resolved pressure sensing. *Nano Research*, 14:3395–3401, 2021.

[36] Zhuocheng Yan, Dong Xu, Zhaoyang Lin, Peiqi Wang, Bocheng Cao, Huaying Ren, Frank Song, Chengzhang Wan, Laiyuan Wang, Jingxuan Zhou, et al. Highly stretchable van der waals thin films for adaptable and breathable electronic membranes. *Science*, 375(6583):852–859, 2022.

[37] Miri Gelbaor Kirzhner, Matvey Klebanov, Victor Lyubin, Neil Collings, and I Abdulhalim. Liquid crystal high-resolution optically addressed spatial light modulator using a nanodimensional chalcogenide photosensor. *Optics letters*, 39(7):2048–2051, 2014.

[38] Vladimir V Semenov, Xavier Porte, Ibrahim Abdulhalim, Laurent Larger, and Daniel Brunner. Two-color optically addressed spatial light modulator as a generic spatiotemporal system. *Chaos: An Interdisciplinary Journal of Nonlinear Science*, 31(12):121104, 2021.

[39] Qing Hua Wang, Kourosh Kalantar-Zadeh, Andras Kis, Jonathan N Coleman, and Michael S Strano. Electronics and optoelectronics of two-dimensional transition metal dichalcogenides. *Nature nanotechnology*, 7(11):699–712, 2012.

[40] Oana Stamatoiu, Javad Mirzaei, Xiang Feng, and Torsten Hegmann. Nanoparticles in liquid crystals and liquid crystalline nanoparticles. *Liquid crystals: materials design and self-assembly*, pages 331–393, 2012.

[41] Jun-Wei Chen, Yu-Yi Kuo, Chao-Ran Wang, and Chih-Yu Chao. The formation of supramolecular liquid-crystal gels for enhancing the electro-optical properties of twisted nematic liquid crystals. *Organic Electronics*, 27:24–28, 2015.

[42] Martin Schadt. Liquid crystal materials and liquid crystal displays. *Annual review of materials science*, 27(1):305–379, 1997.

[43] Martin Schadt. Liquid crystals in information technology. *Berichte der Bunsengesellschaft für physikalische Chemie*, 97(10):1213–1236, 1993.

[44] Tomohiro Miyama, Jirakorn Thisayukta, Hiroyuki Shiraki, Yoshio Sakai, Yukihide Shiraishi, Naoki Toshima, and Shunsuke Kobayashi. Fast switching of frequency modulation twisted nematic liquid crystal display fabricated by doping nanoparticles and its mechanism. *Japanese journal of applied physics*, 43(5R):2580, 2004.

[45] Noel A Clark and Sven T Lagerwall. Submicrosecond bistable electro-optic switching in liquid crystals. *Applied Physics Letters*, 36(11):899–901, 1980.

[46] Qi Guo, Kexin Yan, Vladimir Chigrinov, Huijie Zhao, and Michael Tribelsky. Ferroelectric liquid crystals: physics and applications. *Crystals*, 9(9):470, 2019.

[47] Shampy Mansha, Parikshit Moitra, Xuewu Xu, Tobias WW Mass, Rasna Maruthiyodan Veetil, Xinan Liang, Shi-Qiang Li, Ramón Paniagua-Domínguez, and Arseniy I Kuznetsov. High resolution multispectral spatial light modulators based on tunable fabry-perot nanocavities. *Light: Science & Applications*, 11(1):141, 2022.

[48] Tyler W Hughes, Momchil Minkov, Yu Shi, and Shanhui Fan. Training of photonic neural networks through in situ backpropagation and gradient measurement. *Optica*, 5(7):864–871, 2018.

[49] Tiankuang Zhou, Lu Fang, Tao Yan, Jiamin Wu, Yipeng Li, Jingtao Fan, Huaqiang

Wu, Xing Lin, and Qionghai Dai. In situ optical backpropagation training of diffractive optical neural networks. *Photonics Research*, 8(6):940–953, 2020.

[50] Stijn Goossens, Gabriele Navickaite, Carles Monasterio, Shuchi Gupta, Juan José Piqueras, Raúl Pérez, Gregory Burwell, Ivan Nikitskiy, Tania Lasanta, Teresa Galán, et al. Broadband image sensor array based on graphene–cmos integration. *Nature Photonics*, 11(6):366–371, 2017.

[51] Wei-Ting Chen, Pei-Shiang Chen, and Chih-Yu Chao. Effect of insulating nanoparticles doping on electro-optical characteristics in nematic liquid crystal cells. *Molecular Crystals and Liquid Crystals*, 507(1):253–263, 2009.

[52] Shin-Tson Wu. Nematic liquid crystal modulator with response time less than 100 μs at room temperature. *Applied physics letters*, 57(10):986–988, 1990.

[53] Bijie Bai, Hongda Wang, Tairan Liu, Yair Rivenson, John FitzGerald, and Aydogan Ozcan. Pathological crystal imaging with single-shot computational polarized light microscopy. *Journal of biophotonics*, 13(1):e201960036, 2020.

[54] Vito Lampret, Jože Peternelj, and Aleš Krainer. Luminous flux and luminous efficacy of black-body radiation: an analytical approximation. *Solar Energy*, 73(5):319–326, 2002.

[55] Peter R Michael, Danvers E Johnston, and Wilfrido Moreno. A conversion guide: Solar irradiance and lux illuminance. *Journal of Measurements in Engineering*, 8(4):153–166, 2020.

CHAPTER 4

Highly stretchable van der Waals thin films for adaptable and breathable electronic membranes

4.1 Introduction

The integration of electronic systems with irregular, soft objects is of increasing importance for many emerging technologies, including electronics for the Internet of Things and bioelectronics for monitoring dynamic living organisms and for diagnosing and treating human diseases in the context of personalized medicine and telehealth [1]. A robust bioelectronic system requires intimate interaction with biological structures to perform specific operations,such as biological signal recording [2–4], amplification [5–7], and extraction [8], as well as delivering electrical [9, 10]) or chemical stimulation [11]. Thus, the implementation of bioelectronics hinges on a number of unusual material and device characteristics, including electronic performance; mechanical flexibility, stretchability, or malleability to ensure conformal and adaptable interfaces with dynamically evolving microscopic surface topographies; and permeability or breathability for gas and/or nutrient exchange between living organisms and their surroundings to lessen perturbation of natural bio-functions.

Conventional hard electronic materials exhibit an intrinsic mismatch with soft biological tissues in terms of electrical conductivity, mechanical response, permeability, and environmental adaptability. Hard inorganic semiconductors can be made flexible in an ultra thin membrane format but are barely stretchable and cannot form a conformal interface with ir-

regular geometries with nonzero Gaussian curvatures owing to their fundamental topological limitations [12]. The development of specifically designed deformation-tolerant structures, such as wrinkled [13], buckled [14], waved [15], or serpentine structures [16–18], bring macroscopic stretchability but not microscopic conformability, because of the intrinsic microscopic structural undulation. Organic or composite semiconductor thin films can be made stretchable or conformal [19] but usually exhibit insufficient electronic performance [12, 20] or limited stability in a typical wet biological environment.

Additionally,traditional inorganic membranes or organic thin films typically exhibit limited mechanical robustness in the ultra thin freestanding format and require a polymer [e.g., polydimethylsiloxane (PDMS) and polyimide (PI)] substrate support to retain structural integrity [12]) and specific porous architecture design to achieve breathability [21]. The polymer substrate is typically much thicker ($\gg$1 mm) than a cell membrane ($\sim$ 10 nm), with a large bending stiffness [22] and poor conformability and adaptability to the dynamically evolving biological structures [23]. Inspired by van der Waals (VDW) interactions in biological assemblies,we exploited these interactions to assemble two-dimensional(2D) nanosheets [24–27] into freestanding VDW thin films (VDWTFs) with an excellent mechanical match to soft biological tissues that can directly adapt to and merge with living organisms with ultra conformal and breathable membrane–tissue interfaces. The VDWTFs feature bond-free VDW interfaces between the staggered 2D nanosheets, opening sliding and rotation degrees of freedom between neighboring nanosheets to endow unusual mechanical flexibility, stretchability, and malleability. The staggered VDWTFs also feature a percolating network of channelizes for permeability or breathability.

4.2 Topological and mechanical limitations of a conformal interface

Although the flexibility of intrinsically stiff materials (e.g., a silicon wafer or hard cardboard) can be increased in the ultra thin membrane format (e.g., a silicon membrane or paper) [28], stretchability is fundamentally limited by the covalent chemical bonds and barely changes with reduced thickness [29]. Owing to intrinsic topological limitations, it is impossible to use such flexible yet unstretchable membranes to make a confomal interface with local topographies with nonzero Gaussian curvatures (e.g., wrapping a piece of paper around a pen; Figure 4.1A) [30]. To achieve a conformal interface with irregular geometries, stretchability is essential to allow necessary deformation to adapt to the local surface topographies. Specific polymeric materials with intermolecular slippages between polymer chains can be made stretchable [31, 32] and adaptable to local topographies under sufficient tensile stress(e.g., wrapping parafilm around a pen; Figure 4.1B) [29].

To achieve a conformal interface with a stretchable membrane, external pressure is needed to induce sufficient deformation to match the local surface topography, which results in a contact pressure that can cause tissue deformation or damage (e.g., tightly wrapping parafilm around a fingertip). A 3D geometric model is constructed to visualize the conformal adapting process of a stretchable membrane on spherical topographies and to explore the evolution of the local deformation with the contact pressure (Figure 4.1C). With increasing load, the membrane gradually adapts to the spherical indentations, with the membrane grid stretched and expanded to accommodate the local strain and deformation during the conformal adapting process.

We use a simplified spherical indentation model to evaluate the maximum contact pressure needed for forming a conformal interface with a surface topography of a given curvature.

The indentation strain, ϵ, is given by

$$\varepsilon = k\frac{r_{\text{contact}}}{r_{\text{curve}}} \tag{4.1}$$

where r_{contact} and r_{curve} are the contact radius and the topography radius, respectively (Figure 4.1D), and k is a constant associated with indentation strain [33]. Overall, the contact radius and indentation strain increase with increasing load until a conformal interface between the membrane and the hemisphere is achieved. The maximum contact pressure needed for achieving a conformal interface is determined by the Young's modulus and the membrane thickness following the relationship:

$$\left[\frac{\pi^2}{4}P_0^2\left(\frac{1-\upsilon_1^2}{E_1}+\frac{1-\upsilon_2^2}{E_2}\right)^2\right]^{1/3}+\frac{\pi^2}{8}P_0\left(\frac{1-\upsilon_1^2}{E_1}\right)\frac{r_{curve}^3}{t^3}=1 \tag{4.2}$$

where P0 is the maximum contact pressure; E1 and v1 are the Young's modulus and Poisson's ratio of the membrane, respectively; t is the membrane thickness; and E2 and v2 are the Young's modulus and Poisson's ratio of the sphere, respectively [34, 35]. The E/(1 − v2) is regarded as the plane-strain modulus, which is 130 kPa for human skin [36], 4 MPa for PDMS [37], and 2.8 GPa for polyimide [22]. The difference in plane-strain modulus illustrates the large mechanical mismatch between human skin and the soft polymeric elastomer or typical plastics.

Using Eqs. 1 and 2, we can calculate the maximum film thickness allowed to achieve a conformal interface with a topography of a given rcurve under a certain contact pressure for materials with a different plane-strain modulus (Figure 4.1E). For example, to achieve a conformal interface with a skin topography of rcurve $\sim$ 5 µm under a maximum contact pressure P0 of 1 kPa (the gentlest touch that a human can feel is 1 kPa) [38], the maximum

allowed thickness is 0.3 μm for PDMS and 39 nm for polyimide. Similarly, we can also calculate the maximum contact pressure needed to form a conformal interface with a given rcurve of 5 μm for materials with a different plane-strain modulus and thickness (Figure 4.1F).

These analyses highlight that the contact pressure needed to achieve a conformal interface is proportional to the Young's modulus and thickness of the membrane and inversely proportional to the curvature of the radius of the surface topography. Although, in principle, the contact pressure on biological tissue can be minimized by reducing membrane thickness, the thickness cannot be reduced indefinitely for most polymeric materials owing to the limitation of the characteristic size of individual polymer chains and a precipitous decrease in mechanical properties below a critical thickness (e.g., 25 nm) [23]. Conducting polymers that are suitable for electronic applications usually show worse mechanical properties owing to their specific structural properties, such as chain length, regioregularity, and degree of polymerization.

4.3 Adaptable and breathable VDWTFs

In our design of VDWTFs (Figure 4.1G), the dangling bond–free nanosheets are staggered butted up against each other to establish broad-area plane-to-plane VDW contacts with minimum interfacial trapping states to ensure excellent charge transport across the intersheet grain boundaries.With the bond-free VDW interactions between the nanosheets, the VDWTFs offer a natural mechanical match to soft biological assemblies typically characterized by VDW interactions. When deformed, the bonding-free VDW interfaces allow nanosheets to slide or rotate against each other to accommodate the local tension or compression without breaking the broad-area VDW interfaces and conductive pathways (movie S1), which is essential for achieving unusual stretchability and structural stability in the ultra thin

freestanding format. The mechanical deformation of VDWTFs is readily transformed into intersheet sliding or rotation to accommodate local strains and deformations and overcome topological limitations, thus endowing exceptional malleability and adaptability to irregular and dynamically changing surface topographies. Lastly, the VDWTFs feature a percolating network ofchannelizes (dictated by nanosheet thickness: $\sim$ 3 nm) winding around the staggered nanosheets for gas and/or nutrient permeation, which is critical for the breathability of bioelectronics (movie S2).

This combination of electronic and mechanical properties originates from the VDW interactions among the staggered 2D nanosheets and is difficult to achieve in typical chemical vapor deposition–grown thin films (CVDTFs) (Figure 4.1H). The electrical and mechanical properties of CVDTFs—with their typical polycrystalline structure consisting of laterally stitched domains—are strongly influenced by the grain size, grain orientation, shape, and density of grain boundary defects. The stiff and strong covalent bonding within the grains and disordered bonds at the grain boundaries of the CVDTFs (marked with red arrows in Figure 4.1H) can result in the formation of cracks and ruptures that propagate along the grain boundaries when they are deformed, thereby causing mechanical fragmentation and electronic disintegration under minimal strain (movie S1).

4.4 Structural and mechanical properties of VDWTFs

Molybdenum disulfide (MoS_2) nanosheet ink was prepared using an intercalation-exfoliation process and assembled into VDWTFs using a spin coating process (see supplementary materials). Scanning electron microscopy (SEM) and transmission electron microscopy (TEM) studies show a staggered nanosheet thin film (Figure 4.2,A and B)with an overall film thickness of $\sim$ 10 nm (Figure 4.6A). The MoS_2 nanosheets, with a thickness of $\sim$ 3 nm and

lateral dimensions ranging from less than one to several micrometers, are staggered butted up against each other to form broad-area plane-to-plane VDW Interfaces with an average of ~ 3 to 4 nanosheets staggered in a crisscross manner in the vertical direction. The broad-area bond-free VDW interfaces allow adjacent nanosheets to slide or rotate against each other to accommodate local structural perturbation and reduce the strain-induced cracks and fractures, thus ensuring structural integrity even in the free standing format. For example, the continuous freestanding VDWTFs can be readily floated on water (Figure 4.2C and movie S3), completely folded repeatedly without tearing (movie S4), and suspended over open holes without rupturing (Figure 4.2M). In comparison, the free-standing polycrystalline CVDTFs (Figure 4.6B) easily fragment on water (Figure 4.2D and movie S3) and are too fragile to suspend over open holes (Figure 4.7).

The stress–strain curve of the freestanding VDWTFs shows a well-behaved linear relationship up to a tensile strain of 43% (Figure 4.2E), with a Young's modulus (~ 47.3 MPa) about three orders of magnitude smaller than that of bulk MoS_2 (~ 200 GPa). The greatly reduced modulus indicates that the film deformation is transformed into interlayer sliding or rotation among nanosheets rather than an intrinsic lattice expansion (Figure 4.2F). Beyond the linear regime, the stress shows little increase with further increasing of the tensile strain to $\sim 62\%$, indicating that interlayer sliding or rotation gradually reaches the limit and begins to initiate local rupture, which further aggravates at higher tensile strain and leads to complete rupture at a tensile strain of $> 120\%$.

We compared the electronic properties of the VDWTFs and CVDTFs as a function of the applied strain (Figure 4.2G). Because CVDTFs cannot maintain macroscopic structural integrity in the freestanding form, the measurement was done on films supported on PDMS substrates to ensure a robust comparison. For CVDTFs, the relative resistance exhibits a gradual linear increase at a tensile strain of $< 2.5\%$, followed by a steep increase beyond

2.5%, indicating that the CVDTFs start to macroscopically break apart. In contrast, the VDWTFs do not exhibit a rapid resistance increase until a tensile strain of $> 55\%$, with a stable recoverable resistance under repeated strain cycles(Figure 4.8). When the tensile strain is$> 55\%$, the resistance increases sharply, indicating the formation of microscopic cracks and substantially reduced conductive pathways.

4.5 Adaptability, wettability, and permeability of VDWTFs

We evaluated the adaptability and conformability of the VDWTFs to microscopic surface topographies. SEM studies revealed that the VDWTFs exhibit highly conformal interfaces with not only the microsphere (4.3-µm-diameter) arrays (Figure 4.2H)but also the isolated single microspheres, two- or three-microsphere clusters (Figure 4.2I), conformally wrapping around the microspheres without tearing. By comparison, the CVDTFs on the same surface topography are much less conformal and show abundant microcracks (Figure 4.2, J and K), particularly at the high strain or stress concentration region (e.g., the foot of the microspheres or the space between two adjacent microspheres).

Surface wettability is essential for ensuring proper adhesion between electronic membranes and living organisms (Figure 4.2L). With abundant edge structures in individual nano-sheet building blocks, the VDWTFs exhibit better wettability (with a water contact angle of 40.2°) than CVDTFs (water contact angle of 76.3°), which is desirable for intimately interfacing with wet biological tissues.

Lastly, membrane permeability or breathability is required for gas or nutrient exchange with the environment in bioelectronic applications. Water vapor transmission studies (see supplementary materials) reveal water vapor transmission rates of 34 and 26 mg $cm^{-2} \cdot hour^{-1}$

for the 10-nm-thick and 30-nm-thick freestanding VDWTFs, respectively, suspended over an open hole (Figure 4.2, M and N), about six to eight times higher than the typical transepidermal water loss (TEWL) rate (4.4 mg $cm^{-2} \cdot hour^{-1}$) [39]. Such permeability of the continuous VDWTFs is attributed to the staggered nano-sheet structures, with a highly interconnected network of nanochannels (with the channel thickness dictated by the nanosheet thickness: $\sim$ 3 nm) winding around the staggered nano- sheets (movie S2).

4.6 Leaf-gate VDWTF transistors

Given their exceptional stretchability, conformability, and breathability, the VDWTFs can directly merge with living organisms to form seamless electronic-bio hybrids.Whereas previous attempts sought to augment plant function with electroactive materials or to simply use the plant as an unconventional supporting substrate, our approach was to transfer the VDWTFs onto a leaf to form a leaf-gate transistor, in which the plant leaf functions as a modulating gate and constitutes an active part of the device. We chose the Senecio mandraliscae leaf (Figure 4.3A), which contains abundant electrolyte in mesophyll, as a model system to study the leaf-gate transistors. For the leaf-gate transistor operations (Figure 4.3B), the VDWTF channel is contacted with serpentine-mesh Au electrodes (Figure 4.3C, top) to prevent breaking of the Au thin-film electrodes by local strain on the rough leaf surface, while an inserted tungsten probe establishes electrical contact to the electrolyte within the leaf to form the gate electrode. The transferred VDWTFs form a highly conformal interface with complete compliance, as confirmed by the optical microscopy (Figure 4.3D) and SEM studies (Figure 4.3E).

The function of the leaf-gate transistor relies on the ionic gating effect (in the electrolyte of the leaf gate) to modulate the electronic properties of the VDWTFs, for which the micro-

scopically conformal interface is essential for efficient gating. The leaf-gate transistor shows a typical n-channel transfer curve with an on/off ratio of $\sim$ 100 (Figure 4.3, F to H). The relatively low on/off ratio is limited by the direct leakage into the transistor channel from the leaf gate through direct resistive coupling. With a highly conformal interface and efficient gate coupling, the leaf-gate transistor can operate at a low operating voltage amenable to biological systems.

4.7 Skin-gate VDWTF transistors

VDWTFs can be transferred onto human skin with a highly conformal interface to form skingate transistors (Figure 4.9). In the skin, electrolytes help conduct electricity, regulate pH levels, and keep the body's hydration system in check. The conformal integration of VDWTFs with the skin textures (Figure 4.10, A to C) results in skin-gate transistors in which the electrolyte in human skin effectively modulates the conduction in VDWTFs (Figure 4.4, A and B). Proper skin-gate transistor function requires a conformal interface with an intimate interaction between the VDWTF channel and the epidermis, in which the epidermis can be modeled by a parallel circuit consisting of a capacitor and a resistor, and the dermis and underlying subcutaneous tissues modeled by a resistor (Figure 4.4B).

We investigated the conformability of the freestanding VDWTFs on a forearm skin replica made of Ecoflex silicone rubber and compared it with the same VDWTF supported on a 1.6-μm-thick PI substrate (Figure 4.4C). The freestanding VDWTF adapts to the skin textures and makes an excellent conformal interface without apparent cracking or tearing. In contrast, the 1.6-μm-thick PI substrate and the VDWTF with the PI substrate show much less conformal contact, with most of the fine skin textures, such as the surface wrinkles and pits, hidden (Figure 4.4C, right side). A profilometry height profile analysis shows that

surface topography of the skin replica covered with the freestanding VDWTF is essentially the same as that without the VDWTF (Figure 4.4, D and E), suggesting a fully conformal interface. In contrast, for the area covered with the VDWTF supported by the 1.6-μm-thick PI substrate (Figure 4.4, F and G), the surface topography is largely flattened, suggesting that the1.6-μm thick PI substrate is already too thick to naturally adapt to the skin textures to form microscopically conformal interfaces.

The ability of a membrane to make a conformal interface with the surface topography can be determined by bending stiffness (22). The effective bending stiffness (EI) for a multilayer membrane can be described as:

$$EI = \sum_{i=1}^{N} \frac{E_i}{1-\upsilon_i^2} h_i \left\{ \frac{1}{3}h_i^2 + \left[\left(\sum_{j=1}^{i} h_j \right) - h_{neutral} \right]^2 - h_i \left[\left(\sum_{j=1}^{i} h_j \right) - h_{neutral} \right] \right\} \quad (4.3)$$

$$h_{neutral} = \frac{\sum_{i=1}^{N} \frac{E_i}{1-\upsilon_i^2} h_i \left[\left(\sum_{j=1}^{i} h_j \right) - \frac{1}{2}h_i \right]}{\sum_{i=1}^{N} \frac{E_i}{1-\upsilon_i^2} h_i} \quad (4.4)$$

where $h_{neutral}$ denotes the neutral mechanical plane; i represents the ith layer of the film; h_i , E_i , and υ_i represent the thickness, the elastic modulus, and Poisson's ratio, respectively; and N is the number of layers [40]. Notably, with its ultra small thickness and low elastic modulus, the freestanding 10-nm-thick VDWTF exhibits a bending stiffness of 4.2×10^{-9} GPa·μm^3 , which is about eight orders of magnitude smaller than that of the1.6-μm-thick VDWTF/PI film (0.97 GPa·μm^3).

The VDWTFs transferred onto human skin show excellent natural adaptability to changing skin textures and retain conformal contact without apparent fracturing or flaking throughout stretching, squeezing, and relaxing cycles (Figure 4.4H), highlighting the highly adaptable nature of the VDWTFs to dynamically evolving biological substrates. Incontrast, the CVDTFs transferred onto human skin easily fracture and flake off when the skin is sub-

jected to similar deformation. Figure 4.4I shows the remaining area of both films on the skin replica versus the number of squeezing-and-stretching cycles. Because the freestanding CVDTFs are not strong enough for processing and transferring, they are transferred onto the skin replica with methyl methacrylate (MMA) support. After the transfer process, the CVDTFs quickly flake off once the MMA is dissolved away with acetone vapor. The remaining area instantly decreases to $\sim$ 50% of the original area and, after 100 stretching cycles, further decreases to 40% of the original area, with mostly fractured domains. The fracturing and flaking are attributed to the unstable membrane–skin interface, which is associated with their limited stretchability, conformability, and poor wettability. In contrast, the VDWTFs show superior stretchability and conformability to the dynamically changing skin replica with no apparent fracturing or flaking, retaining essentially 100% surface coverage after the repeated squeezing-and-stretching cycles.

The output and transfer curves of the skin-gate VDWTF transistor demonstrate expected transistor functions (Figure 4.4, J and K) with a low operating voltage suitable for biological systems. Furthermore, the skin-gate VDWTF transistor can maintain stable operation while undergoing various mechanical deformations (Figure 4.4L), establishing a foundation for applications in probing and amplifying electro-physiological signals.

4.8 Monitoring electrophysiological signals with skin-gate VDWTF transistors

Given that many biopotential signals show transient responses, we have evaluated the frequency response of the skin-gate transistors. The response times, τ, of the skin-gate transistors are probed by measuring the current response under a 20-µs pulse of 100-mV gate voltage (Figure 4.5A). A response time of 7 µs is achieved by fitting experimental data with

an exponential function(Figure 4.5B). Furthermore,the skin-gate transistors show a cut-off frequency (at which the transconductance drops by 3 dB from its plateau value) of $\sim$ 100 kHz (Figure 4.5C), which is sufficient for monitoring most electrophysiological signals from the human body.

We explored the skin-gate VDWTF transistors for monitoring electrocardiography (ECG). In this measurement, theVDWTF pad is placed on the left forearm and the gate electrode is adhered on the symmetrical position (right forearm) (Figure 4.5D), and each VDWTF pad works with an Ag/AgCl electrode nearby for comparison. Among the common challenges in measuring ECG with conventional Ag/AgCl electrodes are the motion artifacts due to sliding, inconsistent adhesion, and a mechanical mismatch at the electrode–skin interface induced by skin deformation, leading to a greatly reduced signal-to-noise ratio (SNR), from 44.3 dB before motion (Figure 4.5E) down to 28.5 dB during motion (Figure 4.5, F and G). With the conformal skin-gate transistors, motion artifacts are mitigated, achieving an essentially comparable SNR of 49.8 dB before human motion (Figure 4.5E and Figure 4.11) and 49.2 dB during human motion (Figure 4.5, F and G). With reduced motion artifacts, the ECG signals recorded by the skin-gate transistors (red line) show clear P, QRS, and T waves, with no abnormal deviations and relatively stable baseline during human motion(Figure 4.5, F and G).In contrast, such fine signals are less resolvable by the Ag/AgCl electrodes (Figure 4.5G).

High-fidelity, real-time electroencephalogram (EEG) recording is important for monitoring cerebral activities, studying cognitive behaviors, and developing insights into various neurological disorders. Cerebral activities can be divided into five frequency bands: delta wave (0 to 4Hz),theta wave(4 to 8 Hz), alpha wave(8 to 12 Hz), beta wave (12 to 30 Hz), and gamma wave ($>$ 30 Hz), with each frequency band associated with different mental states. To test the ability to acquire high-quality neurophysiological signals, we placed the VDWTF

transistor over the left side of the forehead (Fp1) according to the international 10-20 system of EEG electrode placement (17) and recorded voltage differences relative to a reference electrode placed over the left occipital region (O1) (Figure 4.5H). When the human subject is relaxed with eyes closed, the EEG background is usually characterized by the posteriorly dominant alpha rhythm (posterior dominant rhythm) with a prominent 8- to 12-Hz (alpha) oscillation (Figure 4.5, I and J), corresponding to brain activities such as meditation and mindfulness that can reduce stress levels. The alpha rhythm typically attenuates considerably upon eye opening, as clearly seen in the spectrogram of the EEG signal measured by the skin-gate transistor (Figure 4.5K), showing the dynamic activity of the alpha rhythm coupled with cyclic eye closing and opening.

4.9 Conclusions

Here, we report on mechanically robust freestanding VDWTFs assembled from 2D nanosheets for highly stretchable, adaptable, conformal, and breathable membrane electronics. The bond-free VDW interfaces among the nanosheets enable sliding and rotating degrees of freedom to render extraordinary mechanical flexibility, stretchability, and malleability. The staggered nanosheet architecture also features a percolation network of nano-channels for excellent permeability or breathability. The ultra thin freestanding VDWTFs are structurally robust with an excellent mechanical match to soft biological tissues, naturally adapting to microscopic topographies and directly integrating with living organisms through highly conformal interfaces, endowing living organisms with electronic functions. The VDWTFs can thus function as versatile electronic membranes that actively adapt to the environment while retaining sufficient electronic performance for sensing,signal amplification, processing, and communication.

4.10 Materials and Methods

4.10.1 Preparation of VDWTFs

The MoS_2 /isopropanol (IPA) ink solution was prepared using a molecular intercalation/exfoliation method [25, 26], which involved a two-electrode electrochemical cell with a thin piece of cleaved MoS_2 crystal (molybdenite) as the cathode, graphite rod as the anode, and tetra-heptylammonium bromide (THAB, 98% from TCI) dissolved in acetonitrile (40 ml; 5 mg ml^{-1}or higher) as the electrolyte. During the intercalation process, a negative voltage (5−10 V) was applied to the MoS_2 (cathode) for 1 hour to insert the positively charged THA+ into the crystal and result in fluffy bulk material, which was rinsed with absolute ethanol and sonicated in 40 ml 0.2 M PVP/DMF solution (PVP: molecular weight of about 40,000, Sigma-Aldrich) for 30 mins to obtain a greenish nanosheet dispersion. The dispersion was subsequently centrifuged and washed with isopropanol (IPA) twice to remove excessive PVP. The final dispersion in IPA was centrifuged at 1,000 rpm for 3 min and precipitates were discarded to remove large chunks or other impurities. The MoS_2 /IPA ink with the peak absorbance of 0.70 at around 440 nm was spin-coated three times on the oxygen plasma pre-treated SiO_2/Si substrate at a speed of 2000 rpm for 20 s to achieve $\sim$ 10-nm-thick VDWTFs. Thicker VDWTFs up to 30 nm can be obtained by increasing the number of repeated spin-coating cycles. Thermal annealing treatments (300 °C) were performed before patterning VDWTFs and defining the top-contact electrodes for the completion of the VDWTF transistor fabrication. When desired for specific applications, the annealing temperature may be varied to achieve VDWTF devices with different conductivity and gating effect. A lower annealing temperature typically leads to a higher conductivity but a smaller gating effect.

4.10.2 Transfer process of freestanding VDWTF

We prepared patterned VDWTF transistors with 50-nm-thick Au electrodes on SiO_2/Si substrates by using standard photolithography, drying etching, and high-vacuum electron-beam evaporation. Next, a 50-nm-thick MMA layer (MMA (8.5) MAA EL9, MICROCHEM) was spin-coated on top of the VDWTFs and baked at 180 °C for 2 mins to serve as the supporting layer during substrate etching. After KOH etching at 120 °C for 20−60 mins, the VDWTFs were separated from SiO_2/Si substrates and then can be released to the DI water. After acetone vapor etching for 1 minute to remove the MMA layer, the freestanding VDWTFs were obtained, which can be transferred to various substrates (e.g., plant leaves or human skins) (Figure 4.9). The electrical property studies showed that the as-prepared VDWTFs and transferred VDWTFs show a similar carrier mobility distribution (Figure 4.12), indicating there is no noticeable degradation of the electronic performance with the transfer process. We used the ImageJ software to determine the remaining area of both the VDWTFs and CVDTFs on the skin replica under cyclic stretching test.

4.10.3 Preparation of CVDTFs

The MoO_3 with a desired thickness (15 nm) was deposited on the SiO_2/Si substrate by electron- beam evaporation. The as-deposited MoO_3 was annealed at 400 °C for 20 min to form α-MoO_3. Then the MoO_3 thin film was sulfurized at 500 °C for 20 min. After sulfurization, a 20 min annealing at 900 °C in the sulfur vapor was performed to improve the crystallinity of the MoS_2. The obtained CVDTF (polycrystalline MoS_2 thin film) was approximately 10 nm thick.

4.10.4 Water vapor transmission rate test

This test procedure was based on a modified ASTM E96 standard (standard test methods for water vapor transmission of materials) [21]. Glass vials (VWR, USA), filled with 1 ml distilled water, were sealed by the VDWTFs, thread seal tape and polyimide tape with a single hole that enables VDWTF suspended on it. The sealed bottles were then placed into an environmental chamber with relative humidity 30 ± 10% at 35 °C. The experiment with an open bottle was conducted to evaluate the water evaporation rate in this chamber environment, and with a closed bottle to determine the effect of bottle itself on the measurement. The total mass of the bottles together with the samples was measured periodically. The reduced mass, corresponding to the evaporated water, was then divided by the exposed area (1 mm in diameter) to derive the water vapor transmission rate.

4.10.5 Tensile tests for the freestanding VDWTF

Tensile tests for the freestanding VDWTFs were carried out using a Mark-10 7 series testing machine. The VDWTFs supported by drilled polypropylene films (2.0×1.5 cm^2 aperture) were mounted on the tensile grips. The stress-strain measurements of the freestanding VDWTFs were performed after clipping off the polypropylene support to leave the freestanding VDWTFs alone.

4.10.6 The basic transistor test, frequency response, ECG and EEG measurement

The polyurethane adhesive tapes with serpentine-layout Au electrodes were prepared to serve as tattoo electrodes assisting the on-body measurements with VDWTF transistors. The VDWTF transistors used for gate pulse and cut-off frequency measurements have a

channel width of 110 µm and a channel length of 5 µm. A function generator (Agilent 33220A) was used to add a low amplitude (0−0.1 V) oscillation on gate, and the small signal transconductance was determined by the amplitude ratio between the drain current oscillations and the corresponding input square wave (duty ratio=1:1). The transistor characteristics were measured using Keysight B2901A. The gate pulse, ECG, and EEG signals were recorded with Agilent DSO3202A Oscilloscope, PLUX device and Arduino board using compatible software developed by our lab (1000 Hz sampling rate for ECG and EEG recording with the test time more than 2 mins). To compare the existing sensor technology (e.g., the standard Ag/AgCl-electrode) and measure the frequency response accurately, the drain current is converted to a voltage output by placing a load resistance in series. The on-body measurements were performed in compliance with all the ethical regulations under the Institutional Review Board (IRB) protocol (ID: IRB# 20-001882) at the University of California, Los Angeles. All participating subjects belonged to the University of California, Los Angeles and were provided informed consent for the participation in the study.

4.11 Supplementary Text

4.11.1 Calculation of conformal contacting process

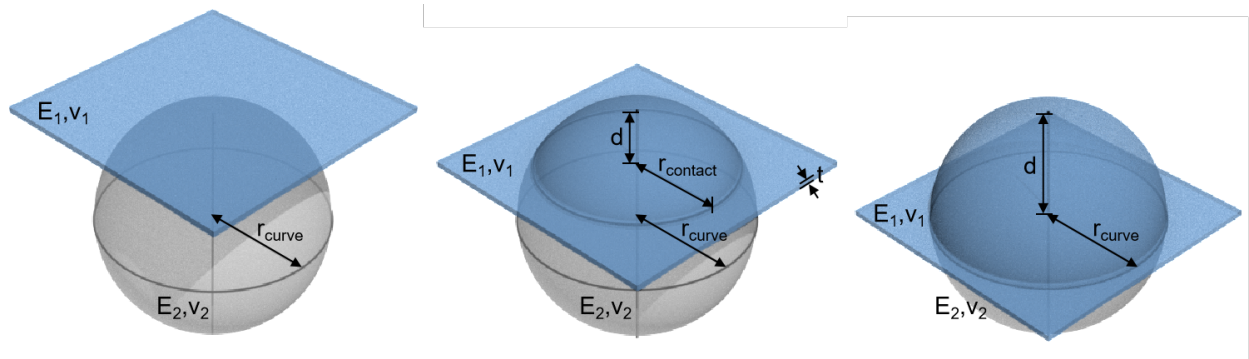

A contact mechanics model is used to demonstrate the conformal contacting process of spherical indentation, and analyze the force vs. contact radius plots in the following form [34]:

$$d = \left(\frac{9F^2}{16 r_{curve}} \left(\frac{1-\upsilon_1^2}{E_1} + \frac{1-\upsilon_2^2}{E_2} \right)^2 \right)^{\frac{1}{3}} + \frac{3a^2 \left(1-\upsilon_1^2\right) F}{4\pi E_1 t^3} \tag{4.5}$$

where F is the force, a is half of the side length of the film, r_{curve} is the sphere radius, d is the depth of indentation and t is the film thickness, E_1 , E_2 are the Young's modulus and $upsilon_1$, $upsilon_2$ are the Poisson's ratios associated with each body. The $E/(1-\upsilon^2)$ is regarded as plane-strain modulus. The maximum contact pressure P_0 in the contact mechanics model is defined as [35]:

$$P_0 = \frac{3F}{2\pi r_{contact}^2} \tag{4.6}$$

4.11.2 SNR calculation for ECG signals

To calculate the SNR, the power spectral density (PSD) is first obtained using the Welch's method in MATLAB 2019b (3). The parameters for the pwelch function are chosen to be a 1000-point Hanning window (i.e., our sampling frequency) and a 50% overlap. Considering the frequency 15 range of interest for ECG signals is typically below 100−120 Hz (Figure 4.11), the region below 100 Hz is chosen to represent our signal in the SNR calculation and the power is summed over those frequencies and normalized to be in units of dB. The noise is averaged from the region shown in black (400−500 Hz) (Figure 4.11) and this frequency range is chosen because it is obviously in the noise floor. The following formula is used to convert the ratio of the signal and noise to power in dB:

$$SNR = 10 \times \log_{10} \frac{P_{(s)}}{P_{(n)}} \tag{4.7}$$

where $P_{(s)}$ is the power of the ECG signal and $P_{(n)}$ is the power of the noise. This approach for calculating the SNR is used for the signals shown in Figure 4.5E. It should be noted that

if the noise is averaged across all frequencies greater than our signal of interest (i.e., > 100 Hz) instead of the $400-500$ Hz range, the SNR values changes negligibly.

4.11.3 SNR calculation for ECG signals under human motion

The SNRs of the signals shown in Figure 4.5F are calculated using a different approach since these signals had obvious motion artifacts that needed to be isolated and considered as noise in the SNR calculation (3). The approach to isolating the artifact is: the raw signal is filtered to remove most ECG signals while keeping the artifacts without too much attenuation. To completely reject the unwanted frequencies and obtain uniform sensitivity for the wanted frequencies, all the following filters utilized Butterworth filters. The raw signal is filtered with a 1^{st} order lowpass filter with a 3 Hz cut-off frequency, and this will be referred to as the motion artifact signal. Simultaneously, the raw signal is filtered to isolate the noise level with a 1st order bandpass filter with cut-off frequencies of 400 and 500 Hz, and this will be referred to as the noise signal. This value is chosen to match the noise range utilized in the previous SNR calculations. For only the time duration for which the motion artifact occurred, the artifact is taken from the motion artifact signal and inserted into the noise signal by the addition of the corresponding samples in time. To calculate the SNR, the root-mean-square (RMS) values of the signal (with motion artifacts and noise removed) and the rms values of the noise is divided and the following formula was utilized:

$$SNR = 20 \times \log_{10} \frac{V_{rms(s)}}{V_{rms(n)}} \tag{4.8}$$

where $V_{rms(s)}$ and $V_{rms(n)}$ are the rms values of the signal (with motion artifacts and noise removed) and noise, respectively.

4.12 Figures and Legends

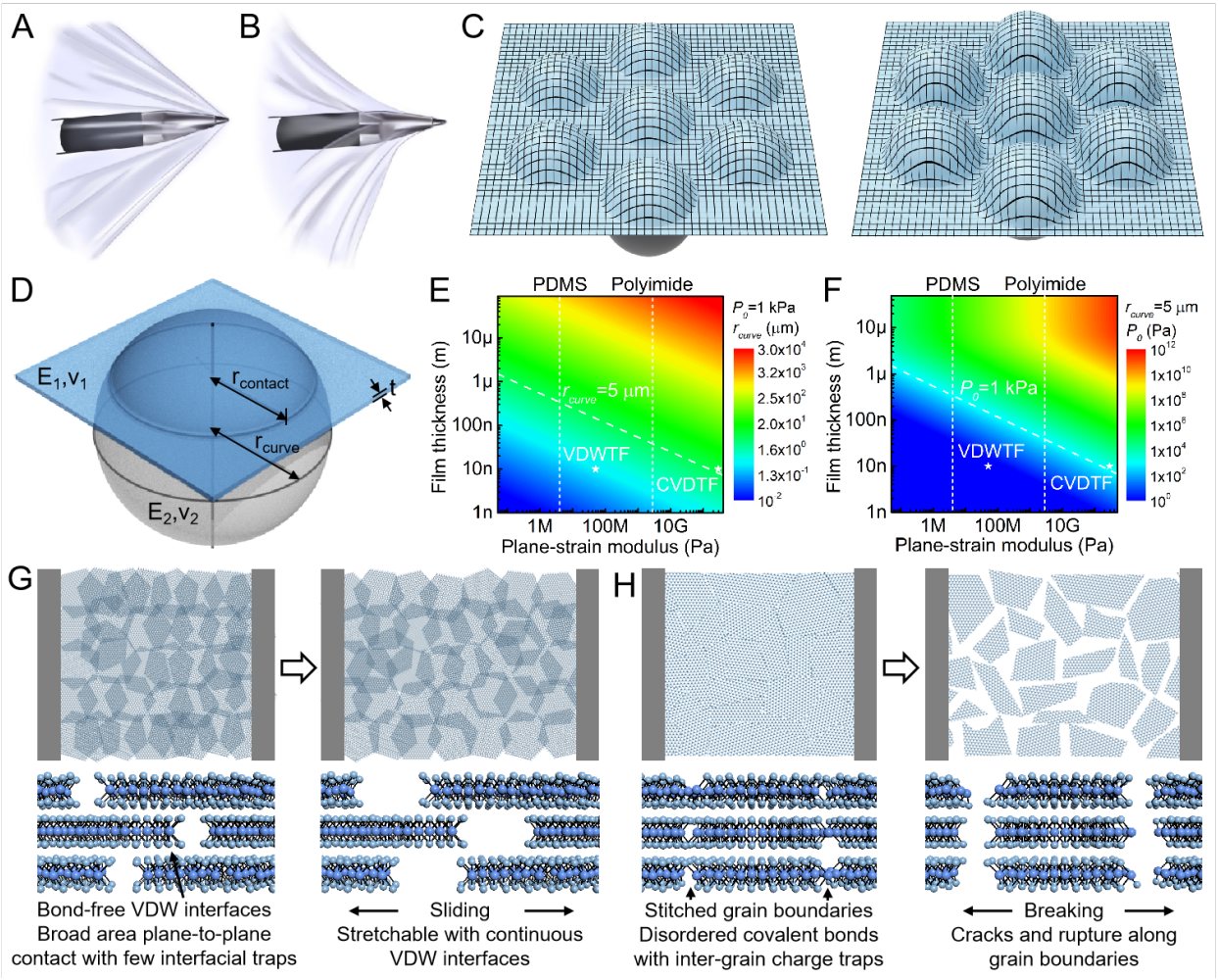

Figure 4.1: Conceptual comparison of unstretchable and stretchable membranes. (A and B) Illustrations showing the wrapping of a piece of (A) unstretchable and (B) stretchable membrane around a pen. (C) Illustrations showing stretchable membranes with grid lines gradually conforming to a curved surface topography. (D) Diagram of a spherical indentation model and relevant parameters. (E and F) Contour maps showing the relationship between plane-strain modulus, film thickness, and (E) contact radius at a contact pressure of 1 kPa or (F) maximum contact pressure for a contact radius of 5μm, highlighting that reducing thickness and plane-strain modulus favors a conformal interface. (G and H) Schematic

diagram of (G) VDWTFs and (H) CVDTFs before and after stretching.

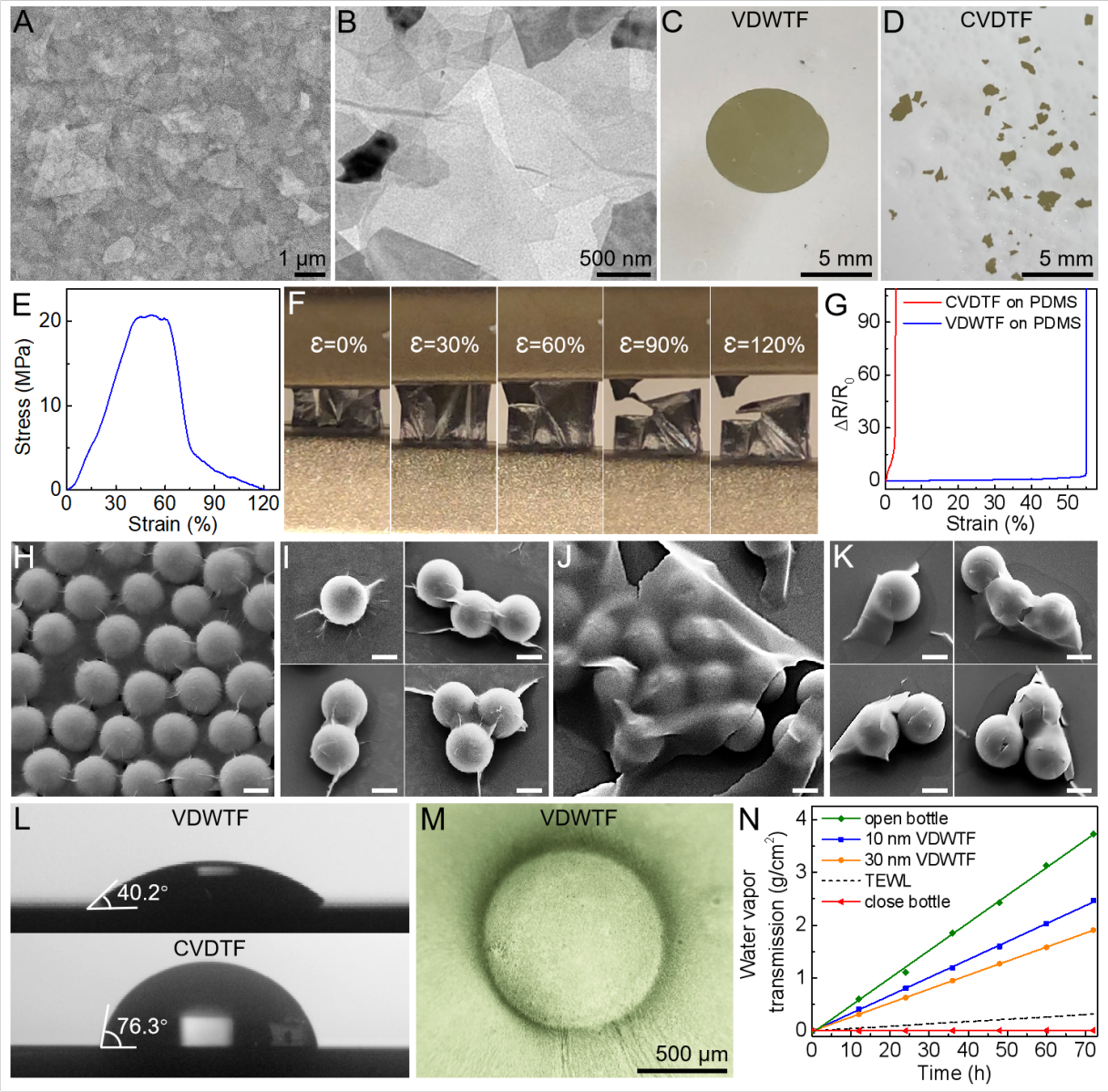

Figure 4.2: Material characteristics of VDWTFs and CVDTFs. (A) SEM and (B) TEM images showing VDWTFs assembled from staggered 2D nanosheets. (C and D) Photograph of the (C) VDWTFs and (D) CVDTFs floating on water. (E) Stress–strain curve of a freestanding VDWTF. Tensile loads cause 2D nanosheets in VDWTFs to slide or rotate against each other, resulting in unusual stretchability.(F)Photographsofthe VDWTF at dif-

ferent tensile strains. (G) Resistance–strain curve of the VDWTF and CVDTF on a PDMS substrate. (H to K) SEM images showing the contact interface between the 4.3- µm-diameter silica microspheres of different configurations with [(H) and (I)] VDWTFs or [(J) and (K)] CVDTFs. Scale bars, 2 µm. (L) Water contact angles of a VDWTF (top) and a CVDTF (bottom). (M) Optical micrographs of a VDWTF suspended over a polyimide substrate with circular holes, confirming structural robustness of the freestanding VDWTFs. (N) Water vapor transmission through VDWTFs of different thickness versus transepidermal water loss (TEWL). See the supplementary materials for a description of the "open bottle" and "closed bottle" conditions.

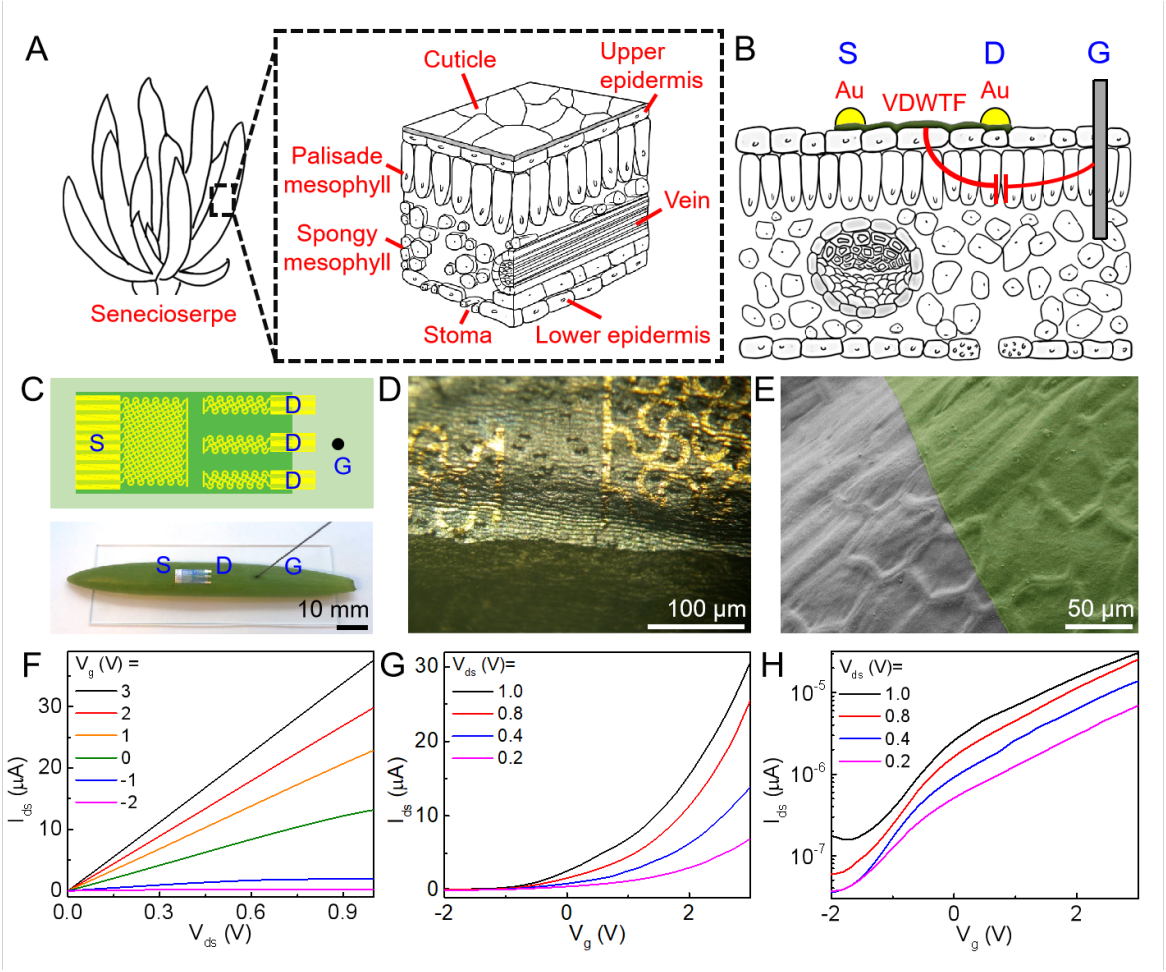

Figure 4.3: Leaf-gate VDWTF transistors. (A) Diagram of a Senecio mandraliscae leaf. (B) Cross-sectional view of the leaf-gate transistor with Au source and drain electrodes ("S" and "D," respectively) and an inserted tungsten gate electrode ("G"). (C) Schematic illustration (top; leaf, light green; VDWTF, dark green; Au electrodes, yellow; tungsten probe, black dot) and photograph of the leaf-gate transistor (bottom). (D) Optical image of a VDWTF with serpentine Au electrodes transferred onto the plant leaf. (E) Colorized SEM image of the VDWTF on the leaf. (F) Output characteristics of a leaf-gate transistor. V_{ds} , drain-source voltage; I_{ds} , drain-source current. (G and H) Transfer curves with (G) linear and (H) logarithmic axis. V_g, gate voltage.

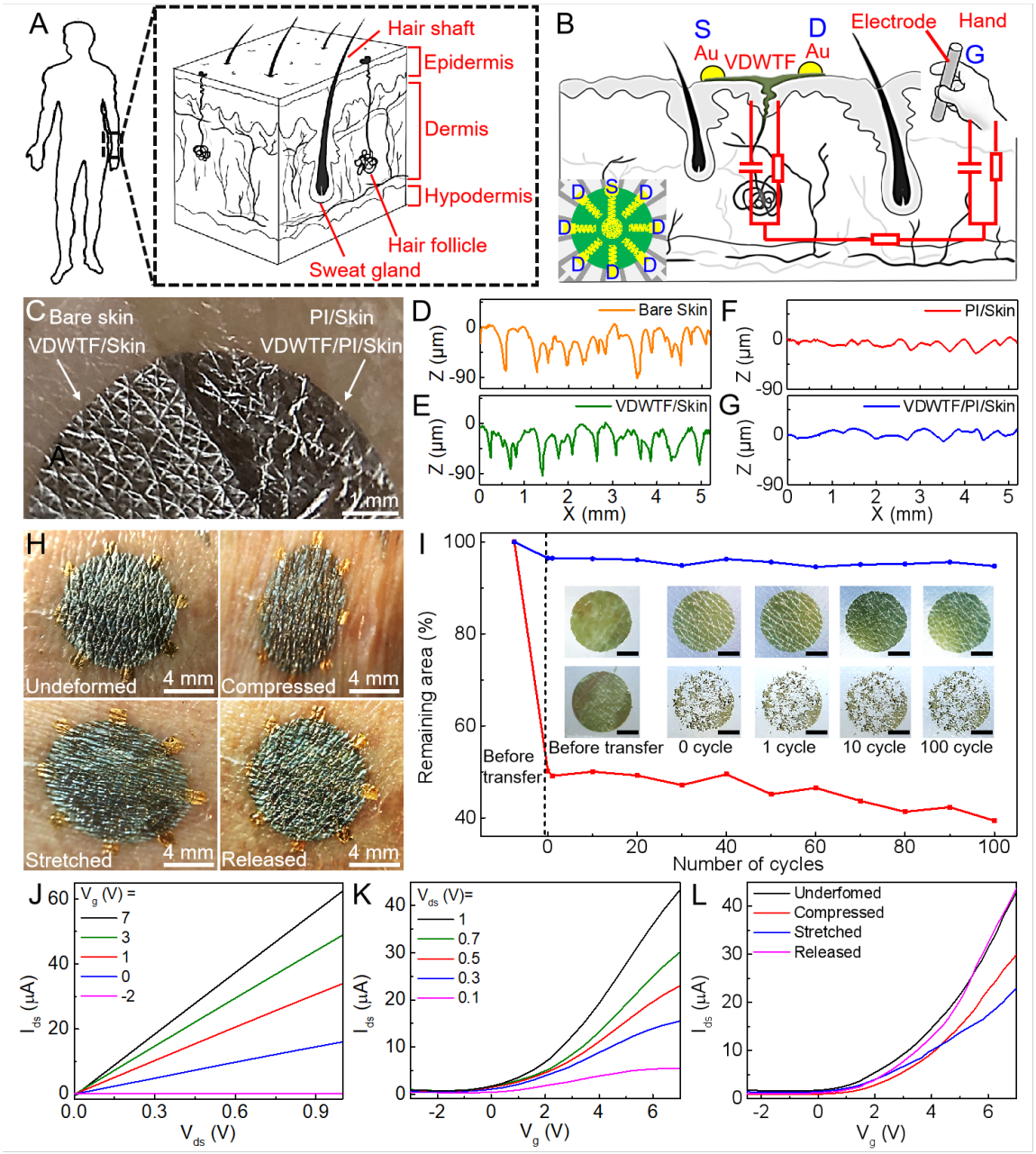

Figure 4.4: Skin-gate VDWTF transistors. (A) The structure of human skin. (B) Schematic of a skin-gate VDWTF transistor with Au source and drain electrodes and an iron rod gate electrode held by a human subject. (C) Photograph of the freestanding VDWTF on a replica of human skin (left) and the VDWTF supported by a 1.6- μm-thick polyimide substrate on a replica of human skin (right). (D to G) Height profiles corresponding to the line scan in

different areas of (C). (H) Skin- gate VDWTF transistor on human skin under different types of mechanical deformation. (I) Remaining area of VDWTFs and CVDTFs on skin replicas as a function of stretching cycles (10% tensile strain). Scale bars, 2 mm. (J) Output and (K) transfer curves of a skin-gate VDWTF transistor. (L) Transfer curves under different types of deformation.

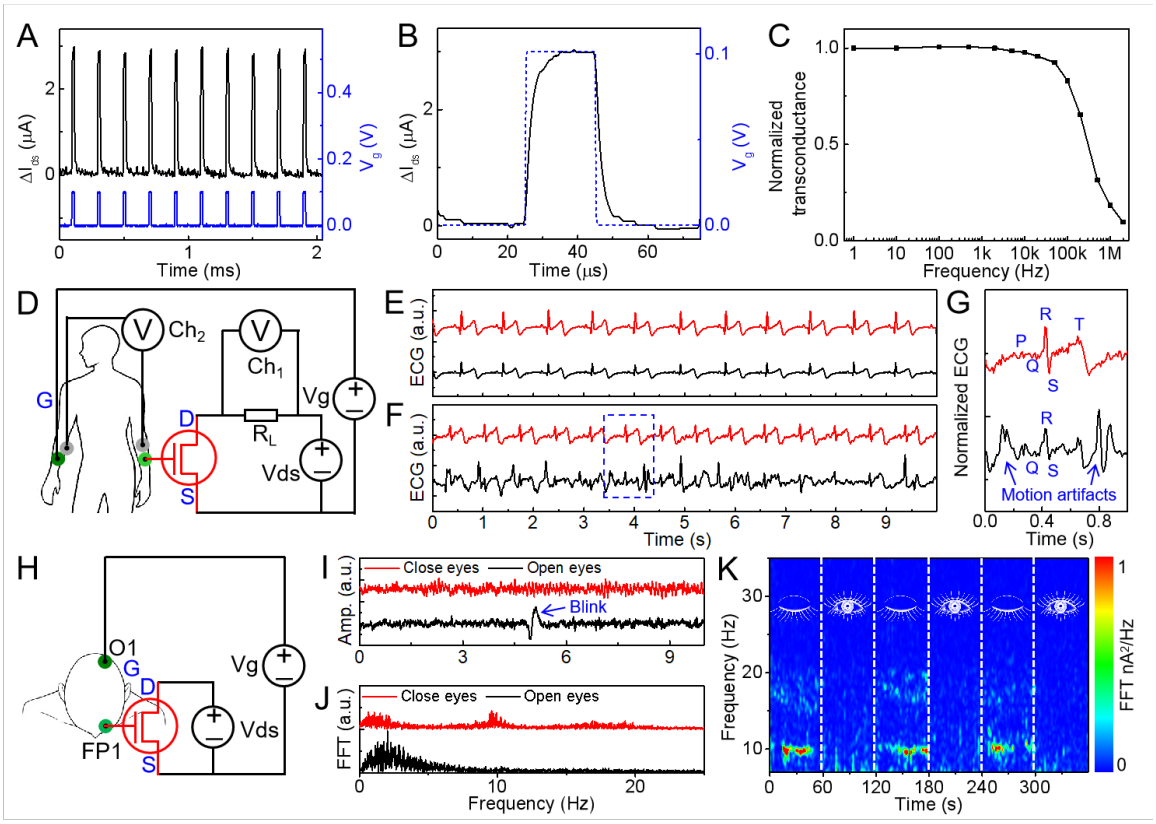

Figure 4.5: Skin-gate VDWTF transistors for monitoring transient skin potentials. (A) Relative drain current (ΔI_{ds}) of a skin-gate VDWTF transistor stimulated by 5 kHz 0.1-V 20-μs-wide gate pulses at a V_{ds} of 0.1 V. (B) The response time of the skin-gate VDWTF transistor to a square gate pulse (blue dashed line). (C) Normalized transconductance at various frequencies. (D) Schematic diagram of the ECG measurement with a V_{ds} of 0.5 V and a V_g of 0.5 V. (E and F) The ECG signals measured by the skin-gate transistor (red line) and Ag/AgCl electrode (black line) (E) before and (F) during human exercise. a.u., arbitrary units. (G) Zoomed-in view of boxed portion in (F), showing clear P, QRS, and T waves from the skin-gate transistor but only a QRS wave and motion artifacts from the Ag/AgCl electrodes. (H) Schematic diagram of the EEG measurement. (I) Recorded EEG signals using a skin-gate transistor when a human subject was engaged in two mental states (closed eyes and open eyes). Eye blink artifacts are also visible. (J) Fast Fourier

transform (FFT)–processed frequency distributions of the EEG signals in (I). (K) Time-frequency spectrograms of the EEG signals recorded during cyclic eye closing and opening, showing dynamic activity of the alpha rhythm at $\sim$ 10 Hz.

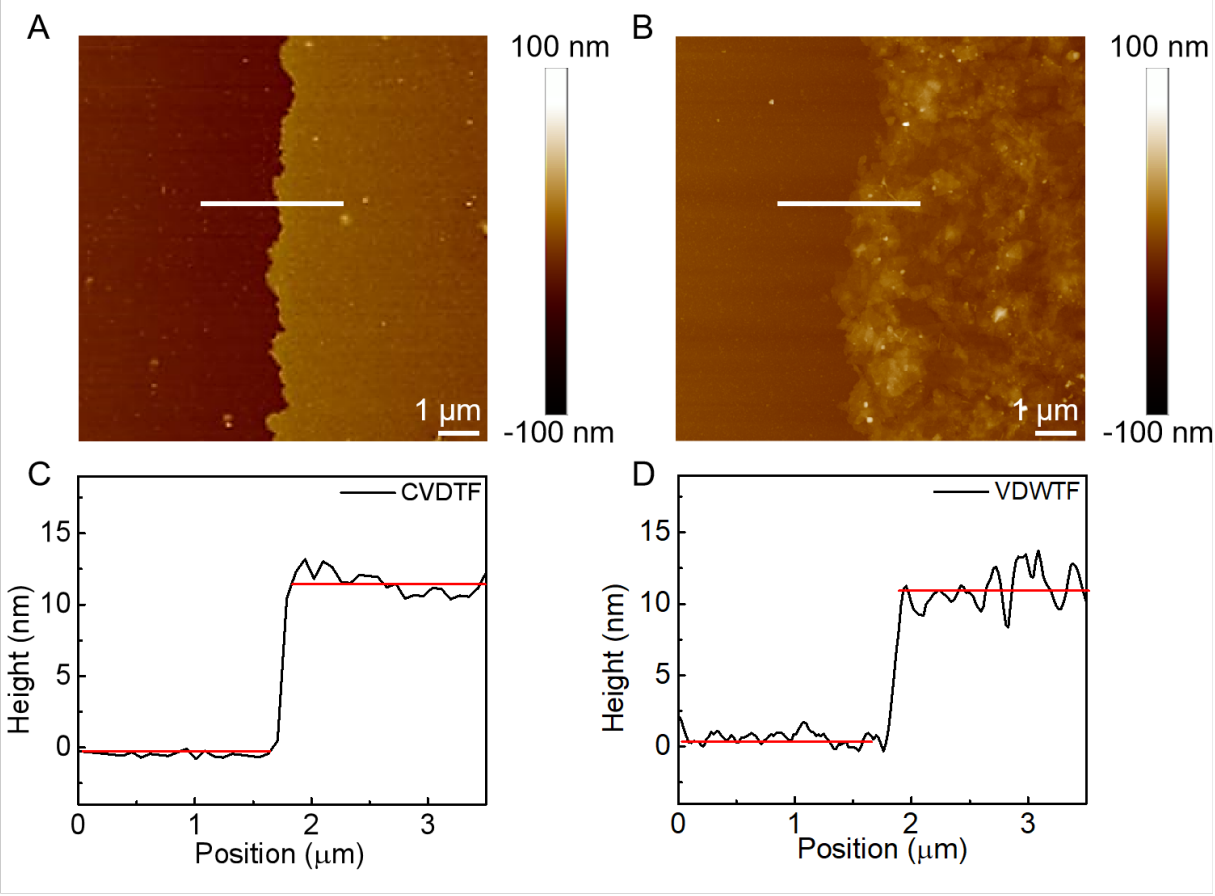

Figure 4.6: The AFM images and height profiles of CVDTF and VDWTF. (A-B) AFM images of (A) CVDTF and (B) VDWTF. (C-D) Height profiles showing the thickness of (C) CVDTF and (D) VDWTF.

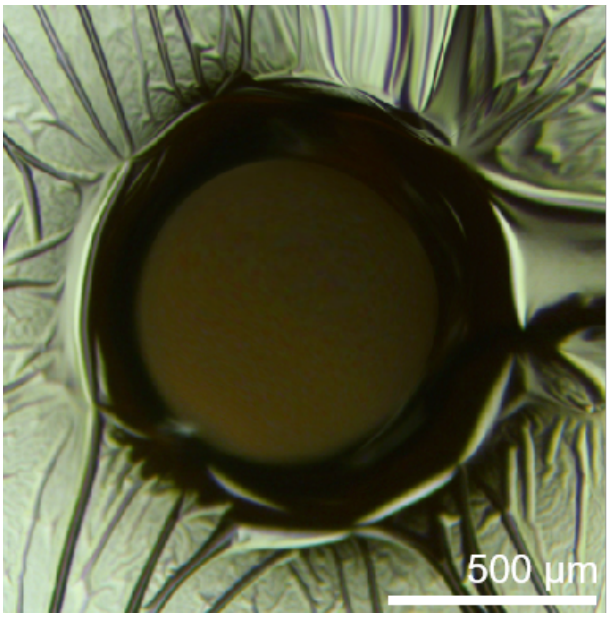

Figure 4.7: Optical image of a CVDTF transferred over a single hole (1 mm in diameter, polyimide substrate) showing complete rupture.

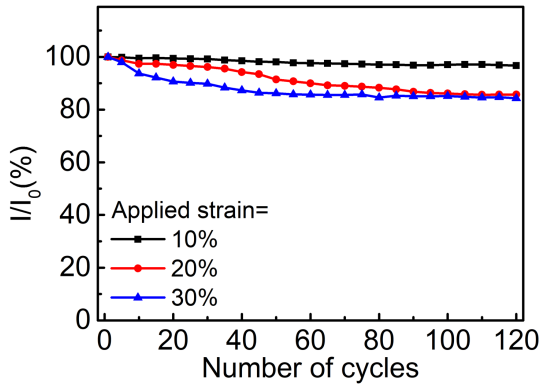

Figure 4.8: Cyclic stability of the VDWTF supported on PDMS substrate under repeated tensile strain cycles of 10%, 20% and 30% for 120 cycles. The results illustrate that there is $< 4\%$ degradation in I_{ds} of VDWTF after 120 cyclic stretching cycles with 10% applied strain. When the applied strain is increased to 20% and 30%, the I_{ds} of VDWTF decreases to about 84% of its initial state during first 90 stretching cycles, and then remains about 84% from 90 to 120 cycles.

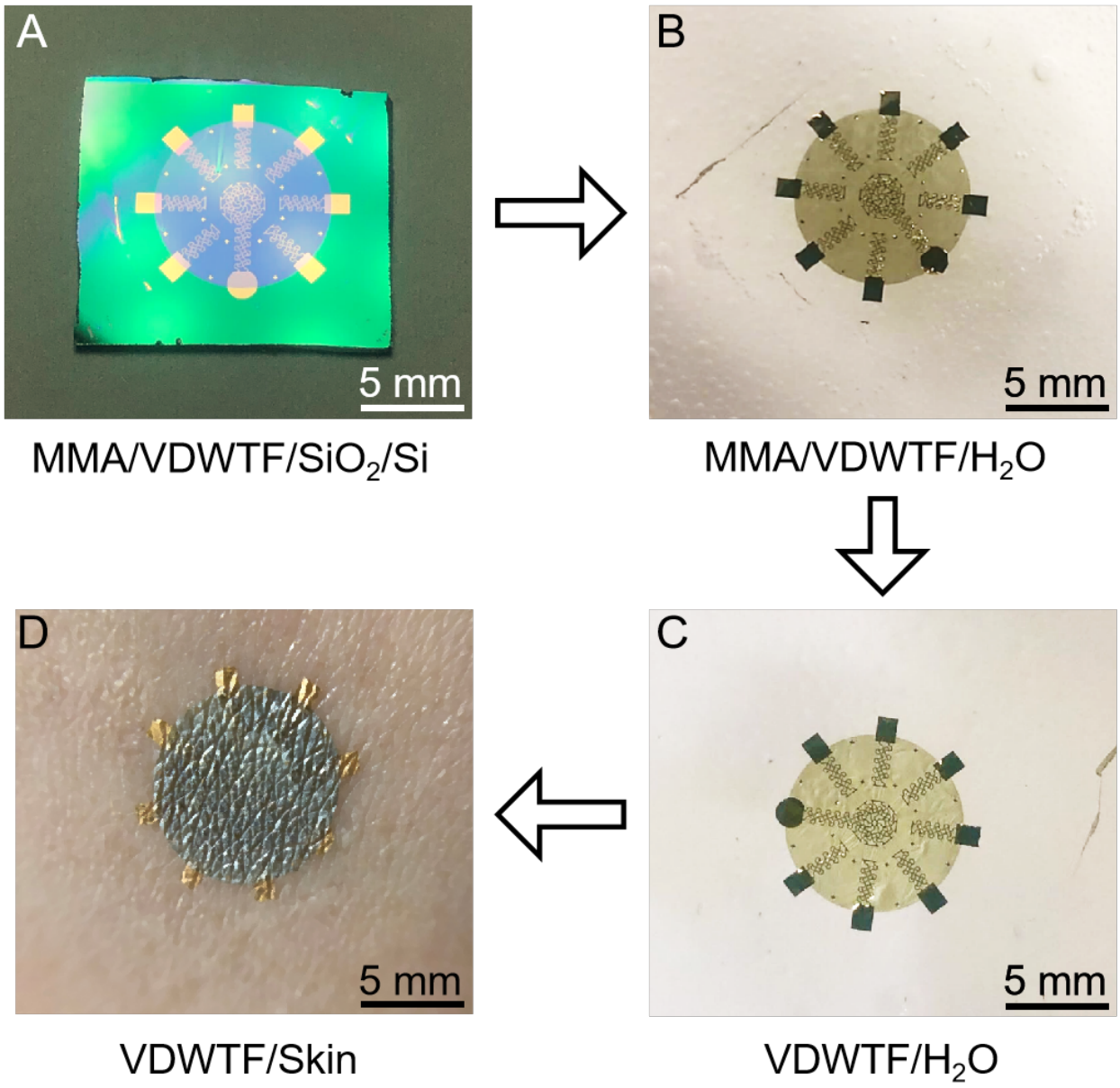

Figure 4.9: Transfer process and photographs of the skin-gate VDWTF transistor. (A) Photographs of the VDWTF and Au electrodes deposited on a SiO_2 substrate, (B) floating on the water with a layer of 50-nm-thick MMA, (C) without MMA layer (MMA dissolved by acetone vapor) and (D) transferred onto human skin.

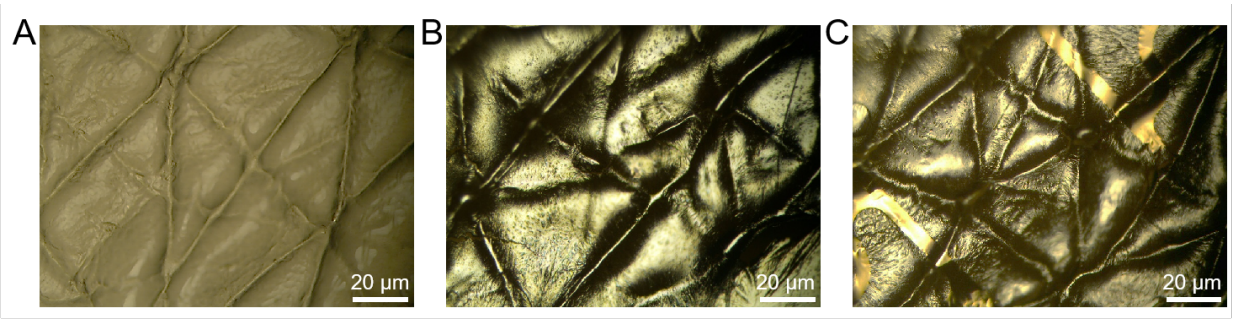

Figure 4.10: Optical microscopy images of skin-gate VDWTF transistors on skin replica. (A) Optical image of bare human skin replica, (B) VDWTF on skin replica, and (C) VDWTF with serpentine-mesh-layout Au electrodes on skin replicas.

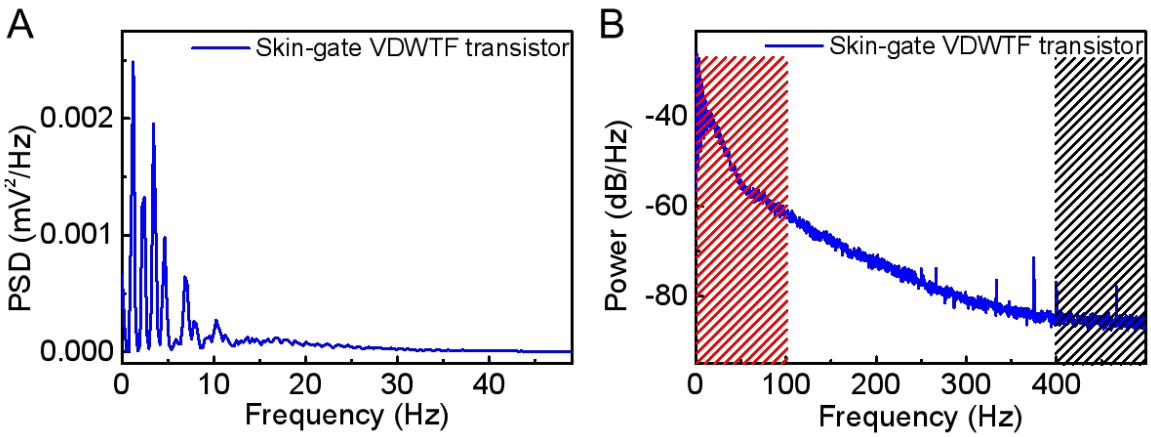

Figure 4.11: (A) Power spectral density of ECG signals obtained using skin-gate VDWTF transistors and (B) that in decibels (dB). The frequency range of ECG signals is typically below 100 Hz, thus the region below 100 Hz (red region in B) is chosen to represent our signal in the SNR calculation. The noise is averaged from the noise floor region in 400−500 Hz (black region in B)

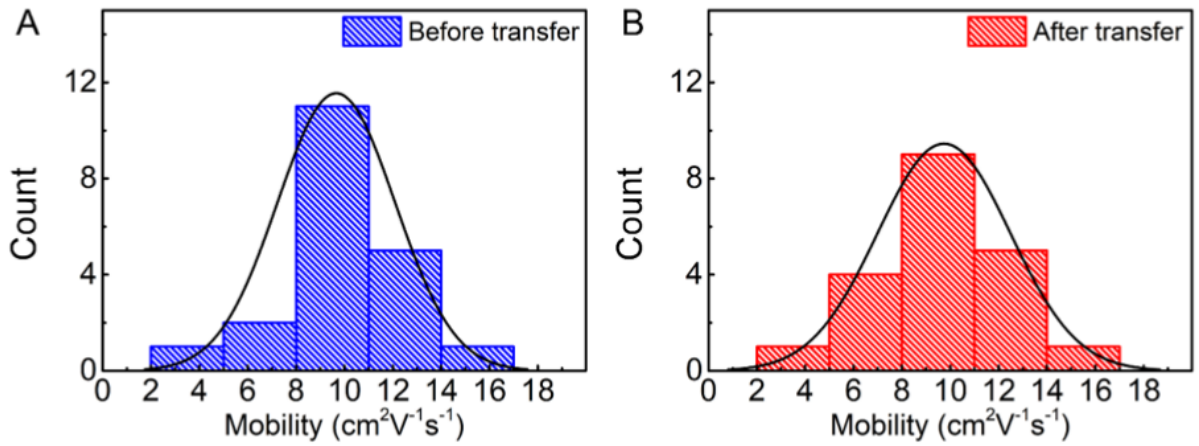

Figure 4.12: The device mobility distributions. (A) The histogram of the carrier mobility values for 20 individual transistors fabricated from the as-prepared VDWTFs. (B) The histogram of the carrier mobility values for 20 individual transistors fabricated from the transferred VDWTFs. The as−prepared and transferred VDWTFs show comparable electronic properties.

Movie S1 − S4 url:

www.science.org/doi/suppl/10.1126/science.abl8941/suppl_file/science.abl8941_movies_s1_to_s4.zip

References

[1] George D. Spyropoulos, Jennifer N. Gelinas, and Dion Khodagholy. Internal ion-gated organic electrochemical transistor: A building block for integrated bioelectronics. *Science Advances*, 5(2):eaau7378, 2019.

[2] Insang You, David G. Mackanic, Naoji Matsuhisa, Jiheong Kang, Jimin Kwon, Levent Beker, Jaewan Mun, Wonjeong Suh, Tae Yeong Kim, Jeffrey B.-H. Tok, Zhenan Bao, and Unyong Jeong. Artificial multimodal receptors based on ion relaxation dynamics. *Science*, 370(6519):961–965, 2020.

[3] Faheem Ershad, Anish Thukral, Jiping Yue, Phillip Comeaux, Yuntao Lu, Hyunseok Shim, Kyoseung Sim, Nam-In Kim, Zhoulyu Rao, Ross Guevara, Luis Contreras, Fengjiao Pan, Yongcao Zhang, Ying-Shi Guan, Pinyi Yang, Xu Wang, Peng Wang, Xiaoyang Wu, and Cunjiang Yu. Ultra-conformal drawn-on-skin electronics for multifunctional motion artifact-free sensing and point-of-care treatment. *Nature Communications*, 11(1):3823, Jul 2020.

[4] Qiang Li, Kewang Nan, Paul Le Floch, Zuwan Lin, Hao Sheng, Thomas S. Blum, and Jia Liu. Cyborg organoids: Implantation of nanoelectronics via organogenesis for tissue-wide electrophysiology. *Nano Letters*, 19(8):5781–5789, 2019. PMID: 31347851.

[5] Sihong Wang, Jie Xu, Weichen Wang, Ging-Ji Nathan Wang, Reza Rastak, Francisco Molina-Lopez, Jong Won Chung, Simiao Niu, Vivian R. Feig, Jeffery Lopez, Ting Lei, Soon-Ki Kwon, Yeongin Kim, Amir M. Foudeh, Anatol Ehrlich, Andrea Gasperini, Youngjun Yun, Boris Murmann, Jeffery B.-H. Tok, and Zhenan Bao. Skin electronics from scalable fabrication of an intrinsically stretchable transistor array. *Nature*, 555(7694):83–88, Mar 2018.

[6] Kyoseung Sim, Zhoulyu Rao, Hae-Jin Kim, Anish Thukral, Hyunseok Shim, and Cun-

jiang Yu. Fully rubbery integrated electronics from high effective mobility intrinsically stretchable semiconductors. *Science Advances*, 5(2):eaav5749, 2019.

[7] Eleni Stavrinidou, Roger Gabrielsson, Eliot Gomez, Xavier Crispin, Ove Nilsson, Daniel T. Simon, and Magnus Berggren. Electronic plants. *Science Advances*, 1(10):e1501136, 2015.

[8] Kyeongha Kwon, Jong Uk Kim, Yujun Deng, Siddharth R. Krishnan, Jungil Choi, Hokyung Jang, KunHyuck Lee, Chun-Ju Su, Injae Yoo, Yixin Wu, Lindsay Lipschultz, Jae-Hwan Kim, Ted S. Chung, Derek Wu, Yoonseok Park, Tae-il Kim, Roozbeh Ghaffari, Stephen Lee, Yonggang Huang, and John A. Rogers. An on-skin platform for wireless monitoring of flow rate, cumulative loss and temperature of sweat in real time. *Nature Electronics*, 4(4):302–312, Apr 2021.

[9] Jahyun Koo, Matthew R. MacEwan, Seung-Kyun Kang, Sang Min Won, Manu Stephen, Paul Gamble, Zhaoqian Xie, Ying Yan, Yu-Yu Chen, Jiho Shin, Nathan Birenbaum, Sangjin Chung, Sung Bong Kim, Jawad Khalifeh, Daniel V. Harburg, Kelsey Bean, Michael Paskett, Jeonghyun Kim, Zohny S. Zohny, Seung Min Lee, Ruoyao Zhang, Kaijing Luo, Bowen Ji, Anthony Banks, Hyuck Mo Lee, Younggang Huang, Wilson Z. Ray, and John A. Rogers. Wireless bioresorbable electronic system enables sustained nonpharmacological neuroregenerative therapy. *Nature Medicine*, 24(12):1830–1836, Dec 2018.

[10] Mengdi Han, Lin Chen, Kedar Aras, Cunman Liang, Xuexian Chen, Hangbo Zhao, Kan Li, Ndeye Rokhaya Faye, Bohan Sun, Jae-Hwan Kim, Wubin Bai, Quansan Yang, Yuhang Ma, Wei Lu, Enming Song, Janice Mihyun Baek, Yujin Lee, Clifford Liu, Jeffrey B. Model, Guanjun Yang, Roozbeh Ghaffari, Yonggang Huang, Igor R. Efimov, and John A. Rogers. Catheter-integrated soft multilayer electronic arrays for multiplexed sensing and actuation during cardiac surgery. *Nature Biomedical Engineering*, 4(10):997–1009, Oct 2020.

[11] Mallika Bariya, Hnin Yin Yin Nyein, and Ali Javey. Wearable sweat sensors. *Nature Electronics*, 1(3):160–171, Mar 2018.

[12] J.A. Rogers, R. Ghaffari, and D.H. Kim. *Stretchable Bioelectronics for Medical Devices and Systems*. Microsystems and Nanosystems. Springer International Publishing, 2016.

[13] Sang Hoon Chae, Woo Jong Yu, Jung Jun Bae, Dinh Loc Duong, David Perello, Hye Yun Jeong, Quang Huy Ta, Thuc Hue Ly, Quoc An Vu, Minhee Yun, Xiangfeng Duan, and Young Hee Lee. Transferred wrinkled al2o3 for highly stretchable and transparent graphene–carbon nanotube transistors. *Nature Materials*, 12(5):403–409, May 2013.

[14] Jongseung Yoon, Alfred J. Baca, Sang-Il Park, Paulius Elvikis, Joseph B. Geddes, Lanfang Li, Rak Hwan Kim, Jianliang Xiao, Shuodao Wang, Tae-Ho Kim, Michael J. Motala, Bok Yeop Ahn, Eric B. Duoss, Jennifer A. Lewis, Ralph G. Nuzzo, Placid M. Ferreira, Yonggang Huang, Angus Rockett, and John A. Rogers. Ultrathin silicon solar microcells for semitransparent, mechanically flexible and microconcentrator module designs. *Nature Materials*, 7(11):907–915, Nov 2008.

[15] Dahl-Young Khang, Hanqing Jiang, Young Huang, and John A. Rogers. A stretchable form of single-crystal silicon for high-performance electronics on rubber substrates. *Science*, 311(5758):208–212, 2006.

[16] Dae-Hyeong Kim, Nanshu Lu, Rui Ma, Yun-Soung Kim, Rak-Hwan Kim, Shuodao Wang, Jian Wu, Sang Min Won, Hu Tao, Ahmad Islam, Ki Jun Yu, Tae il Kim, Raeed Chowdhury, Ming Ying, Lizhi Xu, Ming Li, Hyun-Joong Chung, Hohyun Keum, Martin McCormick, Ping Liu, Yong-Wei Zhang, Fiorenzo G. Omenetto, Yonggang Huang, Todd Coleman, and John A. Rogers. Epidermal electronics. *Science*, 333(6044):838–843, 2011.

[17] Limei Tian, Benjamin Zimmerman, Aadeel Akhtar, Ki Jun Yu, Matthew Moore, Jian Wu, Ryan J. Larsen, Jung Woo Lee, Jinghua Li, Yuhao Liu, Brian Metzger, Subing Qu, Xiaogang Guo, Kyle E. Mathewson, Jonathan A. Fan, Jesse Cornman, Michael

Fatina, Zhaoqian Xie, Yinji Ma, Jue Zhang, Yihui Zhang, Florin Dolcos, Monica Fabiani, Gabriele Gratton, Timothy Bretl, Levi J. Hargrove, Paul V. Braun, Yonggang Huang, and John A. Rogers. Large-area mri-compatible epidermal electronic interfaces for prosthetic control and cognitive monitoring. *Nature Biomedical Engineering*, 3(3):194–205, Mar 2019.

[18] Zhenlong Huang, Yifei Hao, Yang Li, Hongjie Hu, Chonghe Wang, Akihiro Nomoto, Taisong Pan, Yue Gu, Yimu Chen, Tianjiao Zhang, Weixin Li, Yusheng Lei, NamHeon Kim, Chunfeng Wang, Lin Zhang, Jeremy W. Ward, Ayden Maralani, Xiaoshi Li, Michael F. Durstock, Albert Pisano, Yuan Lin, and Sheng Xu. Three-dimensional integrated stretchable electronics. *Nature Electronics*, 1(8):473–480, Aug 2018.

[19] Jonathan Rivnay, Sahika Inal, Alberto Salleo, Róisín M. Owens, Magnus Berggren, and George G. Malliaras. Organic electrochemical transistors. *Nature Reviews Materials*, 3(2):17086, Jan 2018.

[20] Yan Fang, Xinming Li, and Ying Fang. Organic bioelectronics for neural interfaces. *J. Mater. Chem. C*, 3:6424–6430, 2015.

[21] Lili Cai, Alex Y. Song, Peilin Wu, Po-Chun Hsu, Yucan Peng, Jun Chen, Chong Liu, Peter B. Catrysse, Yayuan Liu, Ankun Yang, Chenxing Zhou, Chenyu Zhou, Shanhui Fan, and Yi Cui. Warming up human body by nanoporous metallized polyethylene textile. *Nature Communications*, 8(1):496, Sep 2017.

[22] Zhuocheng Yan, Taisong Pan, Miaomiao Xue, Changyong Chen, Yan Cui, Guang Yao, Long Huang, Feiyi Liao, Wei Jing, Hulin Zhang, Min Gao, Daqing Guo, Yang Xia, and Yuan Lin. Thermal release transfer printing for stretchable conformal bioelectronics. *Advanced Science*, 4(11):1700251, 2017.

[23] Yujie Liu, Yu-Cheng Chen, Shelby Hutchens, Jimmy Lawrence, Todd Emrick, and

Alfred J. Crosby. Directly measuring the complete stress–strain response of ultrathin polymer films. *Macromolecules*, 48(18):6534–6540, 2015.

[24] Jonathan N. Coleman, Mustafa Lotya, Arlene O'Neill, Shane D. Bergin, Paul J. King, Umar Khan, Karen Young, Alexandre Gaucher, Sukanta De, Ronan J. Smith, Igor V. Shvets, Sunil K. Arora, George Stanton, Hye-Young Kim, Kangho Lee, Gyu Tae Kim, Georg S. Duesberg, Toby Hallam, John J. Boland, Jing Jing Wang, John F. Donegan, Jaime C. Grunlan, Gregory Moriarty, Aleksey Shmeliov, Rebecca J. Nicholls, James M. Perkins, Eleanor M. Grieveson, Koenraad Theuwissen, David W. McComb, Peter D. Nellist, and Valeria Nicolosi. Two-dimensional nanosheets produced by liquid exfoliation of layered materials. *Science*, 331(6017):568–571, 2011.

[25] Zhaoyang Lin, Yuan Liu, Udayabagya Halim, Mengning Ding, Yuanyue Liu, Yiliu Wang, Chuancheng Jia, Peng Chen, Xidong Duan, Chen Wang, Frank Song, Mufan Li, Chengzhang Wan, Yu Huang, and Xiangfeng Duan. Solution-processable 2d semiconductors for high-performance large-area electronics. *Nature*, 562(7726):254–258, Oct 2018.

[26] Zhaoyang Lin, Yu Huang, and Xiangfeng Duan. Van der waals thin-film electronics. *Nature Electronics*, 2(9):378–388, Sep 2019.

[27] Daryl McManus, Sandra Vranic, Freddie Withers, Veronica Sanchez-Romaguera, Massimo Macucci, Huafeng Yang, Roberto Sorrentino, Khaled Parvez, Seok-Kyun Son, Giuseppe Iannaccone, Kostas Kostarelos, Gianluca Fiori, and Cinzia Casiraghi. Water-based and biocompatible 2d crystal inks for all-inkjet-printed heterostructures. *Nature Nanotechnology*, 12(4):343–350, Apr 2017.

[28] Jae-Woong Jeong, Woon-Hong Yeo, Aadeel Akhtar, James J. S. Norton, Young-Jin Kwack, Shuo Li, Sung-Young Jung, Yewang Su, Woosik Lee, Jing Xia, Huanyu Cheng, Yonggang Huang, Woon-Seop Choi, Timothy Bretl, and John A. Rogers. Materials and

optimized designs for human-machine interfaces via epidermal electronics. *Advanced Materials*, 25(47):6839–6846, 2013.

[29] John A. Rogers, Takao Someya, and Yonggang Huang. Materials and mechanics for stretchable electronics. *Science*, 327(5973):1603–1607, 2010.

[30] Yu-Ki Lee, Zhonghua Xi, Young-Joo Lee, Yun-Hyeong Kim, Yue Hao, Hongjin Choi, Myoung-Gyu Lee, Young-Chang Joo, Changsoon Kim, Jyh-Ming Lien, and In-Suk Choi. Computational wrapping: A universal method to wrap 3d-curved surfaces with non-stretchable materials for conformal devices. *Science Advances*, 6(15):eaax6212, 2020.

[31] C.E. Carraher. *Giant Molecules: Essential Materials for Everyday Living and Problem Solving*. Wiley InterScience electronic collection. Wiley, 2003.

[32] Yu-Qing Zheng, Yuxin Liu, Donglai Zhong, Shayla Nikzad, Shuhan Liu, Zhiao Yu, Deyu Liu, Hung-Chin Wu, Chenxin Zhu, Jinxing Li, Helen Tran, Jeffrey B.-H. Tok, and Zhenan Bao. Monolithic optical microlithography of high-density elastic circuits. *Science*, 373(6550):88–94, 2021.

[33] Baoxing Xu and Xi Chen. Determining engineering stress-strain curve directly from the load-depth curve of spherical indentation test. *Journal of Materials Research*, 25(12):2297–2307, Dec 2010.

[34] O.N. Scott, M.R. Begley, U. Komaragiri, and T.J. Mackin. Indentation of freestanding circular elastomer films using spherical indenters. *Acta Materialia*, 52(16):4877–4885, 2004.

[35] Xin Fang, Chunhua Zhang, Xun Chen, Yashun Wang, and Yuanyuan Tan. A new universal approximate model for conformal contact and non-conformal contact of spherical surfaces. *Acta Mechanica*, 226(6):1657–1672, Jun 2015.

[36] Shuodao Wang, Ming Li, Jian Wu, Dae-Hyeong Kim, Nanshu Lu, Yewang Su, Zhan Kang, Yonggang Huang, and John A. Rogers. Mechanics of Epidermal Electronics. *Journal of Applied Mechanics*, 79(3), 04 2012. 031022.

[37] Yalin Yu, Daniel Sanchez, and Nanshu Lu. Work of adhesion/separation between soft elastomers of different mixing ratios. *Journal of Materials Research*, 30(18):2702–2712, Sep 2015.

[38] John J. Boland. Within touch of artificial skin. *Nature Materials*, 9(10):790–792, Oct 2010.

[39] Jan Kottner, Andrea Lichterfeld, and Ulrike Blume-Peytavi. Transepidermal water loss in young and aged healthy humans: a systematic review and meta-analysis. *Archives of Dermatological Research*, 305(4):315–323, May 2013.

[40] Taisong Pan, Matt Pharr, Yinji Ma, Rui Ning, Zheng Yan, Renxiao Xu, Xue Feng, Yonggang Huang, and John A. Rogers. Experimental and theoretical studies of serpentine interconnects on ultrathin elastomers for stretchable electronics. *Advanced Functional Materials*, 27(37):1702589, 2017.

CHAPTER 5

From van der Waals thin film to intergrated system

5.1 Introduction

Integrated systems with the ability to instantaneously monitor the bio signals of living organisms is of increasing interest for many emerging applications like diagnosing and treating human diseases [1]. A rubust system that should be able to accurately measure the signals, process the signal and transmit the necessary information to patients. Therefore this kind of device comes with a package of different elements with designated functions. First, the system should have a rubust sensor which can fit the arbitrary featured surfaces of the bio targets and measure the signal with a high signal to noise ratio. Second, the detected signal should be processed on site, including screen out the noise, and deliver the information to patient instantaneously. Third, the whole system needs to be isolated and has its own power supply system as the out wiring makes the system bulky and inconvenient to be carried with humans. Also too many wiring will cause unwanted noise from the connections parts. Therefore the ideal solution is to have a small portable device with power supply and wireless communication system that are connected to the sensor.

5.2 Integration of the devices

Previsously we introduced van der Waals thin film (VDWTF) as a great candidate for flexible electronics as it has a great flexibility and can match with any arbitrary featured bio

target surfaces. Also the van der Waals between flakes inside the thin film allows the flakes to slide with each other to compensate the stress generated during motions. Therefore we have a high performance sensor for the purpose of on site signal measurements. However, just a sensor part is not enough for the whole system. The thin film itself can match with the arbitrary surface and tolerate the motion artifacts, but the wiring part of the whole device are usually made with more rigid materials to support the metal wires as the metals are not conformal and robust like the thin film and therefore need substrates to hold their integrity. And this will make the wiring more rigid compared with the thin film part, even with polymer substrate, and thus the wiring part will be much easier to detach from the target and lead to a disconnection between inside the sensor. Moreover, during the motion of the target, the rigid parts can easily scratch the soft VDWTF and cause permanent damage to the device. As a result, we cannot directly connect the thin film sensor with the metal wiring part and need a joint part.

This joint materials have several requirements. First, the joint needs to be electrically conductive enough so the voltage will be mainly applied on the sensor and targets, also the joint should form ohmic contact with both the metal wires and the thin film. Second, the joint should be able to tolerate the motion artifacts and maintain its connections mechanically and electrically. Third, the materials should have long lifetime and can not be toxic to the target. In general this joint part should be conductive, sticky and harmless. And based on these requirements we have tried several candidates.

The first one is liquid metal and alloy, which is germanium and its alloys. Ge is a metal so the electric conductivity is very high, which can perfectly meet the first requirement. Also it is a liquid so it can tolerate any deformation and still maintain its conductivity. But Ge can form alloys with many metals and materials including gold, which is used for our wires, and also our thin film materials, which means Ge is corrosive to our device. The second one

we tried is a mixture of graphite and syrup. The syrup is further heated up to evaporate the redundant water, so it is very sticky and can maintain the connection between the wire and thin film. But it is still a fluid so it can release the stress in motion. The graphite is small conductive particles and with certain concentrations it can form a mesh inside the syrup to support electron transport. However, this syrup is more resistive than metallic materials as the connection in the graphite mesh is still a point to point connection between each particles and thus conductivity is lower than metal. And this high resistance will draw more voltage to it and generate a lots of noise.

A potential solution is self-adhesive styrene-ethylene-butylene-styrene (SEBS) [2] thermoplastic elastomer coated with gold particles. The SEBS is self-adhesive so it can attach to the surface of thin film and electrodes and maintain the connection during motions. Also this type of polymers has certain viscosity and can change it shape under external perturbation. Therefore it can tolerate motion by release the extra stress. Moreover the gold particles are embedded on the surface so they will maintain the position under deformation and thus provide a good conductivity.

The solution of the connection part between the thin film sensor and the wires is just a start. The whole system has many parts with different functions. A typical integrated system is shown in Fig. 5.1 [3]. This device is used to measure the ECG signal from the target and transfer the signal to a cell phone app to instantaneous monitor the health of patient. The sensor on this device is a commercial ECG front end and is embedded into a flexible PCB, which is much simpler to build. Our system actually requires a transfer or spray process to coat our thin film sensor on to the target as the sensor is too thin to be handled with other bulky parts of the system. Then we need to make the connection between our sensor and the wires with additional joint materials. The rest parts could be easier because the signal process and transmission part can be located on comparatively stable part on muscles like

arms or chests so these parts would not experience many motion artifacts. We can put the sensor on the targets and use a conduit to connect the sensor with the rest parts and in this way only the sensor and the joints need to endure the motions which could reduce the work for the whole design. We need a motion free sensor because most of the valuable signals we can probe on human body are from the parts with less muscles and are close to vessels. And these parts are usually the joint between bonds like wrists. But those parts are also the flexible parts on body and can easily move. So it is important to have a robust sensor to detect the signal from these parts.

5.3 Current Process: Cuffless Blood Pressure Measurement

Conventional measurement of blood pressure requires a cuff to exert external pressure over human body to measure the really pressure. This method is accurate but bulky. A cuffless way is to measure other signals which are correlated with the blood pulse go through human body and then derive the really blood pressure. As shown in Fig 5.2 and Fig 5.3 [2], when the blood pulse go through forearm, it will generate a small change in the impedance of the tissue and blood. And thus by measuring the impedance change we can derive the blood pressure from it. However, the capacitance of human skin is very high and therefore the change in the total impedance is comparatively low (Fig 5.3B). To extract this signal precisely, a AC voltage is applied over the forearm to overcome the high capacitance and in this way we can measure the small change of impedance.

Our design is to use our VDWTF as pads to extract electric signal from forearm. And as the VDWTF is extremely conformal to human skin, we can get a very high signal to noise ratio. As shown in Fig 5.4, we use a syrup mixed graphite to temporarily solve the connection problem mentioned above and use a 4 probe measurement to measure the impedance change

in human forearm when blood pulse pass through. The results show waveforms similar to the reported ones (Fig 5.3C and D), but there are still noises. Those noises come from the connection parts between the electrodes and the measuring equipment. So in the following steps, our main focus is solving the connection problem and build an integrated system from the VDWTF pads to the power supply and signal process part, which can further reduce the noise. And with those we can build up a imperceptible health monitoring system over body surface with a very high SNR to accurately measure bio signals and provide instantaneous feedback.

5.4 Future of Thin Film Sensor

In the next steps, we need to solve the contact issue between the ultra thin VDWTF sensor and improve the whole packaging of the system to have better signal and more robust device. After that, we have to shrink the whole setup onto integrated circuits, which can be portable with target in daily life and can transfer the signal wireless to cell phone or personal computers for analysis and health monitoring. Moreover, an integrated system will further reduce the noise. And this step needs collaboration with other departments like electronic engineering. Also, the measured data need to be analysed by medical experts. With those we can develop a breathable and imperceptible on skin platform for health monitoring and medical study.

5.5 Figures and Legends

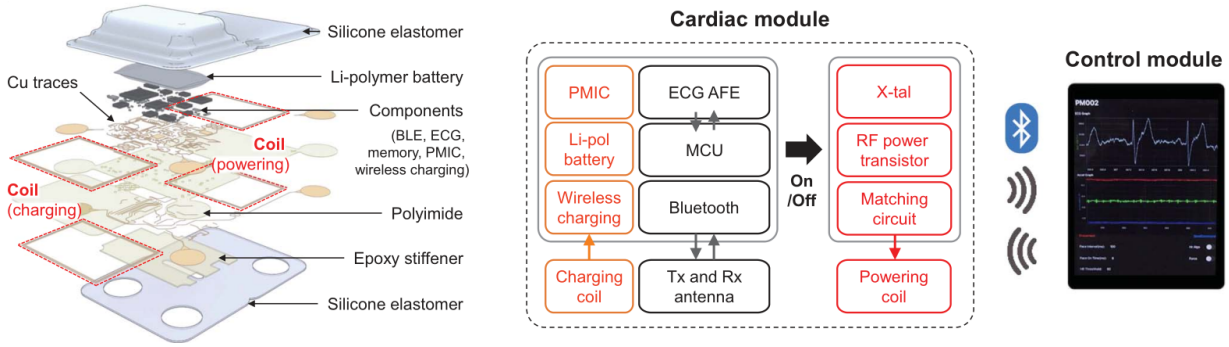

Figure 5.1: Diagram of a typical on site cardiac sensor with wireless communication and power supply[3]

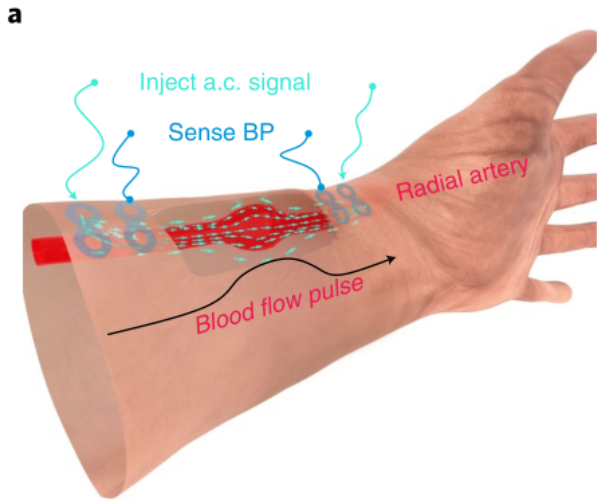

Figure 5.2: Illustration of Z-BP measurement modality[2]

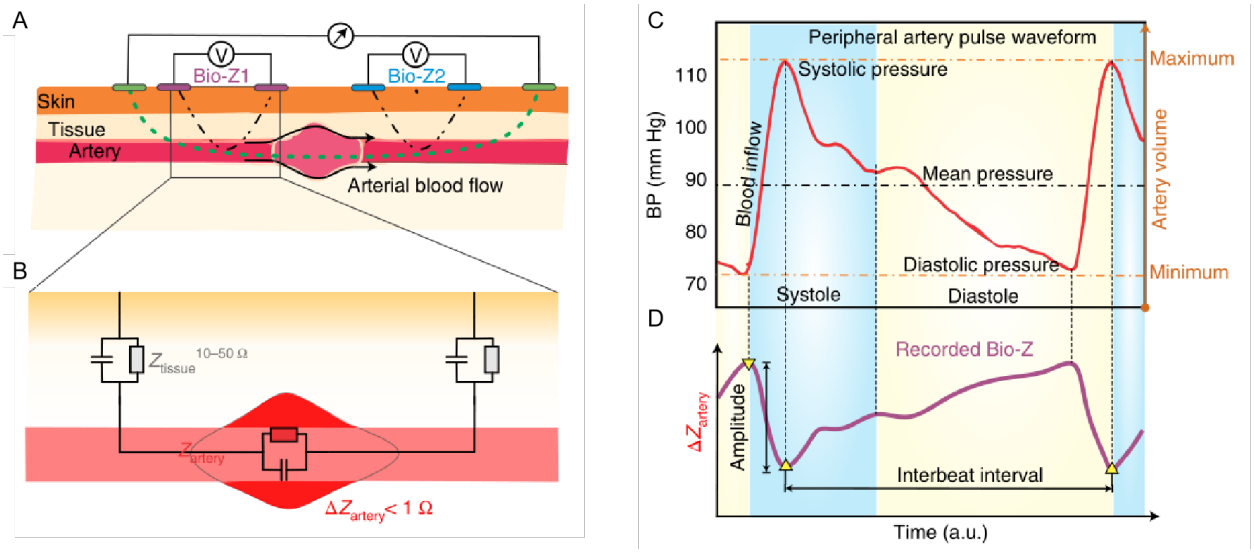

Figure 5.3: Illustration of Z-BP measurement modality[2]: A, Cross-section of the six GETs, with green lines representing the a.c. injected signal and grey lines representing voltage sensing. B, Close-up view of one pair of sensing GETs and the simplified equivalent electrical circuit of the interface. C and D, Correlation between arterial BP and bioimpedance.

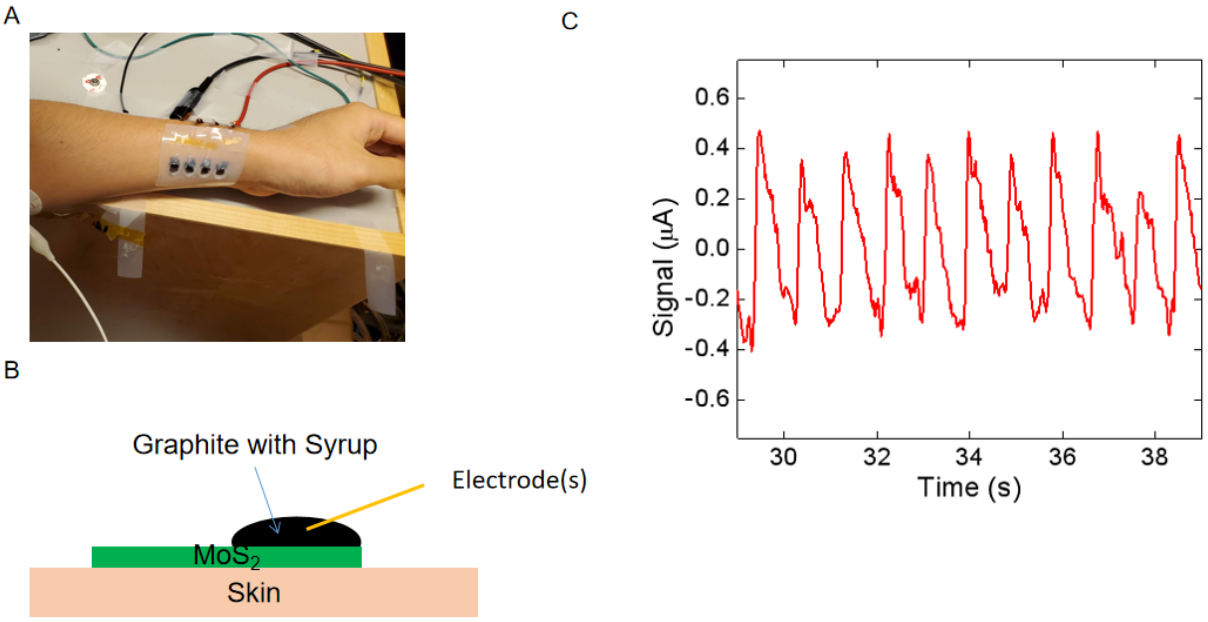

Figure 5.4: Current measurement: A. Schematics of on skin test. B, Schematics of thin film device connected with electrode with conductive gel. C, Typical blood pressure data measured.

References

[1] George D Spyropoulos, Jennifer N Gelinas, and Dion Khodagholy. Internal ion-gated organic electrochemical transistor: A building block for integrated bioelectronics. *Science advances*, 5(2):eaau7378, 2019.

[2] Ying Jiang, Shaobo Ji, Jing Sun, Jianping Huang, Yuanheng Li, Guijin Zou, Teddy Salim, Changxian Wang, Wenlong Li, Haoran Jin, et al. A universal interface for plug-and-play assembly of stretchable devices. *Nature*, 614(7948):456–462, 2023.

[3] Yeon Sik Choi, Hyoyoung Jeong, Rose T Yin, Raudel Avila, Anna Pfenniger, Jaeyoung Yoo, Jong Yoon Lee, Andreas Tzavelis, Young Joong Lee, Sheena W Chen, et al. A transient, closed-loop network of wireless, body-integrated devices for autonomous electrotherapy. *Science*, 376(6596):1006–1012, 2022.

CHAPTER 6

Chapter 2 Supplement: Robust Flexible Pressure Sensors Made from Conductive Micropyramids for Manipulation Tasks

6.1 Introduction

Electronic skin (E-skin) has attracted considerable attention for the emerging fields of prosthesis, robotics and artificial intelligence (AI) [1–14]. As a key part of E-skin, flexible pressure sensors mimicking the characteristics of slow-adapting type I (SA-I) mechanoreceptors are highly desirable [3, 8–13], which is essential not only for detecting subtle static pressures in the low pressure range ($<$ 10 kPa), but also for ensuring precise and stable control of static pressures to accomplish manipulation tasks in the medium-pressure range (10$-$100 kPa). Thus, it requires pressure sensors operating in a relative wide dynamic range with high sensitivity, fast response time, sufficient robustness, low operating voltage, low power consumption, and highly uniform sensitive components in microscale. Moreover, linear pressure response and low hysteresis are also highly desirable for avoiding complex data processing.1,10 Currently, various types of flexible pressure sensors, including resistive [5, 11–27], capacitive [4, 9, 28–33], piezoelectric [34–37], and triboelectric [38–44], have been explored. Capacitive pressure sensors generally contain a deformable dielectric in which the deformation of the dielectric induced by applied pressures leads to the change of the capacitance. Typically, thinner dielectrics and/or dielectrics with higher dielectric constant could provide higher sensitivity and larger signal-to-noise ratio, but often at a sacrifice of the mechanical

and/or electrical robustness [4, 9, 28–33]. Resistive pressure sensors, which can transduce an applied pressure into the variation of resistance, featuring a simple structure, simple read-out circuits, and an ability to detect static pressures, are attractive for the applications in manipulative tasks [6, 10–13].

By creating microstructures within the sensitive layers can lead to improved compressibility and reduced viscoelasticity, and offer an effective strategy to enhance sensitivity and reduce response time of the capacitive or resistive based pressure sensors[9, 17]. For example, a typical irregular microstructure–random roughness surface–has been used to improve the sensitivity of the resistive pressure sensors. Nevertheless, the pressure response generally reaches saturation at $\sim$ 10 kPa [21, 45]. Although the design of porous microstructure has enabled resistive pressure sensors in a wide pressure range ($0-100$ kPa) with linear response, the response/relaxation time is typically slow (on the order of several seconds) [24]. Additionally, such irregular microstructures are generally difficult to precisely tune the properties of this type of pressure sensors to meet specific requirements and the low-degree of uniformity of the irregular patterns may limit their application in high-resolution pressure sensing arrays.

Unlike the irregular one, the regular microstructures, such as pyramids [12, 13, 17, 18, 46, 47], domes [19, 20], and pillars [48], are highly uniform and tunable by the spatial arrangement of the microsctructures, and offer a designable approach to pressure sensors with desired properties. Previously, the approach of coating a very thin conductive layer on the micro-pyramidal surface (e.g., conductive polymers [18], reduced graphene oxides [17], silver nanowires [46], and CNTs [47]) has been employed in resistive pressure sensors to improve the sensitivity. However, the optimum pressure sensing range reported in these studies is generally limited in low-pressure range ($\sim$ 8 kPa [18], $\sim$ 1 kPa [17, 46, 47]). In addition, the very thin conductive layer may be vulnerable to cracks and abrasions in repeated pressure

cycles, resulting in limited mechanical robustness. To this end, the micro-pyramidal pressure sensor based on a relative complex conductive composite (CNT-P3HT-polyurethane) has been reported to achieve a larger pressure range up to $\sim$ 80 kPa.[12, 13] However, the pressure response shows severe hysteresis and even could be irrecoverable under high pressure ($\sim$ 100 kPa), which may limit their practical applicability in manipulative tasks. Thus, it remains a significant challenge to obtain sensitive and robust flexible pressure sensors with fast response time, linear response, and low hysteresis for manipulation tasks.

Herein we report a straightforward approach to highly sensitive and robust flexible pressure sensors with fast response time and low operating voltage based on conductive micropyramids made of polydimethylsiloxane/carbon nanotube (PDMS/CNT) composite. Numerical simulations are preformed to systemically examine the pressure sensing characteristics as a function of the spatial arrangement of pyramids to achieve an optimal design for manipulation tasks. We show that the pressure sensing properties of our design can be readily tuned by the spatial arrangement of pyramids and the trends can be well predicted by numerical simulations, and reveal that the pressure sensors with the 1:1 ratio between the spacing and the pyramidal base length show high sensitivity in both low- ($<$ 10 kPa, more than two-three orders current change) and medium- (10$-$100 kPa with a sensitivity of $\sim$ 0.34$-$1 kPa) pressure regimes, fast response time (48 ms at the pressure of $\sim$ 20 kPa), high mechanical robustness (more than 100 N, compared with the previous report of $\sim$ 10 N[12, 13]), low operating voltage (100 µV, compared with $>$ 10 mV in previous reports [18, 19, 24–27]) and low power consumption, along with linear response and low hysteresis in the medium-pressure regime. To demonstrate the potential application in E-skin, the optimized pressure sensor is further used to construct a wearable pressure sensing system that can convert the pressure amplitude signals into wirelessly transmittable frequency signals (spikes) with nearly linear response, closely mimicking SA-I mechanoreceptors. Taking a step further, a large-area pressure sensing array platform is developed to realize spatially resolved pressure mapping

in real time.

6.2 Result and Discussion

6.2.1 Wearable pressure sensing system.

The flexible resistive pressure sensor is constructed by laminating a thin layer of conductive micro-pyramidal film made of PDMS/CNT composite ($\sim$ 150-µm-thick) on a patterned 50-µm-thick PI film with interdigitated electrodes (Cr/Au 20/50 nm), in which the conductive micro-pyramidal film bridges the interdigitated electrodes to form a resistive network (Figure 6.1a). An applied pressure depresses the tips of the conductive micro-pyramid and increases the contact area between the micro-pyramid and the interdigitated electrodes to reduce the overall resistance. The microstructured conductive film (Figure 6.1b) is fabricated by drop casting PDMS/CNT solution (Figure 6.6a) in a prefabricated silicon mould. Raman spectrum of the comparison between the conductive film made of PDMS/CNT composite and the pure PDMS film indicates that CNTs are successfully blended in PDMS substrate (Figure 6.6b). The scanning electron microscope (SEM) image of the microstructured layer shows the micropyramids are highly uniform (Figure 6.1b), which is important for constructing large-area pressure-sensing array for spatially resolved pressure mapping. Such pressure sensor and pressure sensing array are wearable and could be conformably attached to human skin by virtue of the intrinsic flexibility of the conductive micro-pyramidal film (Figure 6.1c, d). It is noted that the conformability of the device could be further improved [49, 50] by reducing the thickness of PDMS/CNT film to $<$ 100 µm and the thickness of PI film down to several microns without fundamentally affecting the working principle of our design. The detailed fabrication processes are further discussed in method section.

The flexible resistive pressure sensors are next combined with neuron model and wireless

communication to serve as a wearable pressure sensing system to mimic SA-I mechanoreceptors for manipulation tasks. In this system, the pressure sensor transduces the pressure information into the electrical amplitude signals, which are next converted into frequency signals (spikes) by neuron model in real time. Finally, the frequency signals can be wirelessly transmitted to interface with central processors for AI robots or nerve systems for amputees. Furthermore, with the high uniformity and scalability, the pressure sensors can be configured into large-area pressure sensor array for spatially resolved pressure mapping (Figure 6.1e).

6.2.2 Evaluation of the pressure sensors.

Our resistive pressure sensor can transduce an applied pressure into the variation of resistance from the deformable conductive micro-pyramidal film made of PDMS/CNT composite, as schematically illustrated in Figure 6.1a. The resistance of the pressure sensor can be divided into two parts in series, the resistance of pyramidal microstructure that contacts with the interdigitated electrodes (Rc) and the bulk (unstructured layer) resistance (Rb) connecting the two terminals to form the current flow. The bulk resistance Rb changes little under pressure due to the less compressibility of the unstructured layer compared to the pyramidal microstructure. Indeed, the mechanical simulation confirms that the applied stress is concentrated at the pyramid tips where the most part of deformation occurs (Figure 6.2a, b). Therefore, we focus on the analysis of the resistance of pyramidal microstructure in contact with the interdigitated electrodes (Rc), which can be expressed as

$$R_c = \rho \frac{l_c}{S_c} \tag{6.1}$$

where ρ_c is the resistivity of the conductive film made of PDMS/CNT composite, l_c is the height of pyramid, S_c is the contact area between the pyramid tips and the interdigitated electrodes.

As the applied pressure increases, the pyramid height l_c decreases and result in the large increase of the contact area S_c (Figure 6.2a, b), which leads to a decrease of the contact resistance R_c based on equation (1) and an increase of current flow through the device. The simplified series resistance model is further used to evaluate and compare the current change under applied pressures in our design with conductive composite and previous design with a very thin layer of surface coating. For the microstructured resistive pressure sensors, the current flow I can be expressed as$I = V/(R_c + R_b)$, where V is the applied voltage. Since the deformation is largely occurring nearly the contact region, R_b can be approximated as a constant under different pressures. Then the current change ΔI can be described as

$$\Delta I = -\frac{V}{(R_c + R_b)^2}\Delta R_c = -\frac{V}{(1 + R_b/R_c)^2}\frac{\Delta R_c}{R_c^2} \tag{6.2}$$

It is clear from equation (2) that the absolute current change ΔI is proportional to the change in contact resistance $\Delta \mathrm{R_c}/\mathrm{R_c^2}$ and inversely proportional to the bulk/contact resistance ratio of R_b/R_c. Considering that the charge transport through the bulk volume in our conductive composite, the R_b/R_c is likely always smaller than previous design through surface coating in which charge transport through surface layer only. Therefore, our design with bulk conductive composite can lead to larger signal in current change and thus higher sensitivity (Figure 6.7a, b). The numerical simulations confirm that our micro-pyramids made of PDMS/CNT composite with bulk volume conductivity could produce much larger current flow compared with the design with a very thin layer of conductive coating on the microstructured PDMS substrate under the same pressure (Figure 6.2c, d and Figure 6.7c), and as a result, the normalized current change $\Delta \mathrm{I}/\mathrm{I_0}$ of our design made of conductive composite is larger than that of previous design under a broad strain range (0−60%), which is approximately corresponding to both the low- and medium-pressure regimes (Figure 6.7d). Moreover, it is noted that the stress concentrated at the pyramid tips reduces the distance between CNT networks within PDMS/CNT composite (Figure 6.2e, f), which could form more conductive paths, leading to a decrease of the volume resistivity ρ_c. Consequently, it

could further enhance the increase of current flow. From the above analysis, our pressure sensors based on conductive PDMS/CNT composite could provide higher sensitivity in a wide pressure range than the previous design with a very thin layer of conductive surface coating. It is noted that the above analysis could be also applicable to other microstructures, such as random roughness surface, and represents a general strategy for the design of the microstructured resistive-pressure sensors.

6.2.3 Properties of the pressure sensors.

For the pressure sensors with the micro-pyramidal microstructures, the pressure sensing properties can be readily tuned by the spatial arrangement of pyramids, such as the spacing and the pyramidal base length, which governs the compressibility of the pressure sensors. To predict the trends of the sensing performance and to guide the specific design for manipulative tasks, we have conducted mechanical simulation to evaluate the compressibility as a function of the spatial arrangement of pyramids. Figure 6.3a shows the representative simulation results with the same pyramidal base length of 12 µm and the increasing spacings of 3 µm, 6 µm, 12 µm, and 24 µm, respectively. In all scenarios, the stress and the deformation are concentrated at the tips of pyramids, confirming the pyramids dominate the compressibility. As the spacing increases, the pyramids deform more and lead to larger contact area under the same pressure (100 kPa) due to the decrease of the effective Young's modulus from the reduced pyramid density, which results in higher sensitivity. However, the ease to large deformation in the micro-pyramidal structure with larger spacing may cause the earlier saturation in large pressures.

The quantitative simulation results (Figure 6.8a) confirm that the larger spacing leads to steeper slope of the strain of pyramids, namely, higher sensitivity in the low-pressure range (< 10 kPa), but it is also more easily to reach the large strain of pyramids, which could lead

to the saturation (i.e., low sensitivity) in the medium-pressure range (10−100 kPa). Similar trends are also observed in other pyramidal base lengths (e.g., 6 µm, 24 µm, and 48 µm) (Figure 6.8b-d).

To experimentally examine the properties as a function of the spatial arrangement of pyramids and achieve optimal design for manipulation tasks, we fabricated a series of pyramidal microstructures with the pyramidal base lengths of 6 µm, 12 µm, 24 µm, and 48 µm, and the spacing/pyramidal base length ratios of 0.25:1, 0.5:1, 1:1, and 2:1, respectively (for the pyramidal base length of 6 µm, the ratio of 0.25:1 is absent due to the limitation of photolithography). Figure 6.3b shows typical SEM images with the same pyramidal base length of 12 µm and the spacings of 3 µm, 6 µm, 12 µm, and 24 µm, respectively. The pressure responses were tested in the conductive micro-pyramidal films with the area of $\sim$ 1 cm^2 laminating on the interdigitated electrodes patterned on Si wafer with 300-nm-thick SiO_2. A motorized z-stage combined with a force gauge was used to apply a specific load. As predicted by simulation, the largest spacing (24 µm, i.e., the 2:1 ratio of the spacing to the pyramidal base length) yields the steepest slope (i.e., highest sensitivity) in the low-pressure range, but reaches saturation in the medium-pressure range (Figure 6.3c). While a smaller spacing of 12 µm (i.e., the 1:1 ratio of the spacing to the pyramidal base length) can well balance the sensitivity in the low-pressure range (more than two-three orders of the current change) and the medium-pressure range (more than one order of the current change).

The sensitivity S can be calculated by $S = (\Delta I/\Delta P)/I_0$, where P is the applied pressure, I and I_0 are the current and the reference current, respectively. Here the current I at $\sim$ 10 kPa is chosen as I_0 to calculate the sensitivity in the medium-pressure range and the estimated value is about 0.34 kPa^{-1}, which is more than eight times larger than the recently reported pressure sensor for robotics4 and higher than the resistive pressure sensor (about one order of current change).12,13,24 It is noted that there is a tradeoff between the compressibility

and the hysteresis. As the spacing increases (i.e., more compressible), the hysteresis becomes larger (Figure 6.3d). The smaller spacing of 12 µm also leads to smaller hysteresis compared to the largest spacing 24 µm. Similar experimental results are also obtained in micro-pyramidal structure with other pyramidal base lengths (6 µm, 24 µm, and 48 µm) (Figure 6.9a-f), which are consistent with the compressibility predicted from the numerical simulation. Thus, the 1:1 ratio of the spacing to the pyramidal base length represents an optimal design for manipulation tasks.

Moreover, the pressure response with the optimal ratio (1:1 ratio of the spacing to the pyramidal base length) is quite linear in the medium-pressure range, which is confirmed by the high correlation coefficient (the adjusted R-square, $R^2 = 0.9983$) of linear fit (Figure 6..3e). Since the current response of the pressure sensors is dominated by the contact area between the conductive micropyramids and the electrodes resulted from the deformation of micropyramids, the linearity of pressure response is dependent on the compressibility of the micropyramidal conductive film (i.e., the spatial arrangement of micropyramids). Numerical simulations show that the compressibility increases with the increasing spacing, the structure is more easily to reach a large strain and thus non-linear response in the medium-pressure regime. Overall, the pressure sensors with the same ratio of the spacing to the pyramidal base length show similar characteristics of the compressibility, which are consistent with our experimental results. In details, the 1:1 ratio with other pyramidal base lengths of 6 µm, 24 µm, and 48 µm also shows high linearity in the medium-pressure range with high correlation coefficient (the adjusted R-square, $R^2 > 0.98$) (Figure 6.10a-f), and the structures with 2:1 ratio of the spacing to the pyramidal base length generally begin to saturate at the pressure of $\sim 40-60$ kPa. Take a step further, we examined the pressure responses with higher CNT loading of ~ 2 wt% in PDMS/CNT composite (Figure 6.11a-c), which show similar trends as that of ~ 1 wt% CNT loading (i.e., the 1:1 ratio shows high linearity ($R^2 > 0.98$) in the medium pressure range, and the 2:1 ratio turns saturated at the pressure of ~ 60 kPa),

which further confirms that the linearity depends on the spatial arrangement of micropyramids (more specifically, the ratio of the spacing to the pyramidal base length). Such clear dependence of pressure response on the ratio of spacing to base length could help to guide the design of the pressure sensors with the optimal performances in the desired pressure regime.

To explore the mechanical robustness of the pressure sensor, we performed loading-unloading cyclic test on the optimal pressure sensor. Since our pressure sensor is made by PDMS/CNT composite rather than PDMS with a very thin layer of conductive coating, little variation or degradation is observed for over 1000 cycles under a relatively large pressure of 100 kPa (Figure 6.3f). Additionally, it still works well even undertaking the force more than 100 N ($\sim$ 1000 kPa) (Figure 6.12), which is important for mechanical robustness in practical applications.8 Moreover, our pressure sensors can maintain the high linearity and the pressure responses show high uniformity even after 2000 cycles under the pressure of $>$ 100 kPa, which further confirms their mechanical robustness (Figure 6.13).

Lower power consumption and/or lower operating voltage is critical for the practical applications of the pressure sensors [2, 13, 18, 19, 33]. To explore the potential of our pressure sensors for lower voltage operation, we tested their responses under the applied pressure of $\sim$ 20 kPa at the operating voltages of 1 V, 0.1 V, 0.01 V, 0.001 V, 0.0001 V, and 0.00001 V, respectively (Figure 6.14a-f). It can be observed that our pressure sensors can clearly and stably detect the pressure even at the low operating voltage of 0.0001 V (100 µV, compared with $>$ 10 mV in previous reports [18, 19, 24–27]), and thus leads to a low power consumption of $\sim$ 10 nW, which is comparable to the transistor based pressure sensors ($\sim$ 9 pW$-$270 nW).33 Importantly, such low operation voltage makes it possible to power these pressure sensors with small portable energy-harvesting devices [38–40], which could enable the construction of self-powered and wearable pressure sensing systems. More-

over, we also examined the response time/relaxation time, which shows a rapid response of $\sim$ 48 ms under the pressure of $\sim$ 20 kPa (Figure 6.60a, b). Together, our studies show that the optimal pressure sensors can deliver a combination of high sensitivity in both low- and medium-pressure regimes, fast response time, high mechanical robustness, low operating voltage and low power consumption, along with linear response and low hysteresis in the medium-pressure regime for manipulation tasks. A detailed comparison with other resistive pressure sensors with the existing state-of-art is provided in Figure 6.20 and Figure 6.21.

6.2.4 Frequency response of the pressure sensing system.

Compared with electrical amplitude-modulated signals, frequency-modulated signals (spikes) provide a more power-efficient and robust approach for signal transmission and are also more desirable for interfacing with biological nerve systems [3, 5, 12, 13]. Though the conversion from the voltage amplitude to frequency signals has been achieved by the organic ring oscillator [12, 13], it remains a challenge to produce the spikes with biological plausibility and reduce the size of pixels to mimic SA-I mechanoreceptor by the artificial nerve system. To this end, the mathematic (Izhikevich) neuron model, which provides an efficient and practical approach to generate spike signals [51], is selected for the conversion. By integrating the optimal pressure sensor (the spacing of 6 µm and the pyramidal base length of 6 µm) with the Izhikevich neuron model coded in a chip (see method section for details), we successfully converted the applied pressure into spikes (Figure 6.4a) in real time (Movie S1), which is desirable for the sensory feedback systems of amputees and AI robotics.

It is apparent that the frequency of the spikes increases as the pressure stimuli enhances, with the frequency of the spikes ranging from 10 Hz to 120 Hz in the medium-pressure range (10−100 kPa), which is similar to that of SA-I mechanoreceptors. Additionally, the frequency response shows a good linear response to the applied pressure in the 10−60 kPa

regime (Figure 6.4b), which is beneficial for data processing. We note that the non-linearity develops beyond 60 kPa, which is mainly due to the non-linear I-V conversion from the read-out circuit of the voltage divider (Note S1) and it could be further improved by choosing a more linear I-V converter, such as transimpedance amplifier. Furthermore, an interesting example of holding a plastic cup was performed to demonstrate that the wearable pressure sensing system could be applied for a routine manipulation task (Figure 6.4c, d). The resulted frequency signal corresponds to $\sim$ 13 kPa, a reasonable value for such kind of manipulation tasks.

Wireless communication is an efficient way to reduce the wire complexity during the signal transmission.1 Moreover, through wireless communication, the pressure information for manipulation tasks can be wirelessly transmitted to portable intermediary devices such as mobile phones and personal computers in real time and uploaded to clouds, and parsed with big data and AI technology to enable a more intelligent pressure sensing system. Thus, it is desirable to achieve wireless transmission for the pressure sensing system. To this end, we added Bluetooth function to the pressure sensing system and another chip functionalized with Bluetooth is served as the signal receptor, which drives a green light emitting diode (LED) to demonstrate the wireless transmission of the signals and the activation of the actuators (Figure 6.61). When the pressure is applied by our finger, the green LED starts to blink, and the blinking frequency increases with the increase of the pressure, indicating the spike signals generated by our pressure sensing system is successfully transmitted by wireless communication. When we enhance the pressure to a specific value, the green LED will continuously glow, reaching a blinking frequency that is hard to be distinguished by naked eyes (Movie S2).

6.2.5 Spatially resolved pressure mapping.

Our natural skin can obtain the shape information of objects, even the details of structures by the tactile sensation from the array of mechanoreceptors. To mimic the function for artificial skin, it is necessary to create pressure sensing array for obtaining the spatial distribution of pressure. As a demonstration, a 4 × 4 pixel array for spatially resolved pressure mapping is fabricated with the total sensitive area of ∼ 4 cm^2 and the each pixel area of ∼ 4 mm^2. The pressure sensing array is made with 16 pieces (∼ 2 × 2 mm^2) of the optimal conductive micro-pyramidal films (the spacing of 6 μm and the pyramidal base length of 6 μm) attached onto the patterned PI film with an array of interdigitated electrodes, in which each interdigitated electrode is bonded with a contact pad separately to minimize the cross-talk effect (Figure 6.62a-d) and shares a common ground to reduce wire complexity. A thin layer of PDMS with the area of ∼ 4 cm^2 is laminated on the device to hold the position of each pixel when performing the test. For the spatially resolved pressure mapping experiments, the device of pressure sensing array is serially connected with a 16-bits multiplexer and controlled by a chip, serving as a platform for pressure mapping (the details are shown in method section). The letters "I" and "T" made by ∼ 2-mm-thick PDMS are placed on pixels in the array (Figure 6.5a, d). The force is applied by our finger and the data for pressure mapping is collected by the chip. Figure 6.5b, c and 5e, f clearly shows that the shape of the letters can be revealed by the pressure sensing array. The pixels under press (Figure 6.5c, f) are brighter than that under gentle touch (Figure 6.5b, e), which indicates the array system can also identify different pressures. Such platform of pressure sensing array can readily interact with computers, visualizing the images of the letters in real time (Movie S3), which contributes to realize the real spatial recognition with big data and AI techniques. Though we currently use the 4 × 4 pixel array as a proof-of-concept demonstration, the fundamental operation principle could be readily extended to much larger arrays particularly considering the high uniformity of micropyramids and the scalable fabrication process.

6.3 Conclusions

We have reported a highly sensitive and robust flexible pressure sensor based on conductive micropyramids made of PDMS/CNT composite. We showed that pressure sensing properties of the device can be readily tuned by the spatial arrangement of micropyramids, to enable the rational design of pressure sensors with a combination of high sensitivity in both low- (< 10 kPa) and medium- ($10-100$ kPa) pressure regime, fast response time, high mechanical robustness, low operating voltage and low power consumption, linear response and low hysteresis in the medium-pressure regime. The resulting pressure sensors can be further configured to mimic SA-I mechanoreceptors, converting the pressure amplitude to frequency signals with nearly linear response. With high uniformity and scalability, our design can be further extended to large-area pressure sensing array for spatially resolved pressure mapping, showing considerable potential for human-like object manipulation in E-skin. In addition, our robust conductive micropyramids could be readily integrated into the capacitive-, transistor- and triboelectric-based pressure sensors to obtain the highly robust pressure sensors.

6.4 Methods

6.4.1 Microstructured PDMS/CNT film fabrication.

10 mg of Multi-walled carbon nanotubes (MWCNTs, $3-6$ µm length, $\geq 98\%$ from Sigma Aldrich) were dispersed in isopropanol (IPA) with a weight ratio of CNT:IPA = 1:200 by magneton stirring (speed, 1000 rad/min) for 5 min and sonicating for 30 min in bath sonicator (Branson 2510) twice. 0.83 g of PDMS elastomer (Sylgard 184, Dow Corning) was dispersed in ~ 8 g of hexane by magneton stirring for 30 min. The CNT solution was then mixed with the PDMS solution by magneton stirring, sonicating, and magneton stirring for 5 min, respectively. Finally, 0.17 g of curing agent was added in the PDMS/CNT solution

and mixed by magneton stirring for 30 min to obtain the final PDMS/CNT solution with the CNT loading of $\sim$ 1wt% (Figure 6.6a).
The micro-pyramidal film made of PDMS/CNT composite (Figure 6.6b) was prepared by drop casting the PDMS/CNT solution in a silicon (Si) mould with pyramid microstructure three times. Degas in vacuum desiccator for 30 min after the 1st and 2nd casting, respectively, 60 min after the 3rd casting to make sure to remove the solvents, followed by annealing at about 120 °C for 1 h in oven to cure the composite.

The Si mould, made from $<100>$ Si wafer with $\sim$ 60-nm-thick Si_3N_4, was patterned by standard photolithography and etched by Reactive Ion Etching (RIE, Technics Micro-RIE Series 800). The remaining Si_3N_4 served as a mask for potassium hydroxide (KOH) etching, followed by spin coating (speed: 4500 rad/min, time: 40s) a layer of fluoropolymer solution (DAIKIN industries, LTD. Chemical R&D center) and baking at 150 °C for 30 min to facilitate the release of the PDMS/CNT film.

We should note that the fabrication of pyramidal microstructure is a rather straightforward process. The silicon mold can be readily fabricated by a single step photolithography and self-limited etching process. The resulted silicon mold can be repeatedly used for mass production of micropyramidal structures via a simple cast and curing process. The introduction of PDMS/CNT composite further simplifies the process to directly produce conductive micro-pyramids without additional step of deposition or coating process to form surface conductive layer, and at the same time improves the robustness of the structure when compared with those coating a thin surface conductive layer that is prone to crack under repeated compression.

6.4.2 Device Fabrication.

The flexible pressure sensor on fingertip was assembled by laminating the micro-pyramidal film made of PDMS/CNT composite (area: ~ 1 cm^2) on a 50-µm-thick polyimide (PI, Kapton) film with interdigitated electrodes (width: 100 µm and spacing: 100 µm). The PI film was first rinsed with acetone, IPA, and deionized (DI) water, respectively, then patterned with interdigitated electrodes by standard photolithography and deposited by electron beam evaporation (Cr/Au, 20 nm/50 nm), followed by lift off process. Cr/Au was used here due to the good adhesion, which could improve the robustness of the electrodes. For the demonstration of frequency response of holding the cup, medical tape was used to adhere the sensor to fingertip. For the flexible 4×4 pressure sensor array (area: ~ 4 cm^2) on palm, the as prepared 16 pieces of the conductive micro-pyramidal film with the area $\sim 2 \times 2$ mm^2 were attached onto interdigitated electrodes (width: 50 µm and spacing: 50 µm) array on PI substrate. A thin PDMS film ($\sim$ 100 µm) was laminated on the PDMS/CNT film to hold the pixels for the pressure mapping experiments.

6.4.3 Device Characterization.

SEM images of the micropyramids were taken by FEI NOVA NANOSEM 230. Raman spectrums were carried out by Raman spectroscopy (Horiba, 488-nm laser wavelength). The force test system of Mark-10 including a force gauge (M7-10) and a motorized test (ESM303) stand controlled by computer was taken to apply the loads. For the pressure response tests, the current was recorded by Agilent B2902A under ambient conditions operating the voltage of 1 V. For the measurement of frequency response, the pressure sensor was sourced by the chip of Arduino Uno and a simplest readout circuit of voltage divider was applied to convert current to voltage as the input for the chip. The converted voltage V_r can be expressed by $V_r = V_C R_r/(R_r + R_s)$, where V_C is the voltage provided by the chip, R_r and R_s are the

reference resistance and the resistance of the pressure sensor, respectively. As we can see from the equation, the reference resistance R_r could influence the voltage conversion, especially when R_r is comparable to R_s. This effect can be improved by the readout circuit of the more linear I-V converter (transimpedance amplifier), which provides linear conversion between current and voltage. For the Izhikevich neuron model, the details can be expressed as

$$\frac{\mathrm{d}\upsilon}{\mathrm{d}t} = 0.04\upsilon^2 + 5\upsilon + 140 - u + V/R_{ref} \frac{\mathrm{d}u}{\mathrm{d}t} = a(b\upsilon - u) \text{if}(\upsilon = 30\text{mV}), \text{then} \upsilon \leftarrow c, u \leftarrow u + d \quad (6.3)$$

the parameters used for the spikes are as follows: a = 0.02, b = 0.2, c = –65 mV, d = 8, and R_{ref} = 2. For the wireless communication system, two Arduino chips paired with two Bluetooth (HC-05) were used for the demonstration. Chip #1 (Arduino Mega) with Bluetooth #1 and chip #2 (Arduino Uno) with Bluetooth #2 are served as spike-signal sender and receptor, respectively. For the pressure sensing array, the chip of Arduino Mega with a 16-bit multiplexer from SparkFun Electronics was used to control the array of the pressure sensor and the voltage divider was applied to the readout circuit. Processing software was preformed to visualize the spatial distribution of the pressure information.

6.4.4 Simulation.

Finite-element method was used for both mechanical and electric simulations. In mechanical simulation, the PDMS/CNT composite was modelled by linear elastic material with Poisson's ratio of 0.499 and Young's modulus of 3.16 MPa, which is estimated by experimental stress-strain curve with the tensile rate of 10mm/min (Figure 6.63). The pressure was applied on the surface of PDMS/CNT unstructured layer and the counter object (PI) was fixed. In electrical simulation, the conductivity of 3.49 S/m of the PDMS/CNT composite was estimated by four-terminal method. To obtain the relation between strain and contact area of the pyramids, we consider the volume of the pyramid does not change at different strains since the Poisson's ratio of PDMS is about 0.5. The equation can be expressed as

$$\frac{1}{3}\frac{(l_a^2 + l_b^2 + l_a l_b)}{h} = \frac{1}{3}\frac{(l_a{}'^2 + l_b^2 + l_a{}' l_b)}{h'} \tag{6.4}$$

where l_a and $l_a{}'$ are the initial tip length and the tip length corresponding to a specific strain of pyramids, respectively; h and h' are the initial height and the height corresponding to a specific strain of pyramids, respectively; l_b is the pyramidal base length of pyramids. Based on equation (4), we can derive the expression of the tip length corresponding to specific strain $l_a{}'$ as follows:

$$l_a{}' = \frac{-l_b + \sqrt{-3l_b^2 + 4\left(\frac{h'}{h}\right)(l_a^2 + l_b^2 + l_a l_b)}}{2} \tag{6.5}$$

and the contact area corresponding to the specific strain is obtained by the square of $l_a{}'$.

6.5 Note S1

Typically, the circuit of voltage divider converts the current signal to voltage signal by serial connection with a reference resistance, and the equation can be expressed as

$$V_{out} = \frac{R_r}{R_r + R_s} V_{CC} \tag{6.6}$$

where V_{out} and V_{CC} are the output voltage and supply voltage of the circuit, respectively. R_r and Rs are the reference resistance and the pressure sensor resistance, respectively. The circuit model of voltage divider is shown in Figure 6.64a, and to clearly show the effects of the readout circuit to the linearity of the frequency response, we have carried out numerical simulation for analysis, considering that the circuit of voltage divider converts the current ($10^{-3} - 10^{-2}$ A) to the voltage at the supply voltage of 1 V with different reference resistances of 100 Ω , 200 Ω , 400 Ω , and 800 Ω , respectively (Figure 6.64b). It can be observed that the conversion of the current of pressure sensors to the output voltage by voltage divider is generally not linear and the slope of the conversion curve decreases as the current of the

pressure sensors increases (i.e., pressure increases), which leads to the non-linearity of the frequency response of the pressure beyond 60 kPa. It is noted that as the reference resistance R_r decreases the conversion curve turns to linear, but the measurement range becomes narrow. In general, mid-point in the range of resistances of pressure sensors is suggested to balance the linearity and measurement range of the conversion.

6.6 Figures and Legends

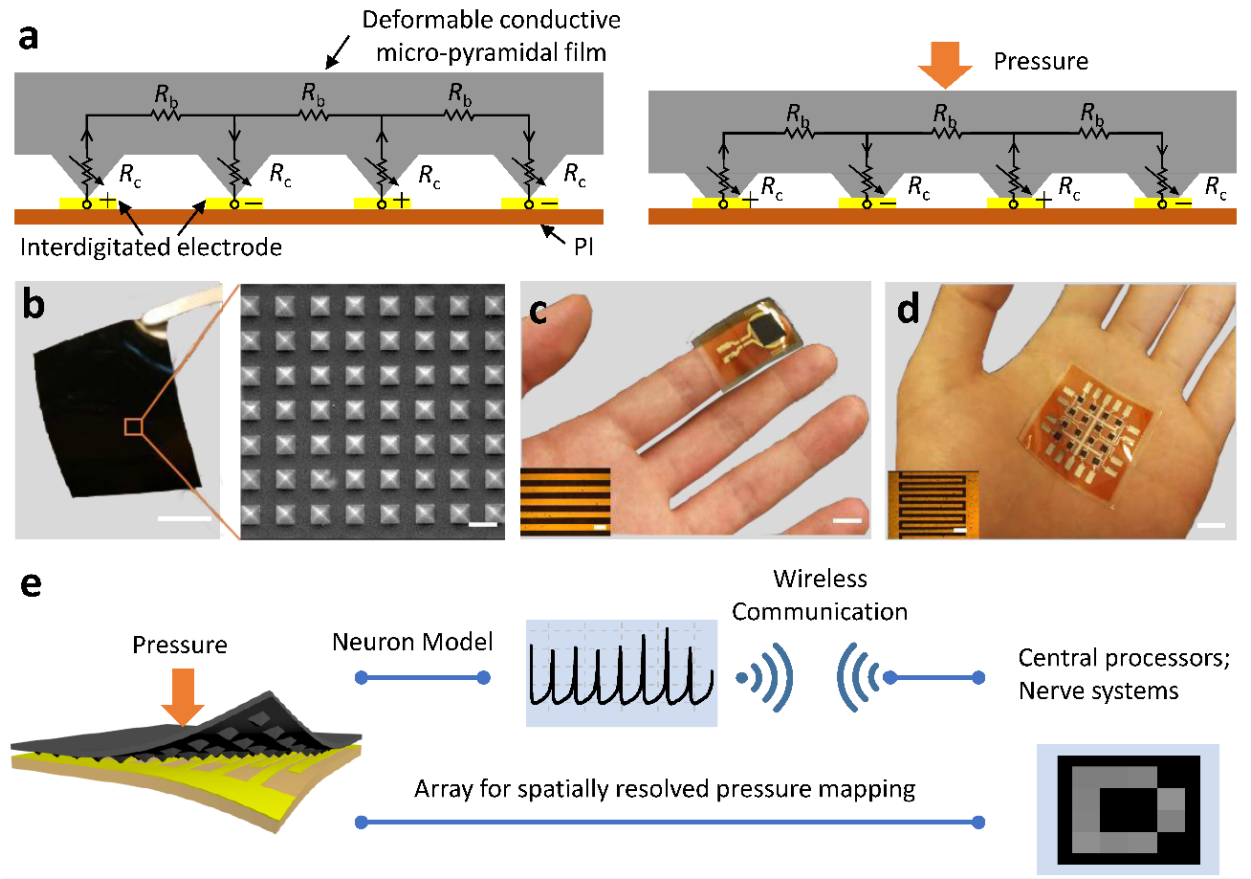

Figure 6.1: Wearable pressure sensing system. (a) Schematic of the working mechanism of the resistive pressure sensor with compressible conductive micro-pyramidal array bridging a pair of interdigitated electrodes without pressure (left) and with pressure (right), in which an applied pressure deforms the micropyramids and change the contact area and thus the resistance of the device to produce a detectable signal. (b) Photograph of the conductive micro-pyramidal film made of PDMS/CNT composite (left). Scale bar, 1 cm. SEM image of the microstructured layer (right). Scale bar, 10 µm. (c) Photograph of wearable pressure sensor on fingertip. The pressure sensor is constructed by laminating the conductive micro-pyramidal film made of PDMS/CNT composite on patterned PI film with interdigitated electrodes. Scale bar, 1 cm. Inset: optical microscope image of interdigitated electrodes.

Scale bar, 100 μm. (d) Photograph of wearable pressure sensor array with 4 × 4 pixels on palm. Scale bar 1 cm. Inset: optical microscope image of interdigitated electrodes. Scale bar, 100 μm. (e) Schematic of wearable pressure sensing system. The pressure sensor transduces pressure information into electrical amplitude signals, then the amplitude signals can be converted into the frequency signals by neuron model in real time, finally the frequency signals are wirelessly transmitted to interface with central processors for AI robots or nerve systems for amputees (top); The pressure sensor array can realize spatially resolved pressure mapping in real time (bottom).

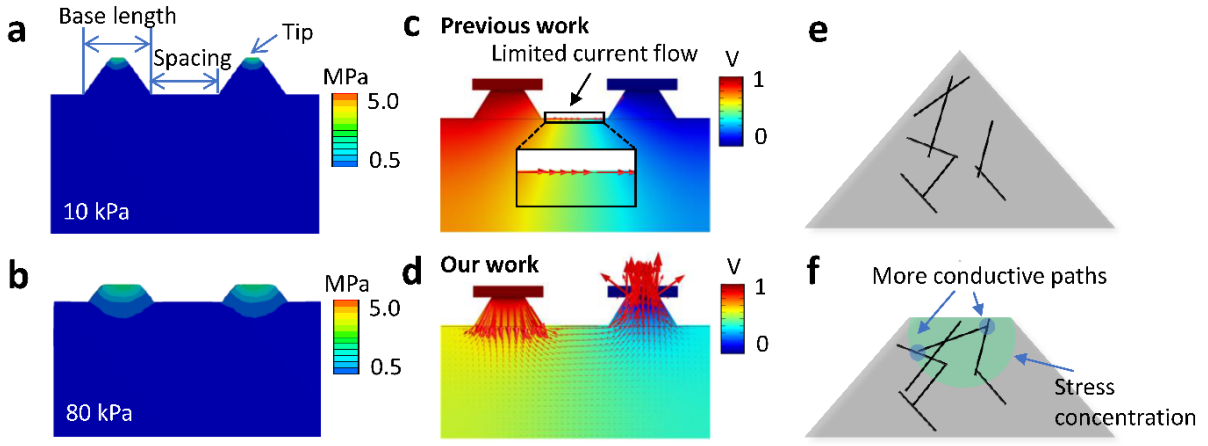

Figure 6.2: Evaluation of the resistive pressure sensors based on conductive micropyramids made of PDMS/CNT composite. Mechanical simulation of cross-sectional views of deformation and stress intensity distribution of the conductive micro-pyramidal film made of PDMS/CNT composite with a spacing of 6 µm and a pyramidal base length of 6 µm under different pressures: (a) 10 kPa and (b) 80 kPa, respectively. Simulation of cross-sectional views of voltage and current density distribution (marked with arrows) of (c) previous work (coating a 100-nm-thick conductive layer, top) and (d) our work (PDMS/CNT composite, bottom) with a spacing of 6 µm and a pyramidal base length of 6 µm at the strain $\sim$ 40% of the pyramids. Schematic of the conductive micro-pyramids (e) without pressure and (f) with pressure to show that the stress concentrated at the pyramid tips reduces the CNTs distance, resulting in more conductive paths.

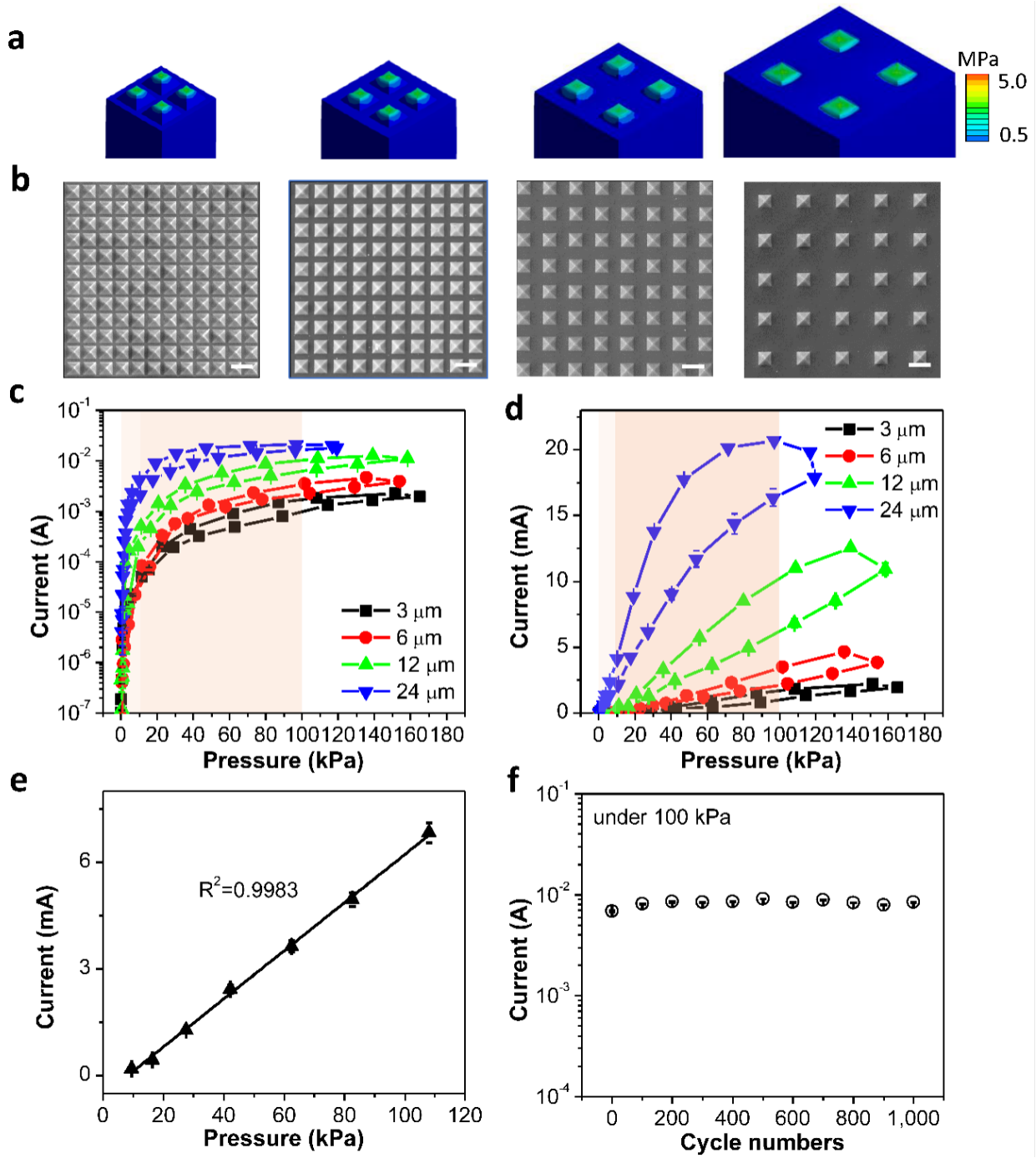

Figure 6.3: Properties of the resistive pressure sensors. (a) Mechanical simulation of deformation and stress intensity distribution of the conductive micro-pyramidal films with the same pyramidal base length of 12 μm and the spacings of 3 μm, 6 μm, 12 μm, and 24 μm

under 100 kPa, respectively. (b) SEM images of the micropyramids in the microstructured PDMS/CNT films with the same pyramidal base length of 12 µm and the spacings of 3 µm, 6 µm, 12 µm, and 24 µm, respectively. Scale bar, 20 µm. (c) Log plot and (d) linear plot of pressure responses of the resistive pressure sensors. (e) Linear fit of pressure response of the optimal pressure sensor with the spacing of 12 µm and the pyramidal base length of 12 µm in medium-pressure range. (f) Stability test of the optimal pressure sensor(over 1000 cycles) under a large pressure of 100 kPa.

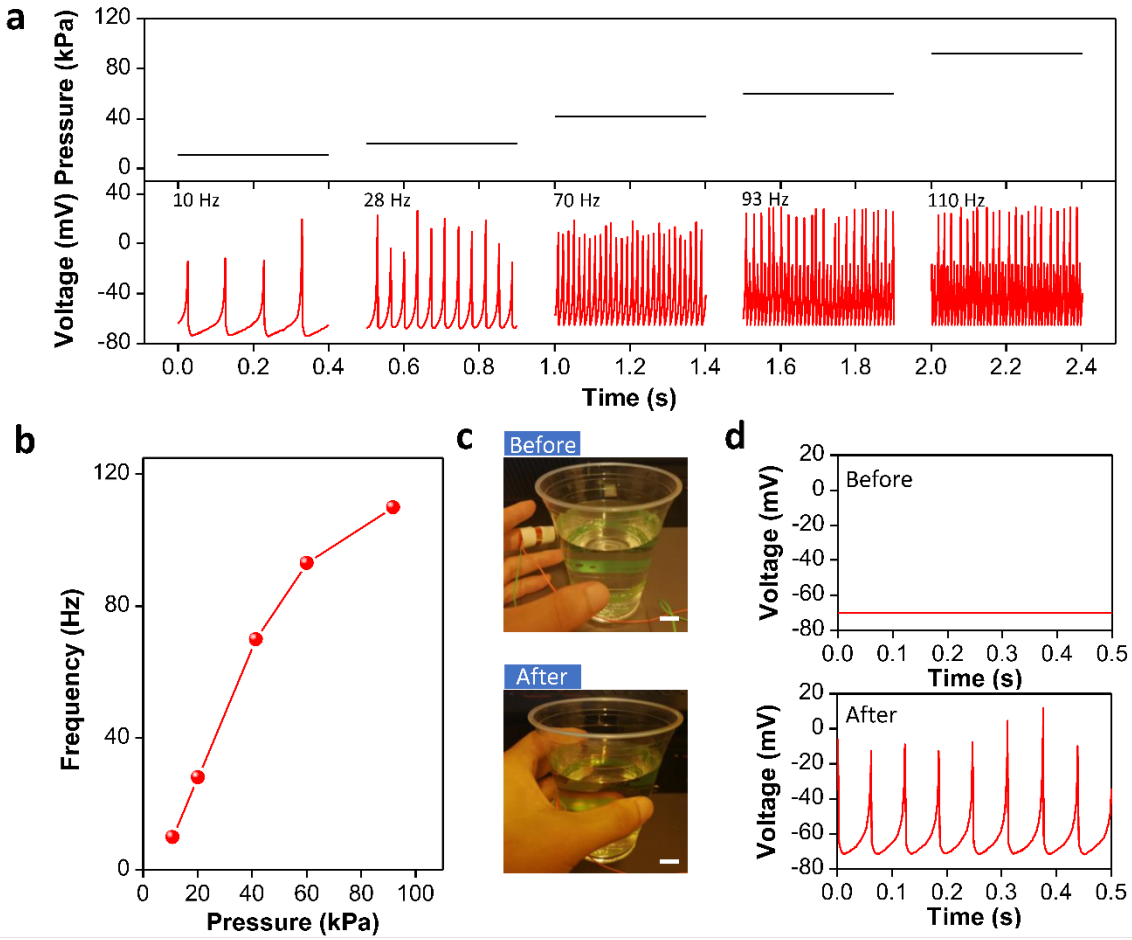

Figure 6.4: Frequency response of the pressure sensing system. (a) Frequency signals (spikes) under different pressures. (b) Frequency response as a function of pressure. (c) Photographs of before (top) and after (bottom) holding a plastic cup filled with water. Scale bar, 1 cm. (d) Frequency signals (spikes) of before (top) and after (bottom) holding the plastic cup, respectively. Before holding the cup, there is no signal; after holding the cup, the system generates the spikes with a frequency of $\sim$ 15 Hz, corresponding to a pressure of $\sim$ 13 kPa.

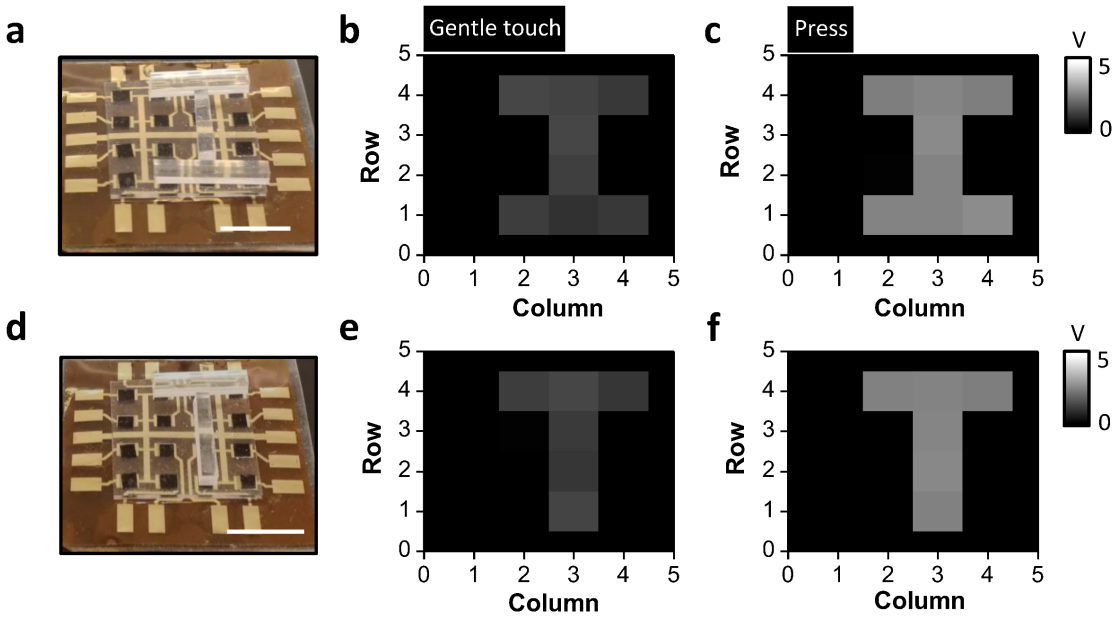

Figure 6.5: Pressure sensing array for spatially resolved pressure mapping. (a) Photograph of the letter "I" made by PDMS on the 4 × 4 pixel array for spatially resolved pressure mapping. Scale bar, 1 cm. (b) Pressure mapping of the letter "I" under gentle touch and (c) under press. (d) Photograph of the letter "T" made by PDMS on the 4 × 4 pixel array for spatially resolved pressure mapping. Scale bar, 1 cm. (e) Pressure mapping of the letter "T" under gentle touch and (f) under press.

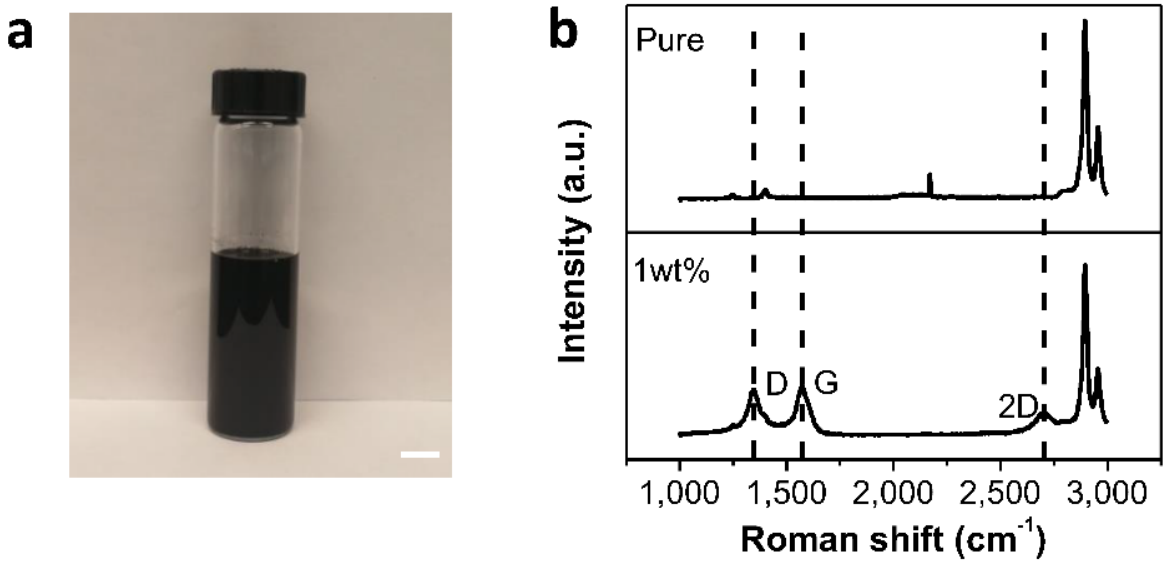

Figure 6.6: Preparation for micro-pyramidal film made of PDMS/CNT composite. (a) Photograph of PDMS/CNT solution. Scale bar, 1 cm. (b) Raman spectrums of pure PDMS film and conductive film made of PDMS/CNT composite with 1wt% CNT content. Three additional peaks D, G, and 2D (1346 cm^{-1}, 1570 cm^{-1}, and 2699 cm^{-1}) can be observed in the conductive film made of PDMS/CNT composite compared to the pure PDMS film.

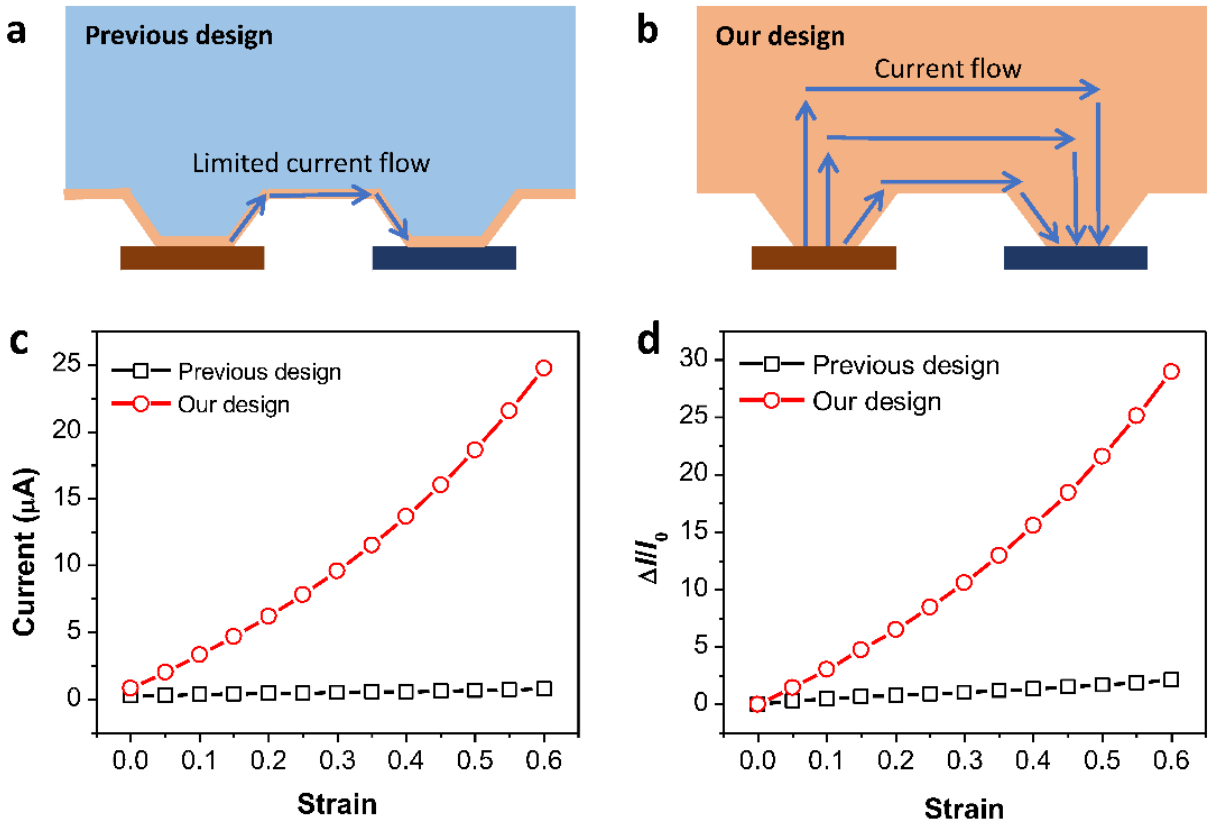

Figure 6.7: Comparison of previous work (coating a 100-nm-thick conductive layer) and our work (PDMS/CNT composite) by electric simulation. Schematic to show the working mechanism of (a) previous design and (b) our design. Considering that the charge transport through the bulk volume in our conductive composite, the ratio of bulk/contact resistance is likely always smaller than previous design through surface coating in which charge transport through surface layer only. Therefore, our design with bulk conductive composite can lead to larger signal in current change and thus higher sensitivity and thus leads to higher sensitivity. (c) The current flow versus the strain of pyramids. (d) Normalized current change versus the strain of pyramids (0−60%), roughly corresponding to both low- (< 10 kPa) and medium- (10−100 kPa) pressure range.

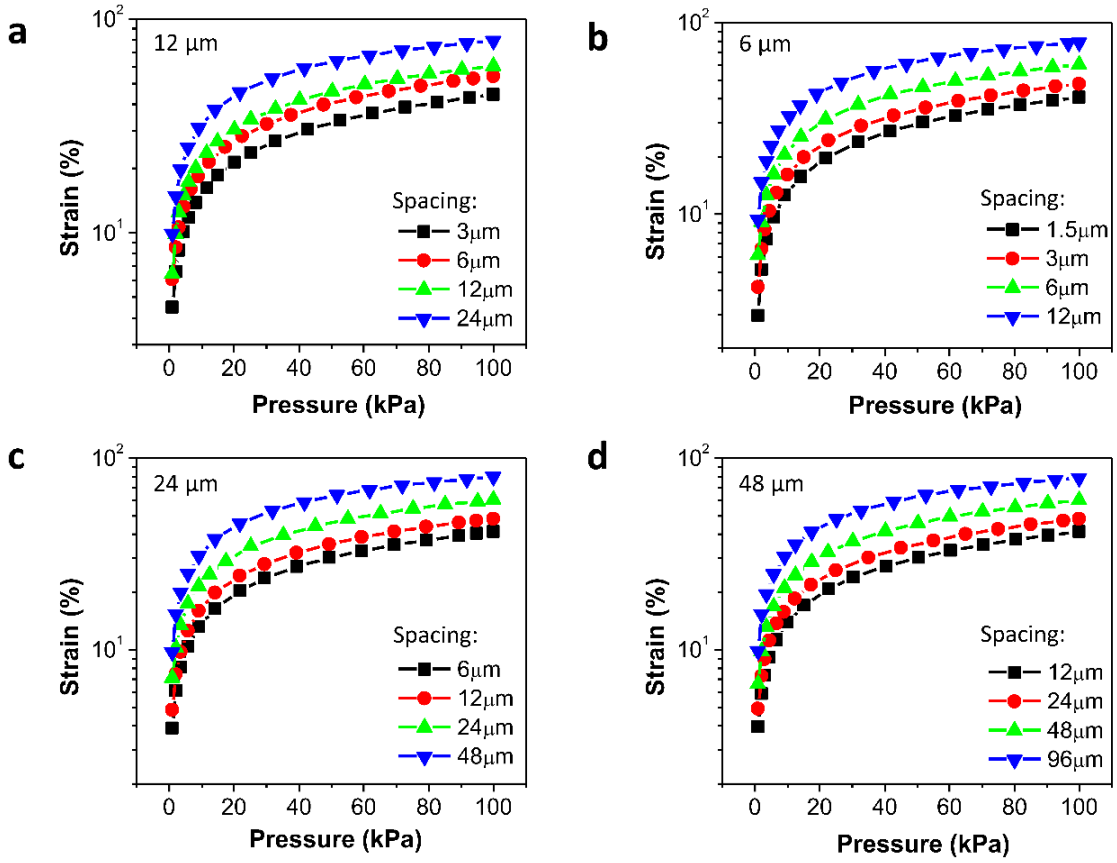

Figure 6.8: Mechanical simulations of the strain of the pyramids versus pressure with different spacings and pyramidal base lengths: (a) the same pyramidal base length of 12 µm and the spacings of 3 µm, 6 µm, 12 µm, and 24 µm, respectively; (b) the same pyramidal base length of 6 µm and the spacings of 1.5 µm, 3 µm, 6 µm, and 12 µm, respectively; (c) the same pyramidal base length of 24 µm and the spacings of 6 µm, 12 µm, 24 µm, and 48 µm, respectively; (d) the same pyramidal base length of 48 µm and the spacings of 12 µm, 24 µm, 48 µm, and 96 µm, respectively.

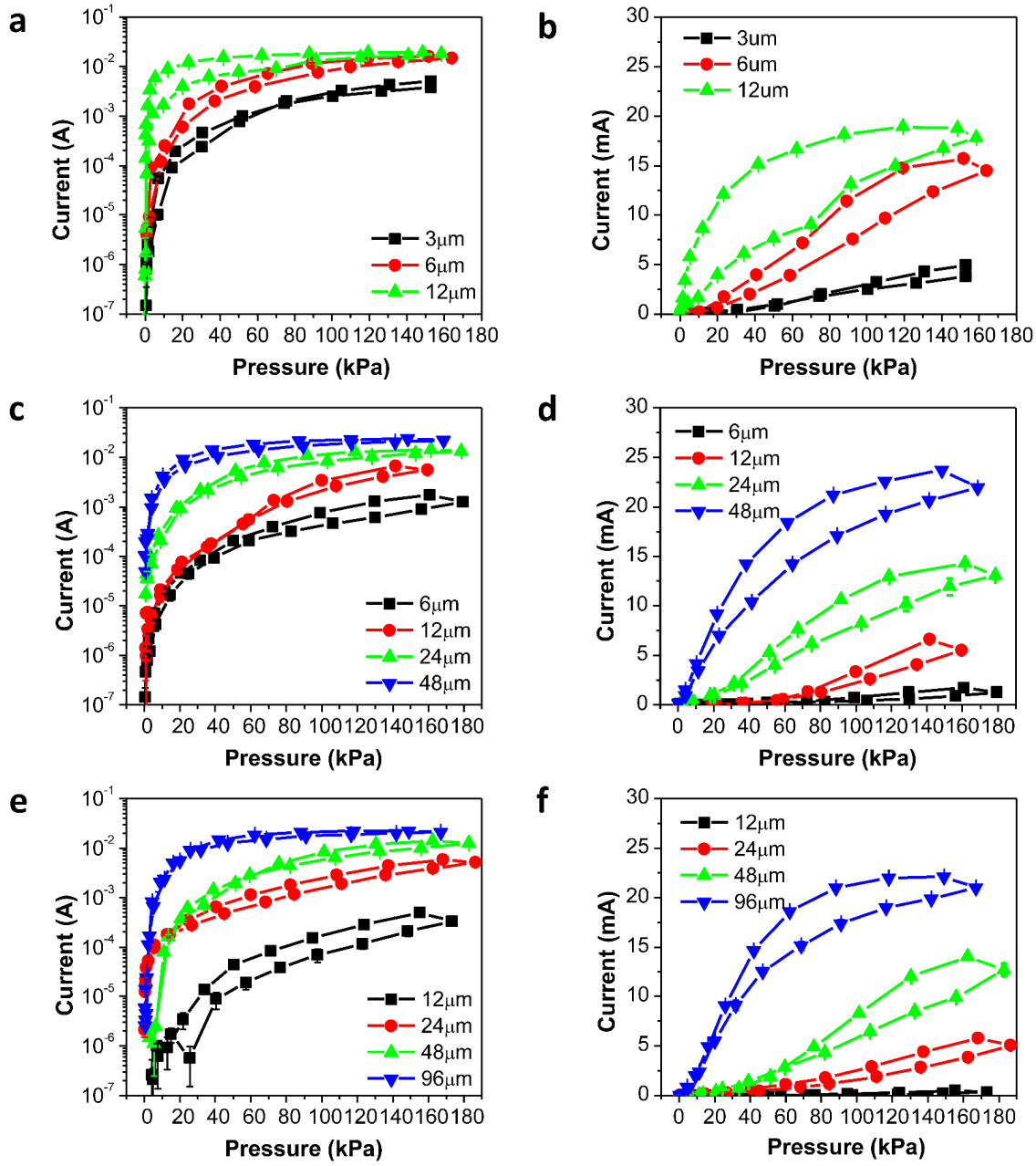

Figure 6.9: Experimental results of pressure responses of the pressure sensors. (a) Log plot and (b) linear plot of pressure responses from the conductive micro-pyramidal films made of PDMS/CNT composite with the same pyramidal base length of 6 µm and the spacings of 1.5 µm, 3 µm, 6 µm, and 12 µm, respectively. (c) Log plot and (d) linear plot of pressure

responses from the conductive micro-pyramidal films made of PDMS/CNT composite with the same pyramidal base length of 24 µm and the spacings of 6 µm, 12 µm, 24 µm, and 48 µm, respectively. (e) Log plot and (f) linear plot of pressure responses of from the conductive micro-pyramidal films made of PDMS/CNT composite with the same pyramidal base length of 48 µm and the spacings of 12 µm, 24 µm, 48 µm, and 96 µm, respectively.

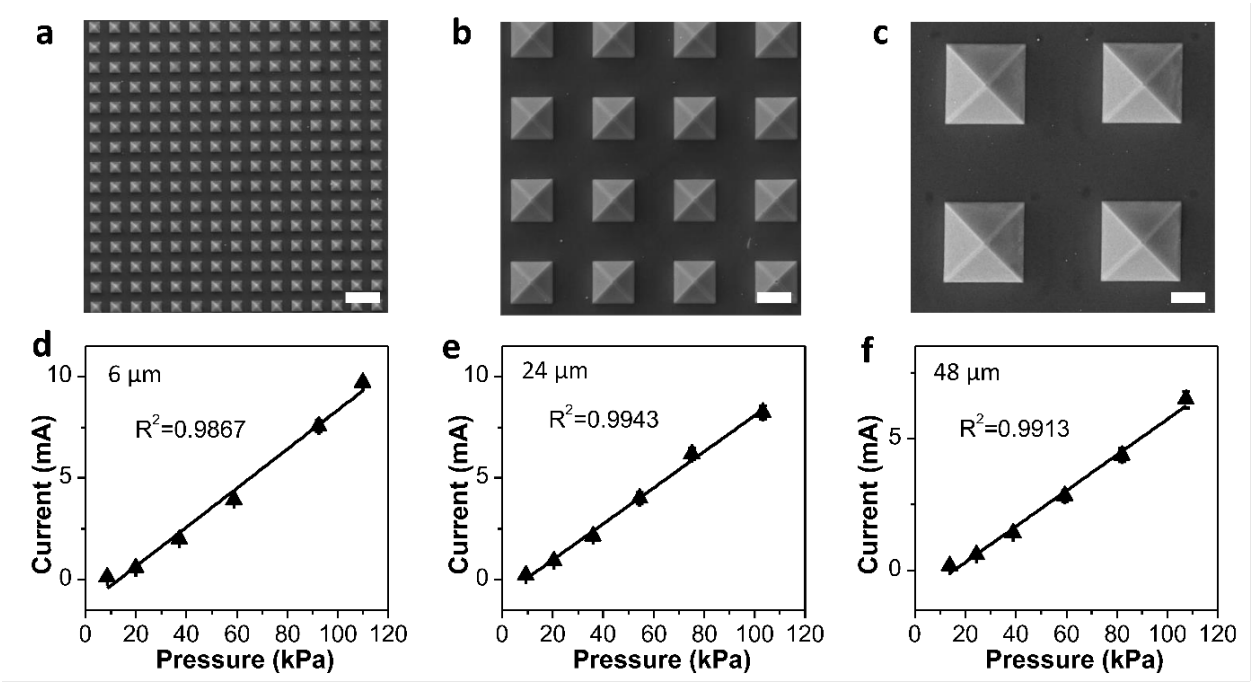

Figure 6.10: Linear pressure response of the pressure sensors with the 1:1 ratio. SEM images of the pressure sensors with the same ratio of the pyramidal base length to the spacing and different base lengths of (a) 6 µm, (b) 24 µm, and (c) 48 µm, respectively. Scale bar, 20 µm. Pressure response and linear fit of the pressure sensors with the same ratio of the pyramidal base length to the spacing and different base lengths of (d) 6 µm, (e) 24 µm, and (f) 48 µm, respectively.

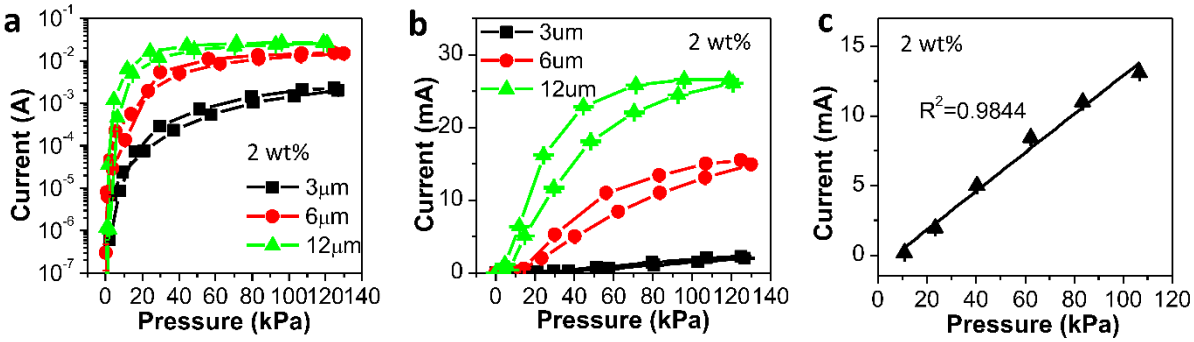

Figure 6.11: (a) Log plot and (b) linear plot of pressure responses of the resistive pressure sensors ($\sim$ 2wt% CNT loading) with the same pyramidal base length of 6 µm and the spacings of 3 µm, 6 µm, and 12 µm, respectively. (c) Linear fit of pressure response of the optimal pressure sensor ($\sim$ 2wt% CNT loading) with the pyramidal base length of 6 µm and the spacing of 6 µm in medium-pressure range.

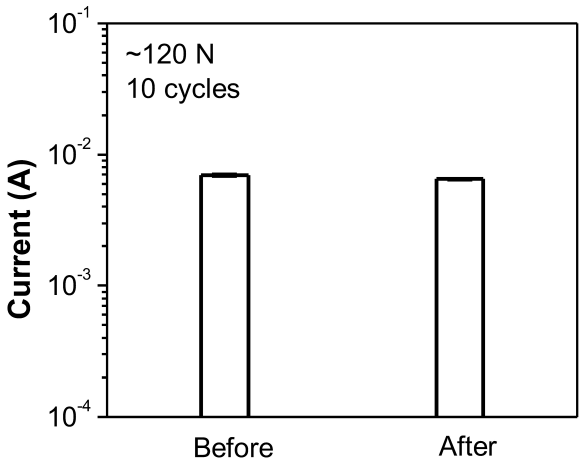

Figure 6.12: Mechanical robustness of the flexible pressure sensor. Pressure response under 100 kPa before and after a large applied force of $\sim$ 120 N (1200 kPa) for 10 cycles.

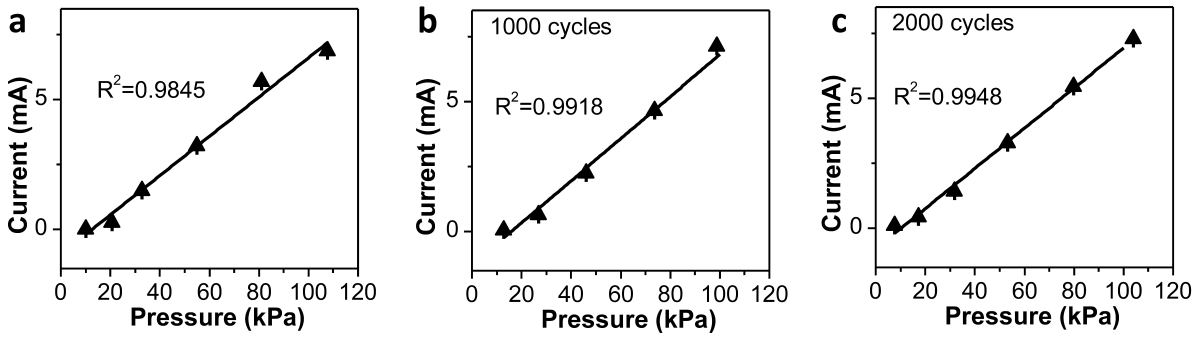

Figure 6.13: Linear pressure response of the pressure sensors with the pyramidal base length of 6 µm and the spacing of 6 µm. (a) The pressure response before cycles. (b) The pressure response after 1000 cycles. (c) The pressure response after 2000 cycles.

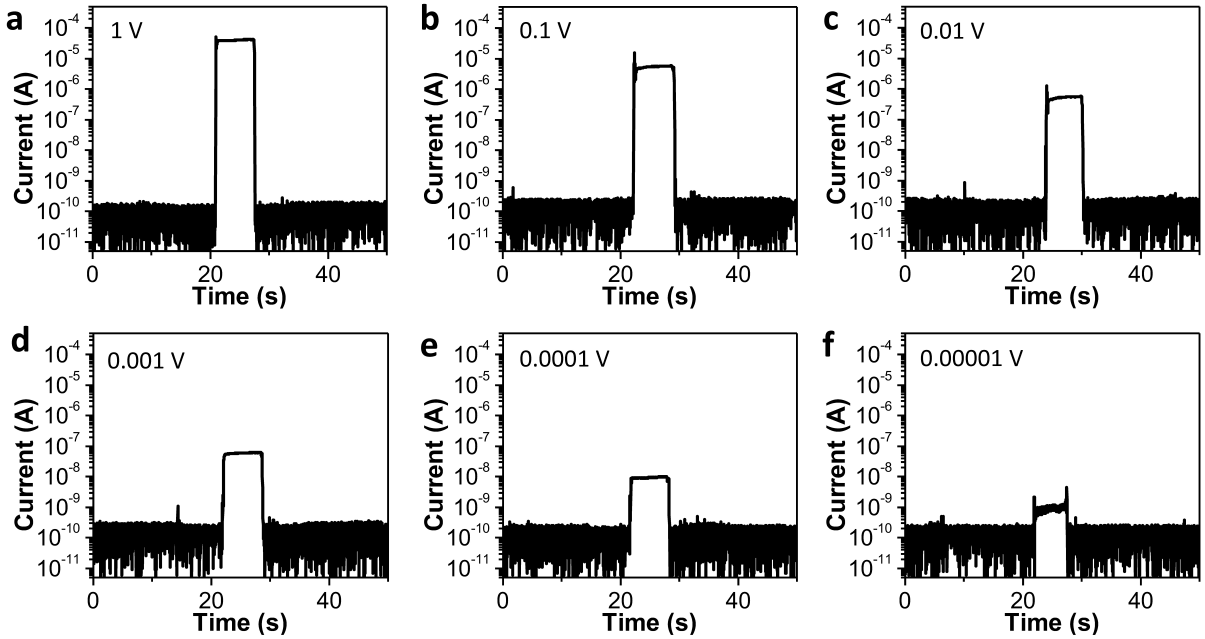

Figure 6.14: Pressure responses of the pressure sensor with the pyramidal base length of 6 µm and spacing of 6 µm under the applied pressure of $\sim$ 20 kPa at the operating voltages of (a) 1 V, (b) 0.1 V, (c) 0.01 V, (d) 0.001 V, (e) 0.0001 V, and (f) 0.00001 V, respectively.

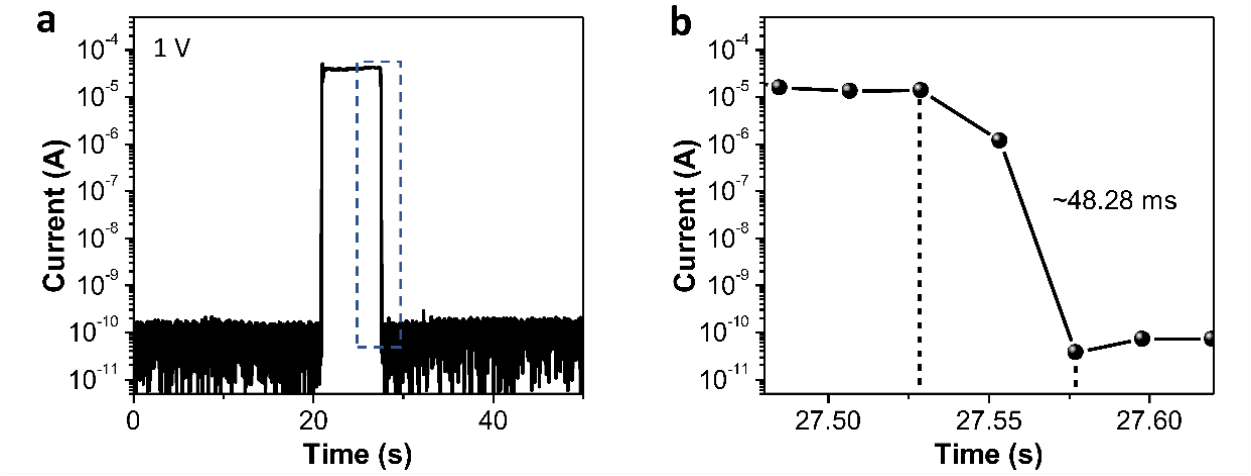

Figure 6.15: Response time/relaxation time of our pressure sensors. (a) Pressure response of the pressure sensor with the pyramidal base length of 6 µm and spacing of 6 µm under the applied pressure of $\sim$ 20 kPa at the operating voltage of 1 V. (b) Enlarged image from a to show the response time of the pressure sensor.

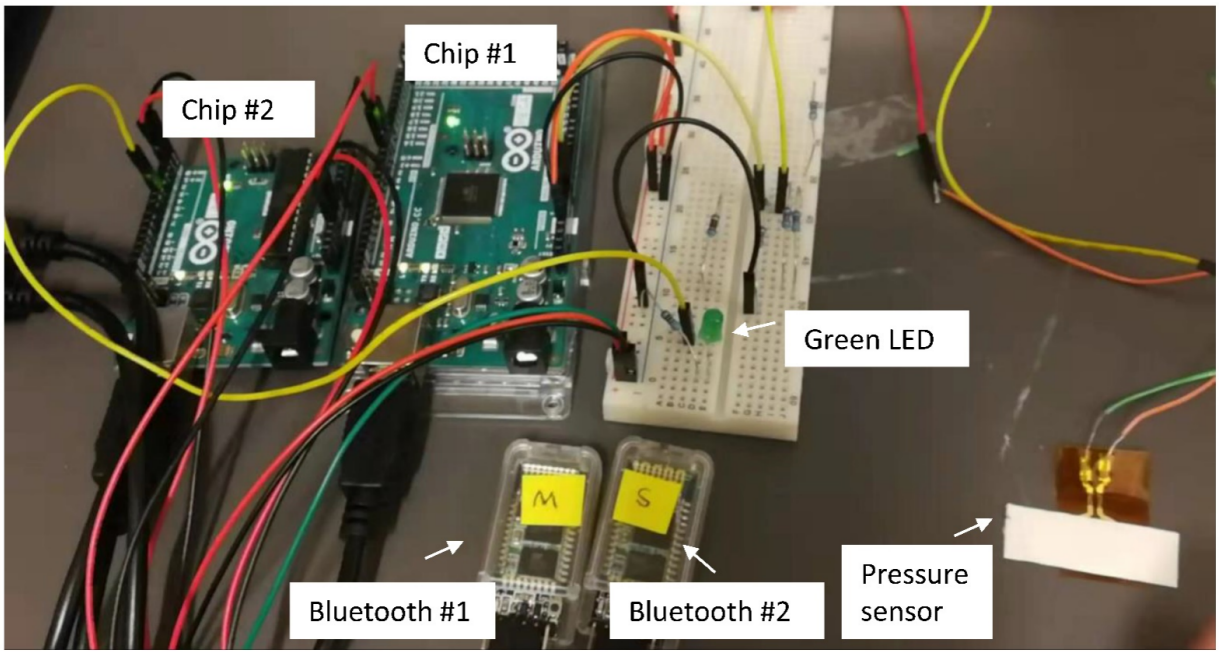

Figure 6.16: Setup of wireless communication system. The pressure information is converted into spikes by chip #1, in which the Izhikevich neuron model is coded and the spike signal can be wirelessly transmitted by Bluetooth #1. Chip #2 with Bluetooth #2 is served as the signal receptor and the received signal is processed to drives the green LED.

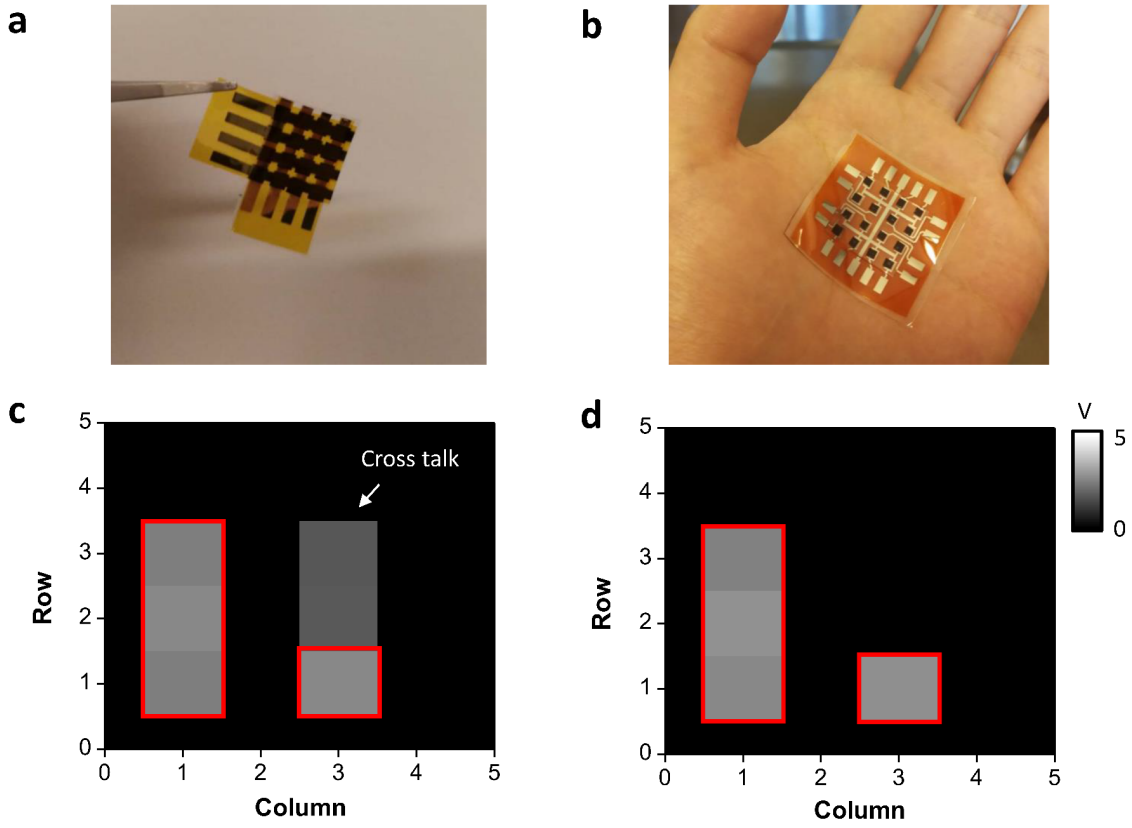

Figure 6.17: Comparison of crosstalk effect between typical orthogonal integration of pressure sensing array and our pressure sensing array. (a) Photograph of the typical orthogonal integration of pressure sensing array. (b) Photograph of our pressure sensing array. (c) pressure mapping of the typical pressure sensing array shows severe crosstalk. (d) pressure mapping of our pressure sensing array (no crosstalk is observed). The red frame is the position of the pressure applied.

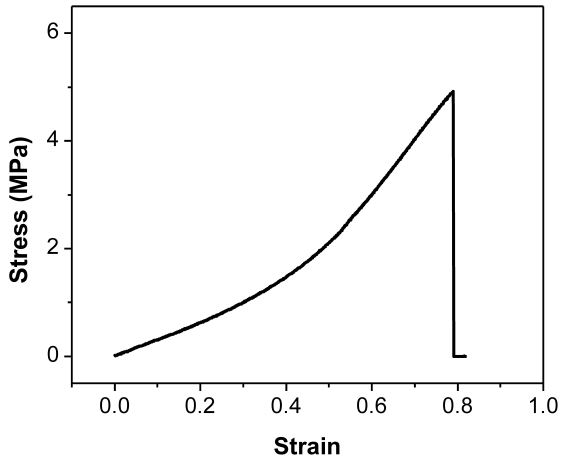

Figure 6.18: Typical stress-strain curve of the conductive micro-pyramidal film made of PDMS/CNT composite. The estimated Young's modulus is about 3.16 MPa.

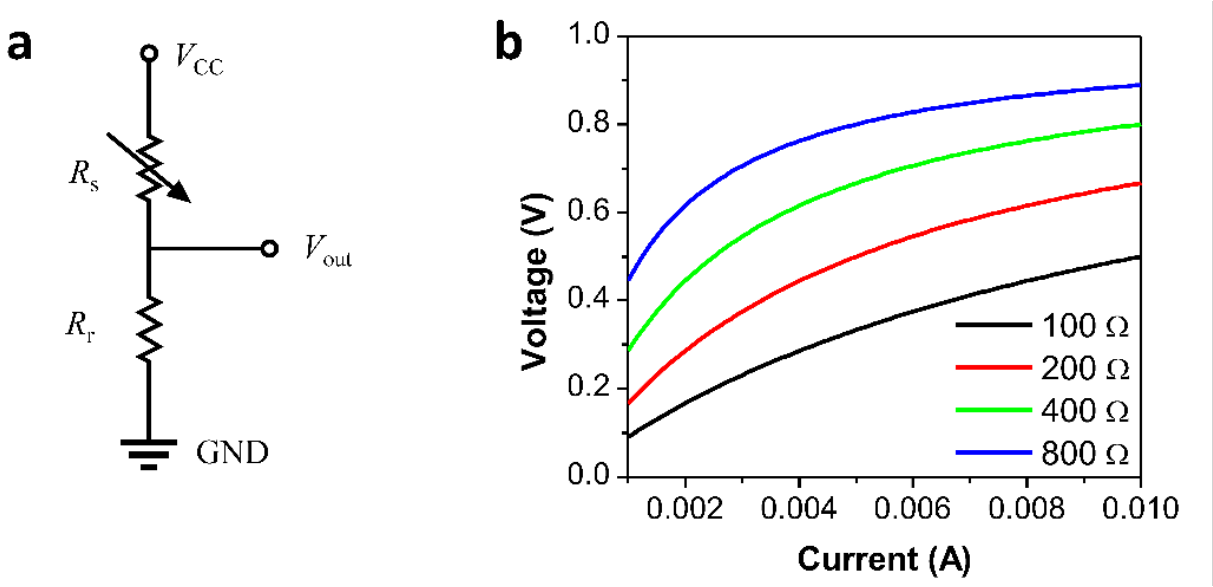

Figure 6.19: Circuit of voltage divider. (a) the circuit model of voltage divider. (b) Numerical simulation of the circuit model. The circuit of voltage divider converts the current ($10^{-3} - 10^{-2}$ A) to the voltage at the supply voltage of 1 V with different reference resistances of 100 Ω , 200 Ω , 400 Ω , and 800 Ω , respectively.

Ref.	Pressure sensors	Sensitivity	Pressure range	Response time	Mechanical robustness	Linear range	Operating voltage
(1)	Silk-mold CNT/PDMS coated	1.8 kPa^{-1} in < 0.4 kPa	1.2 kPa	< 10 ms at 1 kPa	67,500 cycles at 1 kPa	0-0.4 kPa	2 V
(2)	AuNWs coated tissue paper	1.14 kPa^{-1} in 0-5 kPa	~ 5 kPa	< 17 ms at 0.013 kPa	50,000 cycles at 2.5 kPa	0-5 kPa	1.5 V
(3)	Micropillar Au/PDMS coated	0.03-17 kPa^{-1} in <1 kPa	~ 1 kPa				
(4)	Micropillar Au/PDMS coated	2 kPa^{-1} in 0-0.22 kPa; 0.87 kPa^{-1} in 0.22-1 kPa	~ 3.5 kPa	~ 50 ms at 0.02 kPa	10,000 cycles at 1.5 kPa	0-0.22 kPa	1 V
(5)	Leaf-mold Au/PDMS coated	50.17 kPa^{-1} in 0-0.07 kPa 1.38 kPa^{-1} in 0.2-1.5 kPa	~ 1.5 kPa	~ 20 ms at 0.156 kPa	10,000 cycles at 0.156 kPa	0-200 Pa	10 mV
(6)	Leaf-mold CNT/Graphene/ PDMS coated	19.8 kPa^{-1} in <0.3 kPa 0.27 kPa^{-1} in 0.3-6 kPa	~ 6 kPa	~ 16.7 ms at 0.15 Pa	35,000 cycles at 0.150 kPa	0-0.3 kPa	0.03 V
(7)	Micropyramid PEDOT:PSS/PU D coated	4.88 kPa^{-1} in 0.37-5.9 kPa	~ 8 kPa	~ 0.2 s at 6 kPa		0-5.9 kPa	0.2 V
(8)	Micropyramid RGO/PDMS coated	5.5 kPa^{-1} in <100 Pa; 0.01 kPa^{-1} in 100 Pa-1.4kPa	1.4 kPa	0.2 ms at 0.1 kPa	5,000 cycles at 0.1 kPa	0-100 Pa	1V
(9)	Micropyramid AgNWs/PDMS coated	1.3-24.8 kPa^{-1} in < 1kPa	~1 kPa	< 4 ms at 1 kPa	5000 cycles at 1 kPa		1V
(10)	Micropyramid CNT/PDMS coated	53 kPa^{-1} in 0.1 kPa	~1 kPa				
(11)	Sandpaper-mold RGO/PDMS coated	25.1 kPa^{-1} in 0-2.6 kPa; 0.45 kPa^{-1} in ~ 2.6-< 10 kPa	~ < 10 kPa	~ 80 ms at 1.5 kPa	3,000 cycles at 1.5 kPa	0-2.6 kPa	
(12)	Micropatterned graphene/PDMS coated	44.5 kPa^{-1} in 0-1.2 kPa	< 2 kPa		5,000 cycles at 0.6 kPa	0-1.2 kPa	0.01 V
(13)	Hierarchical microdome RGO/PDMS coated	8.5 kPa^{-1} in 0-12 kPa	~ 12 kPa	~ 40 ms at 0.001 kPa	10,000 cycles at 5 kPa	0-12 kPa	1 V

Figure 6.20: A detailed comparison with other resistive pressure sensors.

(14)	RGO/PU sponge	0.26 kPa^{-1} in 0-2 kPa 0.03 kPa^{-1} in 2-10 kPa	10 kPa		10,000 cycles at 2 kPa	0-2 kPa	1 V

Ref.	Pressure sensors	Sensitivity	Pressure range	Response time	Mechanical robustness	Linear range	Operating voltage
(15)	Honeycomb-like graphene	161.1 kPa^{-1} in 0.009-0.56 kPa; 0.92 kPa^{-1} in 2-10 kPa	10 kPa		200 cycles at 100 g	9-560 Pa	10 mV
(16)	Sandpaper-mold graphite/PDMS	64.3 kPa^{-1} in 0-1 kPa; 12.4 kPa^{-1} in 1-10 kPa	~ 10 kPa	~ 8 ms at 0.2 kPa	100,000 cycles at 1 kPa	0-1 kPa	1 V
(17)	Interlocked microdome CNT/PDMS	15.1 kPa^{-1} in < 0.5 kPa	~ 30 kPa	~ 40 ms 0.065 kPa		0-0.5 kPa	1-10 V
(18)	PPy hollow-sphere structure	~7.7-41.9 kPa^{-1} in < 100 Pa 0.03- < 0.4 kPa^{-1} in 1-10 kPa 0.003-0.03 kPa^{-1} in 10-100 kPa	~ 100 kPa	47 ms at 0.28 kPa	8,000 cycles at < 0.1 kPa	Relatively linear in log scale 0-100 kPa	
(19)	Micropore CNT/PDMS/Reverse Micelle Solution	About one order current change in 10-100 kPa	~ 100 kPa	Several seconds		Relatively linear in 0-100 kPa	0.1 V
(20,21)	Micropyramid CNT/P3HT/PU	About one order current change 0-10 kPa; about one order current change in 10-100 kPa	~ 80 kPa		Severe hysteresis and even irrecoverable under ~ 100 kPa		5 V
This work	Micropyramid (1:1 ratio) PDMS/CNT with interdigitated electrodes	More than two-three order current change <10 kPa; more than one order current change in 10-100 kPa (~0.34 kPa)	More than 100 kPa	~ 48 ms at ~ 20 kPa	Over 2000 cycles at 100 kPa; work well undertaking ~ 120 N	10-100 kPa (R^2 > 0.98, the optimal R^2 = 0.9983)	100 μV

Figure 6.21: A detailed comparison with other resistive pressure sensors.

Movie S1 url:

https://pubs.acs.org/doi/suppl/10.1021/acsnano.0c03659/suppl_file/nn0c03659_si_002.mp4

Movie S2 url:

https://pubs.acs.org/doi/suppl/10.1021/acsnano.0c03659/suppl_file/nn0c03659_si_003.mp4

Movie S3 url:

https://pubs.acs.org/doi/suppl/10.1021/acsnano.0c03659/suppl_file/nn0c03659_si_004.mp4

References

[1] Ravinder S. Dahiya, Giorgio Metta, Maurizio Valle, and Giulio Sandini. Tactile sensing—from humans to humanoids. *IEEE Transactions on Robotics*, 26(1):1–20, 2010.

[2] Kuniharu Takei, Toshitake Takahashi, Johnny C. Ho, Hyunhyub Ko, Andrew G. Gillies, Paul W. Leu, Ronald S. Fearing, and Ali Javey. Nanowire active-matrix circuitry for low-voltage macroscale artificial skin. *Nature Materials*, 9(10):821–826, Oct 2010.

[3] Alex Chortos, Jia Liu, and Zhenan Bao. Pursuing prosthetic electronic skin. *Nature Materials*, 15(9):937–950, Sep 2016.

[4] Clementine M. Boutry, Marc Negre, Mikael Jorda, Orestis Vardoulis, Alex Chortos, Oussama Khatib, and Zhenan Bao. A hierarchically patterned, bioinspired e-skin able to detect the direction of applied pressure for robotics. *Science Robotics*, 3(24):eaau6914, 2018.

[5] Luke E. Osborn, Andrei Dragomir, Joseph L. Betthauser, Christopher L. Hunt, Harrison H. Nguyen, Rahul R. Kaliki, and Nitish V. Thakor. Prosthesis with neuromorphic multilayered e-dermis perceives touch and pain. *Science Robotics*, 3(19):eaat3818, 2018.

[6] Subramanian Sundaram, Petr Kellnhofer, Yunzhu Li, Jun-Yan Zhu, Antonio Torralba, and Wojciech Matusik. Learning the signatures of the human grasp using a scalable tactile glove. *Nature*, 569(7758):698–702, May 2019.

[7] Hongbian Li, Suye Lv, and Ying Fang. Bio-inspired micro/nanostructures for flexible and stretchable electronics. *Nano Research*, 13(5):1244–1252, May 2020.

[8] Roland S. Johansson and J. Randall Flanagan. Coding and use of tactile signals from the fingertips in object manipulation tasks. *Nature Reviews Neuroscience*, 10(5):345–359, May 2009.

[9] Stefan C. B. Mannsfeld, Benjamin C-K. Tee, Randall M. Stoltenberg, Christopher V. H-H. Chen, Soumendra Barman, Beinn V. O. Muir, Anatoliy N. Sokolov, Colin Reese, and Zhenan Bao. Highly sensitive flexible pressure sensors with microstructured rubber dielectric layers. *Nature Materials*, 9(10):859–864, Oct 2010.

[10] Chiara Bartolozzi, Lorenzo Natale, Francesco Nori, and Giorgio Metta. Robots with a sense of touch. *Nature Materials*, 15(9):921–925, Sep 2016.

[11] Lijia Pan, Alex Chortos, Guihua Yu, Yaqun Wang, Scott Isaacson, Ranulfo Allen, Yi Shi, Reinhold Dauskardt, and Zhenan Bao. An ultra-sensitive resistive pressure sensor based on hollow-sphere microstructure induced elasticity in conducting polymer film. *Nature Communications*, 5(1):3002, Jan 2014.

[12] Benjamin C.-K. Tee, Alex Chortos, Andre Berndt, Amanda Kim Nguyen, Ariane Tom, Allister McGuire, Ziliang Carter Lin, Kevin Tien, Won-Gyu Bae, Huiliang Wang, Ping Mei, Ho-Hsiu Chou, Bianxiao Cui, Karl Deisseroth, Tse Nga Ng, and Zhenan Bao. A skin-inspired organic digital mechanoreceptor. *Science*, 350(6258):313–316, 2015.

[13] Yeongin Kim, Alex Chortos, Wentao Xu, Yuxin Liu, Jin Young Oh, Donghee Son, Jiheong Kang, Amir M. Foudeh, Chenxin Zhu, Yeongjun Lee, Simiao Niu, Jia Liu, Raphael Pfattner, Zhenan Bao, and Tae-Woo Lee. A bioinspired flexible organic artificial afferent nerve. *Science*, 360(6392):998–1003, 2018.

[14] Takao Someya, Tsuyoshi Sekitani, Shingo Iba, Yusaku Kato, Hiroshi Kawaguchi, and Takayasu Sakurai. A large-area, flexible pressure sensor matrix with organic field-effect transistors for artificial skin applications. *Proceedings of the National Academy of Sciences*, 101(27):9966–9970, 2004.

[15] Xuewen Wang, Yang Gu, Zuoping Xiong, Zheng Cui, and Ting Zhang. Silk-molded flexible, ultrasensitive, and highly stable electronic skin for monitoring human physiological signals. *Advanced Materials*, 26(9):1336–1342, 2014.

[16] Shu Gong, Willem Schwalb, Yongwei Wang, Yi Chen, Yue Tang, Jye Si, Bijan Shirinzadeh, and Wenlong Cheng. A wearable and highly sensitive pressure sensor with ultrathin gold nanowires. *Nature Communications*, 5(1):3132, Feb 2014.

[17] Bowen Zhu, Zhiqiang Niu, Hong Wang, Wan Ru Leow, Hua Wang, Yuangang Li, Liyan Zheng, Jun Wei, Fengwei Huo, and Xiaodong Chen. Microstructured graphene arrays for highly sensitive flexible tactile sensors. *Small*, 10(18):3625–3631, 2014.

[18] Chwee-Lin Choong, Mun-Bo Shim, Byoung-Sun Lee, Sanghun Jeon, Dong-Su Ko, Tae-Hyung Kang, Jihyun Bae, Sung Hoon Lee, Kyung-Eun Byun, Jungkyun Im, Yong Jin Jeong, Chan Eon Park, Jong-Jin Park, and U-In Chung. Highly stretchable resistive pressure sensors using a conductive elastomeric composite on a micropyramid array. *Advanced Materials*, 26(21):3451–3458, 2014.

[19] Geun Yeol Bae, Sang Woo Pak, Daegun Kim, Giwon Lee, Do Hwan Kim, Yoonyoung Chung, and Kilwon Cho. Linearly and highly pressure-sensitive electronic skin based on a bioinspired hierarchical structural array. *Advanced Materials*, 28(26):5300–5306, 2016.

[20] Jonghwa Park, Youngoh Lee, Jaehyung Hong, Minjeong Ha, Young-Do Jung, Hyuneui Lim, Sung Youb Kim, and Hyunhyub Ko. Giant tunneling piezoresistance of composite elastomers with interlocked microdome arrays for ultrasensitive and multimodal electronic skins. *ACS Nano*, 8(5):4689–4697, 2014. PMID: 24592988.

[21] Qi-Jun Sun, Jiaqing Zhuang, Shishir Venkatesh, Ye Zhou, Su-Ting Han, Wei Wu, Ka-Wai Kong, Wen-Jung Li, Xianfeng Chen, Robert K. Y. Li, and Vellaisamy A. L. Roy. Highly sensitive and ultrastable skin sensors for biopressure and bioforce measurements based on hierarchical microstructures. *ACS Applied Materials & Interfaces*, 10(4):4086–4094, 2018. PMID: 29345473.

[22] Chiseon Yeom, Kevin Chen, Daisuke Kiriya, Zhibin Yu, Gyoujin Cho, and Ali Javey.

Large-area compliant tactile sensors using printed carbon nanotube active-matrix backplanes. *Advanced Materials*, 27(9):1561–1566, 2015.

[23] Kailun Xia, Chunya Wang, Muqiang Jian, Qi Wang, and Yingying Zhang. Cvd growth of fingerprint-like patterned 3d graphene film for an ultrasensitive pressure sensor. *Nano Research*, 11(2):1124–1134, Feb 2018.

[24] Sungmook Jung, Ji Hoon Kim, Jaemin Kim, Suji Choi, Jongsu Lee, Inhyuk Park, Taeghwan Hyeon, and Dae-Hyeong Kim. Reverse-micelle-induced porous pressure-sensitive rubber for wearable human–machine interfaces. *Advanced Materials*, 26(28):4825–4830, 2014.

[25] Lizhi Sheng, Yuan Liang, Lili Jiang, Qian Wang, Tong Wei, Liangti Qu, and Zhuangjun Fan. Bubble-decorated honeycomb-like graphene film as ultrahigh sensitivity pressure sensors. *Advanced Functional Materials*, 25(41):6545–6551, 2015.

[26] Muqiang Jian, Kailun Xia, Qi Wang, Zhe Yin, Huimin Wang, Chunya Wang, Huanhuan Xie, Mingchao Zhang, and Yingying Zhang. Flexible and highly sensitive pressure sensors based on bionic hierarchical structures. *Advanced Functional Materials*, 27(9):1606066, 2017.

[27] Huaying Ren, Liming Zheng, Guorui Wang, Xin Gao, Zhenjun Tan, Jingyuan Shan, Lingzhi Cui, Ke Li, Muqiang Jian, Liangchao Zhu, Yingying Zhang, Hailin Peng, Di Wei, and Zhongfan Liu. Transfer-medium-free nanofiber-reinforced graphene film and applications in wearable transparent pressure sensors. *ACS Nano*, 13(5):5541–5548, 2019. PMID: 31034773.

[28] Benjamin C.-K. Tee, Alex Chortos, Roger R. Dunn, Gregory Schwartz, Eric Eason, and Zhenan Bao. Tunable flexible pressure sensors using microstructured elastomer geometries for intuitive electronics. *Advanced Functional Materials*, 24(34):5427–5434, 2014.

[29] Yaping Zang, Fengjiao Zhang, Dazhen Huang, Xike Gao, Chong-an Di, and Daoben Zhu. Flexible suspended gate organic thin-film transistors for ultra-sensitive pressure detection. *Nature Communications*, 6(1):6269, Mar 2015.

[30] Yunsik Joo, Junghwan Byun, Narkhyeon Seong, Jewook Ha, Hyunjong Kim, Sangwoo Kim, Taehoon Kim, Hwarim Im, Donghyun Kim, and Yongtaek Hong. Silver nanowire-embedded pdms with a multiscale structure for a highly sensitive and robust flexible pressure sensor. *Nanoscale*, 7:6208–6215, 2015.

[31] Geun Yeol Bae, Joong Tark Han, Giwon Lee, Siyoung Lee, Sung Won Kim, Sangsik Park, Jimin Kwon, Sungjune Jung, and Kilwon Cho. Pressure/temperature sensing bimodal electronic skin with stimulus discriminability and linear sensitivity. *Advanced Materials*, 30(43):1803388, 2018.

[32] Wen Cheng, Jun Wang, Zhong Ma, Ke Yan, Yunmu Wang, Huiting Wang, Sheng Li, Yun Li, Lijia Pan, and Yi Shi. Flexible pressure sensor with high sensitivity and low hysteresis based on a hierarchically microstructured electrode. *IEEE Electron Device Letters*, 39(2):288–291, 2018.

[33] Yun-Chiao Huang, Yuan Liu, Chao Ma, Hung-Chieh Cheng, Qiyuan He, Hao Wu, Chen Wang, Cheng-Yi Lin, Yu Huang, and Xiangfeng Duan. Sensitive pressure sensors based on conductive microstructured air-gap gates and two-dimensional semiconductor transistors. *Nature Electronics*, 3(1):59–69, Jan 2020.

[34] Canan Dagdeviren, Yewang Su, Pauline Joe, Raissa Yona, Yuhao Liu, Yun-Soung Kim, YongAn Huang, Anoop R. Damadoran, Jing Xia, Lane W. Martin, Yonggang Huang, and John A. Rogers. Conformable amplified lead zirconate titanate sensors with enhanced piezoelectric response for cutaneous pressure monitoring. *Nature Communications*, 5(1):4496, Aug 2014.

[35] Yao Chu, Junwen Zhong, Huiliang Liu, Yuan Ma, Nathaniel Liu, Yu Song, Jiaming

Liang, Zhichun Shao, Yu Sun, Ying Dong, Xiaohao Wang, and Liwei Lin. Human pulse diagnosis for medical assessments using a wearable piezoelectret sensing system. *Advanced Functional Materials*, 28(40):1803413, 2018.

[36] Chonghe Wang, Xiaoshi Li, Hongjie Hu, Lin Zhang, Zhenlong Huang, Muyang Lin, Zhuorui Zhang, Zhenan Yin, Brady Huang, Hua Gong, Shubha Bhaskaran, Yue Gu, Mitsutoshi Makihata, Yuxuan Guo, Yusheng Lei, Yimu Chen, Chunfeng Wang, Yang Li, Tianjiao Zhang, Zeyu Chen, Albert P. Pisano, Liangfang Zhang, Qifa Zhou, and Sheng Xu. Monitoring of the central blood pressure waveform via a conformal ultrasonic device. *Nature Biomedical Engineering*, 2(9):687–695, Sep 2018.

[37] Kyoung-Yong Chun, Young Jun Son, Eun-Seok Jeon, Sehan Lee, and Chang-Soo Han. A self-powered sensor mimicking slow- and fast-adapting cutaneous mechanoreceptors. *Advanced Materials*, 30(12):1706299, 2018.

[38] Fengjiao Zhang, Yaping Zang, Dazhen Huang, Chong-an Di, and Daoben Zhu. Flexible and self-powered temperature–pressure dual-parameter sensors using microstructure-frame-supported organic thermoelectric materials. *Nature Communications*, 6(1):8356, Sep 2015.

[39] Feng-Ru Fan, Long Lin, Guang Zhu, Wenzhuo Wu, Rui Zhang, and Zhong Lin Wang. Transparent triboelectric nanogenerators and self-powered pressure sensors based on micropatterned plastic films. *Nano Letters*, 12(6):3109–3114, 2012. PMID: 22577731.

[40] Peng Bai, Guang Zhu, Qingshen Jing, Jin Yang, Jun Chen, Yuanjie Su, Jusheng Ma, Gong Zhang, and Zhong Lin Wang. Membrane-based self-powered triboelectric sensors for pressure change detection and its uses in security surveillance and healthcare monitoring. *Advanced Functional Materials*, 24(37):5807–5813, 2014.

[41] Partha Sarati Das, Ashok Chhetry, Pukar Maharjan, M. Salauddin Rasel, and Jae Yeong

Park. A laser ablated graphene-based flexible self-powered pressure sensor for human gestures and finger pulse monitoring. *Nano Research*, 12(8):1789–1795, Aug 2019.

[42] Ying-Chih Lai, Jianan Deng, Ruiyuan Liu, Yung-Chi Hsiao, Steven L. Zhang, Wenbo Peng, Hsing-Mei Wu, Xingfu Wang, and Zhong Lin Wang. Actively perceiving and responsive soft robots enabled by self-powered, highly extensible, and highly sensitive triboelectric proximity- and pressure-sensing skins. *Advanced Materials*, 30(28):1801114, 2018.

[43] Minjeong Ha, Seongdong Lim, Soowon Cho, Youngoh Lee, Sangyun Na, Chunggi Baig, and Hyunhyub Ko. Skin-inspired hierarchical polymer architectures with gradient stiffness for spacer-free, ultrathin, and highly sensitive triboelectric sensors. *ACS Nano*, 12(4):3964–3974, 2018. PMID: 29620871.

[44] Ming Li, Yang Jie, Li-Hua Shao, Yilin Guo, Xia Cao, Ning Wang, and Zhong Lin Wang. All-in-one cellulose based hybrid tribo/piezoelectric nanogenerator. *Nano Research*, 12(8):1831–1835, Aug 2019.

[45] Yu Pang, Kunning Zhang, Zhen Yang, Song Jiang, Zhenyi Ju, Yuxing Li, Xuefeng Wang, Danyang Wang, Muqiang Jian, Yingying Zhang, Renrong Liang, He Tian, Yi Yang, and Tian-Ling Ren. Epidermis microstructure inspired graphene pressure sensor with random distributed spinosum for high sensitivity and large linearity. *ACS Nano*, 12(3):2346–2354, 2018. PMID: 29378401.

[46] Bowen Zhu, Hong Wang, Yaqing Liu, Dianpeng Qi, Zhiyuan Liu, Hua Wang, Jiancan Yu, Matthew Sherburne, Zhaohui Wang, and Xiaodong Chen. Skin-inspired haptic memory arrays with an electrically reconfigurable architecture. *Advanced Materials*, 28(8):1559–1566, 2016.

[47] Changjin Wan, Geng Chen, Yangming Fu, Ming Wang, Naoji Matsuhisa, Shaowu Pan,

Liang Pan, Hui Yang, Qing Wan, Liqiang Zhu, and Xiaodong Chen. An artificial sensory neuron with tactile perceptual learning. *Advanced Materials*, 30(30):1801291, 2018.

[48] Minjeong Ha, Seongdong Lim, Jonghwa Park, Doo-Seung Um, Youngoh Lee, and Hyunhyub Ko. Bioinspired interlocked and hierarchical design of zno nanowire arrays for static and dynamic pressure-sensitive electronic skins. *Advanced Functional Materials*, 25(19):2841–2849, 2015.

[49] Dae-Hyeong Kim, Nanshu Lu, Rui Ma, Yun-Soung Kim, Rak-Hwan Kim, Shuodao Wang, Jian Wu, Sang Min Won, Hu Tao, Ahmad Islam, Ki Jun Yu, Tae il Kim, Raeed Chowdhury, Ming Ying, Lizhi Xu, Ming Li, Hyun-Joong Chung, Hohyun Keum, Martin McCormick, Ping Liu, Yong-Wei Zhang, Fiorenzo G. Omenetto, Yonggang Huang, Todd Coleman, and John A. Rogers. Epidermal electronics. *Science*, 333(6044):838–843, 2011.

[50] Takao Someya, Zhenan Bao, and George G Malliaras. The rise of plastic bioelectronics. *Nature*, 540(7633):379–385, December 2016.

[51] E.M. Izhikevich. Simple model of spiking neurons. *IEEE Transactions on Neural Networks*, 14(6):1569–1572, 2003.

CHAPTER 7

Conclusion

Here I reported two major types of applications for van der Waal thin films: one to use the VDWTF as transistors for large scale circuits as the conventional use of semiconducting materials, and the other one as a free standing thin film sensor for bio-signal detection.

As a conventional semiconducting material, the VDWTF exhibits its capability as a candidate for large scale circuits with a high device performance and wafer scale uniformity. Also the easy process and low cost with a long lifetime ensure the possibility for really application. The first application is an 10×10 active pressure mapping matrix. Here the thin film transistor shows a high performance with a $10^5 - 10^6$ on/off ratio and negligible hysteresis. Also the doping level and thus the sub-threshold swing can be tuned by changing the annealing temperature. And therefore it can be adapted for different applications. Moreover, the yield of the whole process is high as 98% and can be modified easily for different purposes. Then we combine the transistor matrix with a highly sensitive pressure sensing rubber, and demonstrate that this pressure sensor can accurately map the pressure distribution of target even for small pressure range (<100 kPa). And this pressure sensor can be further developed into electronic skin and other applications.

Then we apply the thin film for opto electronics applications. The 2D thin film has high light transimission rate so we successfully build a transparent photo transistor with it. And we combine a 100×100 matrix of photo transistor with liquid crystal to tune the trans-

parency of the liquid crystal by the light pass through it. The demonstration shows that this transparent device can be used as a glare reduction system with rapid response. And in the future this setup can be further adapted into diffractive deep neural network.

The second type of application is for flexible electronics. The VDWTF is a great candidates for this becasue of its special structure and morphology: the weak van der Waal connection between each layers allows the flakes to slide with each other to compensate the strain generated during deformation, which makes it stretchable and adaptive to fine-featured targets. Then we demonstrate that this thin film can cover the arbitrary featured skin with high conformability and its high durability/adaptability make it possible to pick up high quality signal even during motion. However, this is just a start of the application, and further work needs to be done to develop a single material into a really portable device.